Modeling Polarimetric Imaging using DIRSIG

by

Jason P. Meyers

M.S.E.E., Observables Reduction, Air Force Institute of Technology,
Wright-Patterson AFB, OH, 1994

B.S., Electrical Engineering, Michigan Technological University, 1993

A dissertation submitted in partial fulfillment of the
requirements for the degree of Doctor of Philosophy
in the Chester F. Carlson Center for Imaging Science
Rochester Institute of Technology

2002

Signature of the Author _____

Accepted by _____
Coordinator, Ph.D. Degree Program Date

CHESTER F. CARLSON CENTER FOR IMAGING SCIENCE
ROCHESTER INSTITUTE OF TECHNOLOGY
ROCHESTER, NEW YORK

CERTIFICATE OF APPROVAL

Ph.D. DEGREE DISSERTATION

The Ph.D. Degree Dissertation of Jason P. Meyers
has been examined and approved by the
dissertation committee as satisfactory for the
dissertation required for the
Ph.D. degree in Imaging Science

Dr. John Schott, Dissertation Advisor

Dr. William Grande, Committee Chair

Dr. Joel Kastner

Dr. Michael Kotlarchyk

Date

DISSERTATION RELEASE PERMISSION

ROCHESTER INSTITUTE OF TECHNOLOGY

CHESTER F. CARLSON CENTER FOR IMAGING SCIENCE

Title of Dissertation:

Modeling Polarimetric Imaging using DIRSIG

I, Jason P. Meyers, hereby grant permission to Wallace Memorial Library of R.I.T. to reproduce my thesis in whole or in part. Any reproduction will not be for commercial use or profit.

Signature _____

Date

Modeling Polarimetric Imaging using DIRSIG

by

Jason P. Meyers

Submitted to the
Chester F. Carlson Center for Imaging Science
in partial fulfillment of the requiremnets
for the Doctor of Philosophy Degree
at the Rochester Institute of Technology

Abstract

The remote sensing community is beginning to recognize the potential benefit of exploiting polarimetric signatures. The ability to accurately model polarimetric phenomenology in a remote sensing system will assist efforts in system design, algorithm development, phenomenology studies, and analyst training. This dissertation lays the ground work for enhancing the current Digital Imaging and Remote Sensing Laboratory's Synthetic Image Generation (DIRSIG) model to include polarimetric phenomenology. The current modeling capabilities are discussed along with the theoretical background required to expand upon the current state of the art. Methods for modeling and estimating polarimetric signatures and phenomenology from start to end in a typical remote sensing system are presented. A series of simple simulations were conducted to assess the performance of the new polarimetric capabilities. Analysis was performed to characterize the individual models and the collected performance of the models.

DISCLAIMER

The views expressed in this article are those of the authors and do not reflect the official policy or position of the United States Air Force, Department of Defense, or the U.S. Government.

Contents

List of Figures

List of Tables

Nomenclature

The symbols used throughout this dissertation are listed here. Note that the symbols for electric field values and irradiances both typically use the letter E. In order to reduce confusion, I have chosen to use script letters for the electric and magnetic field values.

Symbol	Definition
a	Length of the major axis of the polarization ellipse
α	Angle of rotation for linearly polarized light
b	Length of the minor axis of the polarization ellipse
$\overrightarrow{\boldsymbol{\mathcal{B}}}$	Magnetic field
E	Irradiance
$\overrightarrow{\boldsymbol{\mathcal{E}}}$	Electric field vector
$\mathcal{E}_x$	$\hat{\mathbf{x}}$ component of the E-field vector
$\mathcal{E}_{0x}$	Peak amplitude of the $\hat{\mathbf{x}}$ component of the E-field vector
$\mathcal{E}_y$	$\hat{\mathbf{y}}$ component of the E-field vector
$\mathcal{E}_{0y}$	Peak amplitude of the $\hat{\mathbf{y}}$ component of the E-field vector
f	Unpolarized BRDF
$\boldsymbol{f}$	Polarized BRDF
θ	Zenith angles
I	Intensity
k	Imaginary part of the complex index of refraction
$\overrightarrow{\mathbf{k}}$	Direction of propagation
L	Radiance

Symbol	Definition
$\mathbf{M}$	Mueller matrix
n	Real part of the complex index of refraction
$\tilde{n}$	Complex index of refraction
P	Degree of polarization (DoP)
P_{lin}	Degree of linear polarization (DoLP)
ϕ	Azimuth angles
Φ	Flux
$r_{\|\|}$	Fresnel reflection amplitude parallel to the plane of incidence
$r_{\perp}$	Fresnel reflection amplitude perpendicular to the plane of incidence
$R_{\|\|}$	Fresnel reflectance parallel to the plane of incidence
$R_{\perp}$	Fresnel reflectance perpendicular to the plane of incidence
ρ'	BRDF (Beard-Maxwell notation)
S_{0-3}	Stokes parameters corresponding to the traditional Stokes parameters I, Q, U, V respectively
$\mathbf{S}$	Stokes vector
σ	Surface roughness
$t_{\|\|}$	Fresnel transmission amplitude parallel to the plane of incidence
$t_{\perp}$	Fresnel transmission amplitude perpendicular to the plane of incidence
$T_{\|\|}$	Fresnel transmittance parallel to the plane of incidence
$T_{\perp}$	Fresnel transmittance perpendicular to the plane of incidence
ω	Solid angle
$\hat{\mathbf{x}}$	Unit vector along the x-axis
χ	Ellipticity angle
$\hat{\mathbf{y}}$	Unit vector along the y-axis
ψ	Angle of rotation of the polarization ellipse
$\hat{\mathbf{z}}$	Unit vector along the z-axis

The following list defines the terms and acronyms used in this proposal. Included in the list are some company names and trade marks for informational purposes only. The referencing of these names does not constitute an endorsement by the author, the Rochester Institute of Technology, the United States Air Force, the Department of Defense, nor the U.S. Government.

Term	Definition
ADEOS	Advanced Earth Observing Satellite
AFB	Air Force Base
AFIT	Air Force Institute of Technology
AFRL	Air Force Research Laboratory
BDRF	BiDirectional Reflectance Factor
BRDF	Bidirectional Reflectance Distribution Function
CIS	Carlson Center for Imaging Science
DHR	Directional Hemispherical Reflectance
DIRS	Digital Imaging and Remote Sensing group within CIS
DIRSIG	Digital Imaging and Remote Sensing Laboratory's Image Generation model
DoLP	Degree of Linear Polarization
DoP	Degree of Polarization
ERIM	Environmental Research Institute of Michigan (now Veridian)
F-BEAM	First-Principles BRDF Evaluation and Analysis Model
IR	Infrared
LASS	Laboratory for Advanced Spectral Studies
MODTRAN	Moderate Resolution Transmission Code
MODTRAN-P	Polarized version of MODTRAN
NEF	Nonconventional Exploitation Factors (database)
NEFDS	Nonconventional Exploitation Factors Data System
NIMA	National Imagery and Mapping Agency
PI	Polarimetric Imaging
POLDER	Polarization and Directionality of Earth Reflectances
RIT	Rochester Institute of Technology

Chapter 1

Introduction

> Then God said, "Let there be light," and there was light. God saw how good the light was. God then separated the light from the darkness.
>
> *Genesis 1:3–4*

Polarized filters have long been used in sunglasses and photography to reduce unwanted glare (see figures 1.1 and 1.2). Many manmade objects and some natural materials, like water, tend to polarize the light they reflect and emit. Based on solar illumination and view angles, scattered skylight can have a significant level of polarization. Therefore, the possibility exists to exploit the information contained in remotely sensed polarized light. Until recently, the use of polarization in remote sensing has been limited to astronomy (Egan 1985).

The remote sensing community is beginning to recognize the potential benefits of exploiting polarization signatures. Polarized filters can be used to increase cloud contrasts (Egan 1985). Polarization effects could aide in detecting manmade objects and increasing signal to background clutter ratios. Polarization may help counter various concealment and deception techniques (Straw 2001).

Figure 1.1: Photograph of a window using a vertically polarized filter.

Figure 1.2: Photograph of a window using a horizontally polarized filter.

Terrestrial remote sensing has been slow to exploit the benefits of polarimetry. This is primarily due to the added complexity of simultaneously collecting multiple polarization components (Egan 1992). Beginning in 1984, the space shuttle was used to conduct multiple experiments to test the feasibility and utility of polarimetry from space based platforms (Whitehead 1992; Egan et al. 1991). The Japanese Advanced Earth Observing Satellite (ADEOS) satellite carried the Polarization and Directionality of Earth Reflectances (POLDER) sensor which collected polarized and directional reflectance data. The POLDER sensor collected data at very low spatial resolution ($6 \times 7\,\mathrm{km}^2$) (Deschamps et al. 1994; Nadal and Bréon 1999). As remote sensing technology continues to mature, we can expect to see additional remote sensing systems take advantage of polarization signals.

Synthetically generated hyperspectral imagery has proven useful in many aspects of remote sensing. Synthetic imagery is currently used in support of sensor design studies; algorithm development, training, and evaluation; phenomenology studies; and analyst training. A major benefit of synthetic imagery is the inherent ground truth data which makes it easier to understand the system being studied. Synthetic imagery also provides the ability to easily construct identical scenes with varying atmospheric and imaging conditions. Finally, synthetic imagery is typically much cheaper than traditionally collected imagery. When the physical phenomena are well understood and adequately modeled, synthetic imagery poses a very cost effective alternative to collected imagery.

Current synthetic image generation programs lack the ability to model polarimetric phenomenology. The purpose of this research is to investigate the intricacies of modeling hyperspectral polarimetry phenomenology within remote sensing applications. This research developed the foundation for including the modeling of hyper-

spectral polarimetry within RIT's Digital Imaging and Remote Sensing Laboratory's Synthetic Image Generation (DIRSIG) program. The result is a physics based model which can be used to model remote sensing based polarimetry. The improved DIRSIG model can be used for instrument design studies, algorithm development and evaluation, analyst training, and phenomenology studies.

The objectives and scope of the research are given in the next chapter. The relevant theoretical background information is presented in chapter 3. The current synthetic image generation and bidirectional reflectance modeling capabilities are presented in chapters 4 and 5. Both of these chapters also discuss the limitations which were addressed by this research. The approach for completing the objectives of this research are detailed in chapter 6 with the results presented in chapter 7.

Chapter 2

Objectives

> Basic research is what I am doing when I don't know what I am doing.
>
> Werner Von Braun

This chapter gives a high level overview of the research efforts and expected results. The details of specific aspects of the research are provided in later chapters. The scope of this research effort is presented in section 2.3.

The objectives of this research were grouped into two classes. The first group includes those objectives required to successfully complete the requirements of this dissertation. The second group was additional objectives which were not required but provided added value. The second group was called the "Goals". Completion of the goals depended upon time constraints and the availability of required resources and applicable data.

2.1 Success Criteria

The following list are the objectives that were established for the successful completion of this dissertation:

- Gain an understanding of polarimetric phenomenology associated with hyperspectral remote sensing in the visible portion of the spectrum.
- Develop the ability to model polarimetric radiative transfer phenomena within DIRSIG using Stokes parameters and Mueller matrices. The new model will handle the following cases:
  - Full polarimetric characterization data available to include polarized illumination field, polarimetric bidirectional reflectance distribution function (BRDF) database and/or models, polarization and depolarization effects resulting from atmospheric transmission and scattering, and full sensor polarization characterization.
  - Graceful degradation to a partially polarized or unpolarized model when full polarimetric characterization data is not available. For example, using unpolarized illumination field data with polarized BRDF data would result in a polarized output based on the assumption that all illumination was randomly polarized.
  - In the absence of all polarimetric information, resort to the current unpolarized DIRSIG model.
- Investigate and implement a simple algorithm for estimating the polarization characteristics of the illumination field and atmospheric contributions. This may be accomplished using one or both of the following methods:

- modifying tabulated polarized atmospheric data tables
- estimating atmospheric polarization based on MODTRAN predictions of single versus multiple scattered radiance fields.

The DIRSIG modifications will include the ability to import propagation terms and polarized radiance values generated by a polarized version of MODTRAN or other radiative transfer models.

- Investigate and implement methods of modeling hyperspectral polarimetric bidirectional reflectances when limited data is available.
- Investigate the interaction between target and background polarimetric bidirectional reflectances. This will be accomplished through a combination of optional field experiments and model simulation sensitivity studies.
- Include hyperspectral polarimetric characteristics in the generic sensor model.
- Assess the accuracy and sensitivities of the hyperspectral polarimetric modeling through a simple validation effort. The validation effort will be split into the following levels:

  Laboratory simulation: Use simple geometric shapes to prove the validity of individual models and algorithms.

  Simple Scene: Construct a simple outdoor scene with as many variables controlled as possible. For example, this may be a parking lot scene located near the Center for Imaging Science (CIS). This test would demonstrate various interactions of groups of models and algorithms.

  Complex Scene: Demonstrate the feasibility of modeling polarimetric remote sensing of a large "real world" scene. This scene may be the mega scene

being developed for the Laboratory for Advanced Spectral Studies (LASS) or one of the standard DIRSIG scenes.

2.2 Goals

The following goals will assist in the successful completion of the required tasks listed above in section 2.1:

- Collect limited polarimetric directional hemispherical reflectance (DHR) data. This may be accomplished using the DIRS ASD field spectrometer and a combination of polarization filters and an illumination source. These data would provide some additional limited polarization data for characterizing some background materials and other materials of interest.

- Obtain full polarimetric BRDF measurements for various material samples from the Air Force Research Labs (AFRL) BRDF measurement facility. This data would assist in evaluating the accuracy and usability of various BRDF models.

- Compare DIRSIG polarimetric simulations with actual polarimetric remotely sensed imagery. This task depends heavily upon the availability of polarimetric imagery and the ability to model the scene that was imaged.

2.3 Scope

There are many complexities involved in fully characterizing and modeling polarimetric remote sensing. This research is focused on developing a physics based model which produces a good approximation of a realistic polarimetric remote sensing system. The model cannot and will not be able to accurately predict all sources

of polarization and all energy-matter interactions. Such a model would require an inordinate amount of computer resources and computation time. This research will attempt to identify and model the most significant polarimetric phenomena and interactions involved in a typical remote sensing system. The following is a list of things which are out of scope of this dissertation:

- Detailed polarimetric characterization of atmospheric illumination, transmission, absorption, and scattering. AFRL is currently conducting efforts to include polarimetric atmospheric modeling within MODTRAN. This research used an alpha test version of the polarized MODTRAN model. The accuracy of the model was not investigated, rather it was used to generate plausible atmospheric contributions.

- Development of high fidelity physics based BRDF models. The lack of measured BRDF data, both polarized and unpolarized, severely limits the potential for development and validation of more complicated BRDF models.

- Propagation of coherent light. It is assumed that all sources are mutually independent and incoherent.

- Characterization of sensor systems using polarimetric ray tracing. Instead, the improved DIRSIG sensor model will include methods of characterizing the polarization effects on a per pixel basis. This will most likely be accomplished using a Mueller transformation matrix on a per pixel basis.

- Modeling of clouds and plumes.

This is not an exhaustive list of items which are specifically out of the scope of this research. The research is primarily concerned with the initial development of

a polarimetric modeling capability. The infrastructure developed will be specifically designed to accommodate improved modeling capabilities as they become available. This will be accomplished through a modular design approach which will enable the modification of individual modules without affecting the performance of other modules.

Chapter 3

Theory

> I have also a paper afloat, with an electromagnetic theory of light, which, till I am convinced to the contrary, I hold to be great guns.
>
> *A letter to C. H. Cay, 5 January 1865*
> James Clerk Maxwell

This chapter provides a discussion of the relevant theory and background information necessary for this research. Most of the theories presented can be derived from Maxwell's equations. For the sake of clarity, I have chosen to omit the tedious derivations and simply present the results. However, I felt it was still necessary to acknowledge the great contributions of Maxwell. Complete derivations can be found in many places within the literature. Additional references are provided for related topics which are not fully discussed in this chapter or elsewhere in this dissertation.

3.1 Polarization

I begin this chapter with a discussion of polarization, the main focus of this research. This discussion begins with a short history which is followed by a description

of the types of polarization and the mathematics which is used to describe the polarization characteristics of light.

3.1.1 Historical Discoveries of Polarization Phenomenology

This section attempts to give a brief overview of the highlights of the history behind the discoveries related to polarization phenomenology. Below you will find extracts from two well written histories by Coulson (1988) and Brosseau (1998). Both authors give a much more in depth history in the introductions of their books.

The fact that light, and hence electromagnetic radiation, can be polarized was first discovered by a Danish professor named Erasmus Bartolinus. He published his discovery in 1669 in an article about the properties of Iceland spar which is a variety of calcite. However, it wasn't until the 19^{th} century that the term polarization was introduced by the French Colonel E. L. Malus. Colonel Malus discovered that by looking through calcite crystals, reflections from windows could be made to disappear. This observation lead Malus to discover the laws of reflection.

Through experimentation, Fresnel was able to prove that light propagated as transverse and not longitudinal waves. He concluded this based on two observations: first, different polarizations did not interfere and second, polarized light exhibited symmetry about two orthogonal planes parallel to the direction of propagation. Fresnel went on to develop the Fresnel equations which calculate the polarization of reflected and refracted light at the boundary of two transparent media.

Although Sir David Brewster is credited with discovering the Brewster angle, Coulson (1988) points out that even Brewster recognized that Malus was first to discover it. The Brewster angle is the angle at which reflected light is fully polarized. This occurs because one of the linear polarization states is fully transmitted thus

leaving only one polarization state reflected.

Finally, this historical review is concluded with the contributions of Sir Georges Gabriel Stokes and Hans Mueller. Stokes introduced four measurable parameters which fully describe all possible polarization states of light now called Stokes parameters. The combination of the measurability and completeness of the Stokes parameters makes them ideal for characterizing polarized light. Mueller, among others, developed the Mueller matrix and Jones calculus which can be used to relate the input and output Stokes parameters of a given system.

3.1.2 Types of Polarization

Before discussing the various polarization states, it is useful to understand the reasoning behind the convention used to name the states. All light waves are composed of electric ($\overrightarrow{\mathcal{E}}$) and magnetic ($\overrightarrow{\mathcal{B}}$) field vectors which are mutually orthogonal to each other and the direction of propagation. The names of the polarization states (i.e. vertical or horizontal) refer to the orientation of $\overrightarrow{\mathcal{E}}$. The choice of electric field vector over the magnetic field vector may seem arbitrary. However, Brosseau (1998, pp. 48–50) points out that in 1890, Otto Wiener published the results of an experiment that demonstrated photochemical reactions in film are directly related to fluctuations of $\overrightarrow{\mathcal{E}}$ and not $\overrightarrow{\mathcal{B}}$.

Unless otherwise stated, it is assumed that the direction of propagation, $\overrightarrow{\mathbf{k}}$, is in the $\hat{\mathbf{z}}$ direction. Therefore, $\overrightarrow{\mathcal{E}}$ and $\overrightarrow{\mathcal{B}}$ will be confined to the x-y plane. Polarization states arise from relationships between the magnitude and phase of the orthogonal components of $\overrightarrow{\mathcal{E}}$ (i.e. $\mathcal{E}_x$ and $\mathcal{E}_y$). The following sections discuss the various types of polarizations and the relationships between $\mathcal{E}_x$ and $\mathcal{E}_y$ required for each polarization state.

The most general form of polarized light is elliptical polarization. Linear and circular polarization are simply special degenerate cases of elliptical polarization. The types of polarization are introduced in the order of increasing mathematical complexity. The type of polarization is determined by the relative magnitude and phase difference between the two orthogonal components of $\overrightarrow{\boldsymbol{\mathcal{E}}}$. In general, $\overrightarrow{\boldsymbol{\mathcal{E}}}$ can be described mathematically by

$$\overrightarrow{\boldsymbol{\mathcal{E}}} = \mathcal{E}_x(z,t)\hat{\mathbf{x}} + \mathcal{E}_y(z,t)\hat{\mathbf{y}} \tag{3.1}$$

where $\mathcal{E}_x$ and $\mathcal{E}_y$ are given by

$$\mathcal{E}_x(z,t) = \mathcal{E}_{0x}\cos(\tau + \delta_x) \tag{3.2}$$

$$\mathcal{E}_y(z,t) = \mathcal{E}_{0y}\cos(\tau + \delta_y) \tag{3.3}$$

where $\tau = \omega t - kz$ is the propagation term. ω is the angular frequency i.e.

$$\omega = 2\pi f \tag{3.4}$$

where f is the temporal frequency. k is the wavenumber i.e.

$$k = \frac{2\pi}{\lambda} \tag{3.5}$$

and t is time. δ_x and δ_y are the phase angles of $\mathcal{E}_x$ and $\mathcal{E}_y$ respectively, and $\mathcal{E}_{0x}$ and $\mathcal{E}_{0y}$ are the peak magnitudes in the $\hat{\mathbf{x}}$ and $\hat{\mathbf{y}}$ directions.

3.1.2.1 Random Polarization

Randomly polarized light refers to light whose polarization is completely symmetric about the direction of propagation. The terms unpolarized and naturally polarized are often used to refer to randomly polarized light. It is important to note that the term unpolarized is a misnomer in that the E-field is always aligned in some particular

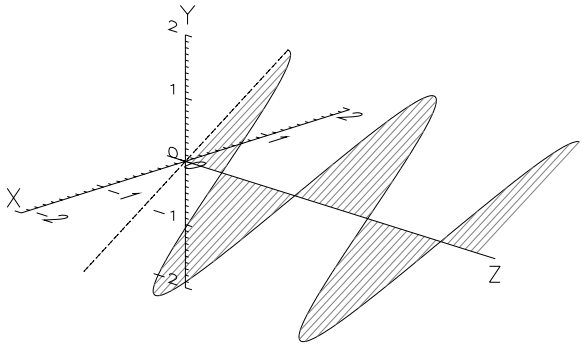

Figure 3.1: Example of linearly polarized light. $\overrightarrow{\mathcal{E}}$ is plotted along the direction of propagation. For simplicity, $\overrightarrow{\mathcal{B}}$, which is perpendicular to $\overrightarrow{\mathcal{E}}$ and $\overrightarrow{\mathbf{k}}$, was not plotted.

direction. In the case of random polarization, the direction of $\overrightarrow{\mathcal{E}}$ is changing rapidly and randomly. In fact it changes so rapidly that it is impossible with current technology to detect the direction of the E-field at any given point in time. Broadband solar radiation can be assumed to be randomly polarized (Coulson 1988; Uitenbroek 2000). Throughout this document, the terms randomly polarized, unpolarized, and natural polarization will be used interchangeably. However, the term randomly polarized will be favored since it more accurately describes the true nature of the polarization state.

3.1.2.2 Linear Polarization

The simplest form of polarized light is linear polarization. Light is said to be linearly polarized, or plane-polarized, when the electric field remains in a fixed plain that contains both $\overrightarrow{\mathcal{E}}$ and $\overrightarrow{\mathbf{k}}$. For light to be linearly polarized, the following has to hold true in equations (3.2) and (3.3):

$$\delta = \delta_x - \delta_y = 0 \tag{3.6}$$

Substituting equation (3.6) into equations (3.2) and (3.3) results in identical cosine terms for $\mathcal{E}_x$ and $\mathcal{E}_y$ and equation (3.1) becomes

$$\overrightarrow{\boldsymbol{\mathcal{E}}} = (\mathcal{E}_{0x}\hat{\mathbf{x}} + \mathcal{E}_{0y}\hat{\mathbf{y}})\cos(\tau + \delta) \tag{3.7}$$

Therefore, the ratio $\frac{\mathcal{E}_x}{\mathcal{E}_y}$ is a constant for linear polarized light. Actually, equation (3.6) is overly restrictive since $\delta = \pi$ also results in linearly polarized light. In this case, the cosine terms have the same magnitude but opposite signs and equation (3.1) can be written as

$$\overrightarrow{\boldsymbol{\mathcal{E}}} = (\mathcal{E}_{0x}\hat{\mathbf{x}} - \mathcal{E}_{0y}\hat{\mathbf{y}})\cos(\tau + \delta) \tag{3.8}$$

Figure 3.1 shows an example of linearly polarized light. Notice how the tip of $\overrightarrow{\boldsymbol{\mathcal{E}}}$ traces a straight line when projected to the $z = 0$ plane. If $\mathcal{E}_{0x} = 0$ the light is said to be vertically polarized since $\overrightarrow{\boldsymbol{\mathcal{E}}}$ oscillates in a vertical plane. Likewise, if $\mathcal{E}_{0y} = 0$, it is called horizontal polarization. Other forms of linear polarization are often referred to by the angle, α, between the plane of polarization and the x-z plane. This angle is given by:

$$\alpha = \arctan\left(\frac{\mathcal{E}_y}{\mathcal{E}_x}\right) \tag{3.9}$$

In section 3.1.2.4, α is related to ψ, the angle of rotation of the polarization ellipse.

3.1.2.3 Circular Polarization

The next simplest case is circular polarization which arises under the following conditions:

$$\mathcal{E}_{0x} = \mathcal{E}_{0y} \;=\; \mathcal{E}_0 \tag{3.10}$$

$$\delta = \frac{\pi}{2} + 2m\pi \qquad (m = 0, \pm 1, \pm 2, \dots) \tag{3.11}$$

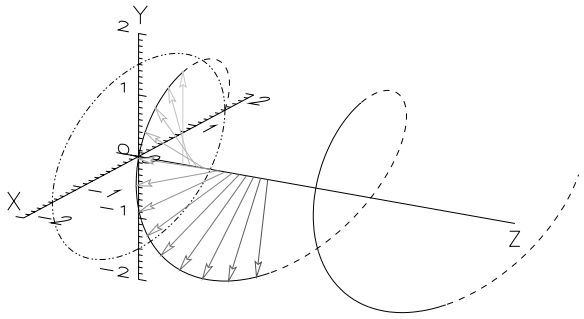

Figure 3.2: Example of right-hand circularly polarized light.

For circularly polarized light, equations (3.2) and (3.3) become

$$\mathcal{E}_x(z,t) = \mathcal{E}_0 \cos(\tau) \tag{3.12}$$

$$\mathcal{E}_y(z,t) = \mathcal{E}_0 \sin(\tau) \tag{3.13}$$

where δ_x has been arbitrarily set to zero without loss of generality. Combining equations (3.12) and (3.13) gives the following for equation (3.1)

$$\overrightarrow{\boldsymbol{\mathcal{E}}} = \mathcal{E}_0[\cos(\tau)\hat{\mathbf{x}} + \sin(\tau)\hat{\mathbf{y}}] \tag{3.14}$$

Notice that in the case of circular polarization, the magnitude of $\overrightarrow{\boldsymbol{\mathcal{E}}}$ remains constant ($|\overrightarrow{\boldsymbol{\mathcal{E}}}| = \mathcal{E}_0$) while the direction of $\overrightarrow{\boldsymbol{\mathcal{E}}}$ is time varying. This is the exact opposite of the case of linear polarization. Figure 3.2 shows an example of circularly polarized light. Notice how the tip of $\overrightarrow{\boldsymbol{\mathcal{E}}}$ traces a circle when projected to the $z = 0$ plane.

3.1.2.4 Elliptical Polarization

The most general case of polarization is elliptical polarization. In fact, linear and circular polarization are simply special cases of elliptical polarization. The name comes from the fact that the tip of $\overrightarrow{\boldsymbol{\mathcal{E}}}$ traces an ellipse, called the polarization ellipse,

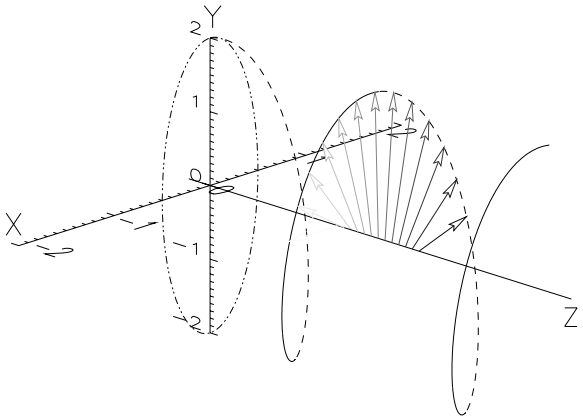

Figure 3.3: Example of left-hand elliptically polarized light.

when projected to the $z = 0$ plane (see figure 3.3). In the case of elliptical polarization, both the magnitude and direction of $\overrightarrow{\boldsymbol{\mathcal{E}}}$ are time varying.

There are several parameters which can be used to describe the polarization ellipse. The choice of parameters often depends on the specific application. Figure 3.4 shows a generic polarization ellipse with its major and minor axes (x' and y') rotated from the reference axes (x and y). The equation for the polarization ellipse has the following form (Collett 1993)

$$\frac{\mathcal{E}_x^2}{\mathcal{E}_{0x}^2} + \frac{\mathcal{E}_y^2}{\mathcal{E}_{0y}^2} - \frac{2\mathcal{E}_x\mathcal{E}_y\cos\delta}{\mathcal{E}_{0x}\mathcal{E}_{0y}} = \sin^2\delta \tag{3.15}$$

which shows that the polarization can be characterized in terms of the parameters $\mathcal{E}_{0y}$, $\mathcal{E}_{0y}$, and δ. Figure 3.4 indicates that the polarization can also be characterized by the ellipse rotation angle, ψ, and the major and minor axes, a and b. Using the standard equation of an ellipse, Collett derives the following relationship between ψ and the parameters $\mathcal{E}_{0x}$, $\mathcal{E}_{0y}$, and δ

$$\tan 2\psi = \frac{2\mathcal{E}_{0x}\mathcal{E}_{0y}\cos\delta}{\mathcal{E}_{0x}^2 - \mathcal{E}_{0y}^2} \tag{3.16}$$

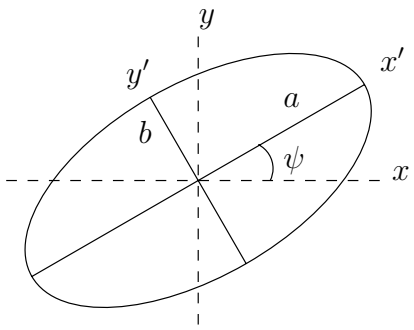

Figure 3.4: Polarization Ellipse

He also derives the relationship between ψ, α, and δ

$$\tan 2\psi = (\tan 2\alpha)\cos\delta \tag{3.17}$$

In the case of linear polarization ($\delta = 0$ or π) equation (3.17) reduces to

$$\psi = \pm\alpha \tag{3.18}$$

In the case of circular polarization ($\delta = \frac{\pi}{2}$ or $\frac{3\pi}{2}$) equation (3.17) reduces to $\phi = 0$ indicating that there is no rotation. This makes sense since a circle is rotationally symmetric.

Finally, the angle of ellipticity, χ, is defined as

$$\tan\chi = \frac{\pm b}{a} \qquad -\frac{\pi}{4} \leq \chi \leq \frac{\pi}{4} \tag{3.19}$$

where a and b, the major and minor axis, are given by

$$a = \sqrt{\mathcal{E}_{0x}^2\cos^2\psi + \mathcal{E}_{0y}^2\sin^2\psi + 2\mathcal{E}_{0x}\mathcal{E}_{0y}\cos\psi\sin\psi\cos\delta} \tag{3.20}$$

$$b = \sqrt{\mathcal{E}_{0x}^2\sin^2\psi + \mathcal{E}_{0y}^2\cos^2\psi - 2\mathcal{E}_{0x}\mathcal{E}_{0y}\cos\psi\sin\psi\cos\delta} \tag{3.21}$$

Linearly polarized light has no minor axis, thus $b = 0$ and from equation (3.19) $\chi = 0$. In the case of circularly polarized light, the two axis are equal lengths, thus $a = b$

which means $\chi = \pm\frac{\pi}{4}$. Collett (1993) has shown the following relationship between χ and the elliptical parameters $\mathcal{E}_{0x}$, $\mathcal{E}_{0y}$, and δ

$$\sin 2\chi = \frac{2\mathcal{E}_{0x}\mathcal{E}_{0y}}{\mathcal{E}_{0x}^2 + \mathcal{E}_{0y}^2} = (\sin 2\alpha)\sin\delta \tag{3.22}$$

In summary, the polarization ellipse, is fully characterized using either the elliptical parameters $\mathcal{E}_{0x}$, $\mathcal{E}_{0y}$, and δ or by the ellipticity and orientation angles χ and ψ.

3.1.2.5 Right-Handed vs. Left-Handed Polarization

In the cases of elliptical and circular polarization, one must also indicate whether it is right or left handed. Right versus left handed refers to whether $\overrightarrow{\mathcal{E}}$ rotates clockwise or counterclockwise. The classical definition is based on an observer looking back at the source of the radiation. The polarization is said to be *right-handed* when the tip of $\overrightarrow{\mathcal{E}}$ appears to rotate *counterclockwise* (see figure 3.2). Conversely, for *left-handed* polarization, the tip of $\overrightarrow{\mathcal{E}}$ appears to rotate *clockwise* (see figure 3.3). The values of δ and χ can be used to determine the handedness of the polarization.

Right-handed:	$\delta > 0$	$0 < \chi \leq \frac{\pi}{4}$
Left-handed:	$\delta < 0$	$-\frac{\pi}{4} \leq \chi < 0$

3.1.3 Polarization Mathematics

The previous sections describe the various types of polarization. The following sections discuss the various mathematical tools developed by Stokes, Mueller, and others to deal with the propagation and interaction of polarized radiance. The Stokes vectors provide a simple and compact method of describing the polarization state while the Mueller matrices provide a tool for relating incoming radiance to outgoing radiance at various interfaces.

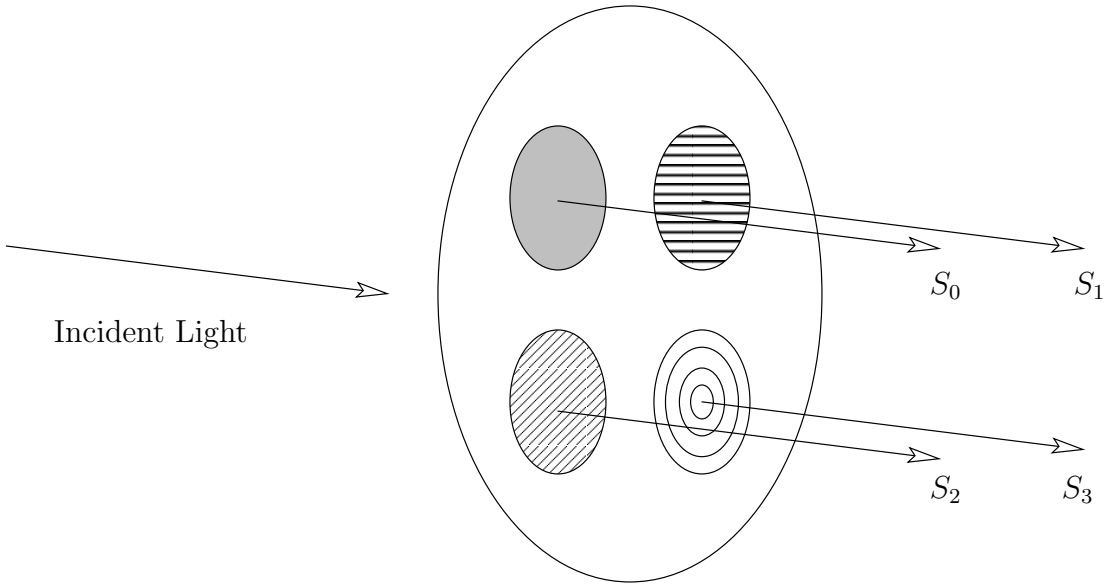

Figure 3.5: Example of measuring Stokes parameters using four filters.

3.1.3.1 Stokes Parameters

A major limitation of the polarization ellipse equations is the ability to only describe fully polarized light. Another limitation arises from the fact that the fluctuations described by the polarization ellipse equations occur with a time scale on the order of 10^{-15} seconds. As such, they cannot be directly observed. Instead all we can measure is average values. Therefore, it would be useful to use a system that describes the polarized radiance using observable quantities. Sir George Gabriel Stokes developed a method for fully describing any state of polarization ranging from completely randomly polarized to fully polarized. These four parameters, now referred to as the Stokes parameters or Stokes vector, were made popular by Chandrasekhar in his famous formulation of the radiative transfer of scattered, partially polarized light.

The Stokes parameters can be defined in terms of the transmitted irradiance from

a set of four filters (see figure 3.5). For a completely randomly polarized radiance field, each of the filters transmits exactly half the radiance. The first filter is a 50% neutral density filter; therefore, the transmitted radiance is also completely randomly polarized. The second and third filters are linear polarizers. The second filter is aligned to transmit horizontally polarized light. The third filter has its plane of polarization aligned at a 45° angle (i.e. diagonally between quadrants I and III as viewed looking back at the source). The last filter is a right-hand circular filter. The Stokes parameters are then defined as

$$S_0 = 2I_0 \tag{3.23}$$

$$S_1 = 2(I_1 - I_0) \tag{3.24}$$

$$S_2 = 2(I_2 - I_0) \tag{3.25}$$

$$S_3 = 2(I_3 - I_0) \tag{3.26}$$

where I_{0-3} are the transmitted irradiances that would be measured using the four filters. The S_n notation is the new standard for specifying the Stokes parameters. Some literature uses I, Q, U, and V to represent S_0 through S_3 respectively. It is useful to note that S_0 is equivalent to the incident irradiance. The other three parameters characterize the polarization state. The signs on S_1 through S_3 indicate which types of polarization are dominant. Table 3.1 lists the meanings of the sign convention for the stokes parameters.

Collett (1993) formally derives the four Stokes parameters from the polarization ellipse equations. This results in the following equivalent definition of the the Stokes

Parameter	Positive	Negative
S_1	Horizontal dominates	Vertical dominates
S_2	+45° dominates	-45° dominates
S_3	Right-hand circular dominates	Left-hand circular dominates

Table 3.1: Characterization of the polarization state based on the signs of the Stokes parameters.

parameters

$$S_0 = \left\langle \mathcal{E}_x^2 \right\rangle + \left\langle \mathcal{E}_y^2 \right\rangle \tag{3.27}$$

$$S_1 = \left\langle \mathcal{E}_x^2 \right\rangle - \left\langle \mathcal{E}_y^2 \right\rangle \tag{3.28}$$

$$S_2 = 2\left\langle \mathcal{E}_x^2 \mathcal{E}_y^2 \cos\delta \right\rangle \tag{3.29}$$

$$S_3 = 2\left\langle \mathcal{E}_x^2 \mathcal{E}_y^2 \sin\delta \right\rangle \tag{3.30}$$

where the symbol $\langle \cdots \rangle$ represents the time average over one period. Assuming perfectly monochromatic light and substituting the values for the time averages in (3.27) through (3.30) results in the following equations

$$S_0 = \mathcal{E}_{0x}^2 + \mathcal{E}_{0y}^2 \tag{3.31}$$

$$S_1 = \mathcal{E}_{0x}^2 - \mathcal{E}_{0y}^2 \tag{3.32}$$

$$S_2 = 2\mathcal{E}_{0x}\mathcal{E}_{0y}\cos\delta \tag{3.33}$$

$$S_3 = 2\mathcal{E}_{0x}\mathcal{E}_{0y}\sin\delta \tag{3.34}$$

From which the following relationship holds for completely polarized light

$$S_0^2 = S_1^2 + S_2^2 + S_3^2 \tag{3.35}$$

In general, the following inequality holds for any polarization state

$$S_0^2 \geq S_1^2 + S_2^2 + S_3^2 \tag{3.36}$$

which indicates the sum of the polarized intensity cannot exceed the total intensity. The degree of polarization (DoP), P is defined as

$$P = \frac{I_{pol}}{I_{total}} = \frac{\sqrt{S_1^2 + S_2^2 + S_3^2}}{S_0} \qquad 0 \leq P \leq 1 \tag{3.37}$$

where I_{pol} is the sum of the intensity of the polarized light and I_{total} is the total intensity. The degree of linear polarization (DoLP) is defined as

$$P_{lin} = \frac{I_{linear}}{I_{total}} = \frac{\sqrt{S_1^2 + S_2^2}}{S_0} \qquad 0 \leq P \leq 1 \tag{3.38}$$

where I_{linear} is the sum of the intensity of the linearly polarized light.

Since all of the Stokes parameters are measures of intensity, the superposition of monochromatic waves results in a polarization state that is simply the sum of the component Stokes parameters.

3.1.3.2 Stokes Vectors

The four Stokes parameters can be combined in a 4×1 column matrix to form what is called the Stokes vector. Technically, it is a matrix and not a vector. However, it is still most commonly called a vector. The Stokes vector is written as

$$\mathbf{S} = \begin{pmatrix} S_0 \\ S_1 \\ S_2 \\ S_3 \end{pmatrix} \tag{3.39}$$

The Stokes vector is often normalized by S_0 to result in a vector representing unit irradiance. Table 3.2 lists the normalized Stokes vectors for some simple polarization

Polarization State	Symbol	Stokes Vector	Polarization State	Symbol	Stokes Vector
Horizontal	$\leftrightarrow$	$\begin{pmatrix}1\\1\\0\\0\end{pmatrix}$	Vertical	$\updownarrow$	$\begin{pmatrix}1\\-1\\0\\0\end{pmatrix}$
Linear +45°	$\nearrow\!\!\swarrow$	$\begin{pmatrix}1\\0\\1\\0\end{pmatrix}$	Linear -45°	$\nwarrow\!\!\searrow$	$\begin{pmatrix}1\\0\\-1\\0\end{pmatrix}$
Right-hand circular	$\circlearrowright$	$\begin{pmatrix}1\\0\\0\\1\end{pmatrix}$	Left-hand circular	$\circlearrowleft$	$\begin{pmatrix}1\\0\\0\\-1\end{pmatrix}$
Random	$*$	$\begin{pmatrix}1\\0\\0\\0\end{pmatrix}$			

Table 3.2: Stokes vectors

states. The Stokes vector can also be represented in terms of α and δ or χ and ψ

$$\mathbf{S} = \begin{pmatrix} 1 \\ \cos 2\alpha \\ \sin 2\alpha \cos \delta \\ \sin 2\alpha \sin \delta \end{pmatrix} = \begin{pmatrix} 1 \\ \cos 2\chi \cos 2\psi \\ \cos 2\chi \sin 2\psi \\ \sin 2\chi \end{pmatrix} \tag{3.40}$$

By combining equations (3.39) and (3.40) and solving the resulting system of equations it is possible to derive the following expressions for the various polarization

ellipse parameters

$$\alpha = \cos^{-1} S_2 \tag{3.41}$$

$$\delta = \cos^{-1}\left[\frac{S_3}{\sqrt{1-S_2^2}}\right] \tag{3.42}$$

$$\chi = \frac{\sin^{-1} S_4}{2} \tag{3.43}$$

$$\psi = \frac{1}{2}\ \cos^{-1}\left[\frac{S_2}{\sqrt{1-S_4^2}}\right] \tag{3.44}$$

Figure 3.7 shows how the polarization ellipse changes from circular polarization to linear polarization as the value of χ ranges from 0° to 45°. The rotation of the polarization ellipse as a function of ψ is also shown.

The superposition of two monochromatic waves represented by the Stokes vectors $\mathbf{S_a}$ and $\mathbf{S_b}$ is the vector sum of the two Stokes vectors

$$\mathbf{S_{tot}} = \mathbf{S_a} + \mathbf{S_b} = \begin{pmatrix} S_{a0} \\ S_{a1} \\ S_{a2} \\ S_{a3} \end{pmatrix} + \begin{pmatrix} S_{b0} \\ S_{b1} \\ S_{b2} \\ S_{b3} \end{pmatrix} = \begin{pmatrix} S_{a0}+S_{b0} \\ S_{a1}+S_{b1} \\ S_{a2}+S_{b2} \\ S_{a3}+S_{b3} \end{pmatrix} \tag{3.45}$$

3.1.3.3 Mueller Matrix Calculus

The Stokes vectors presented in the previous section provide a powerful mathematical tool for characterizing the polarization state of light waves. Using vector addition the Stokes vectors also describe the results of combining multiple rays of

Figure 3.6: Simple model of an optical system.

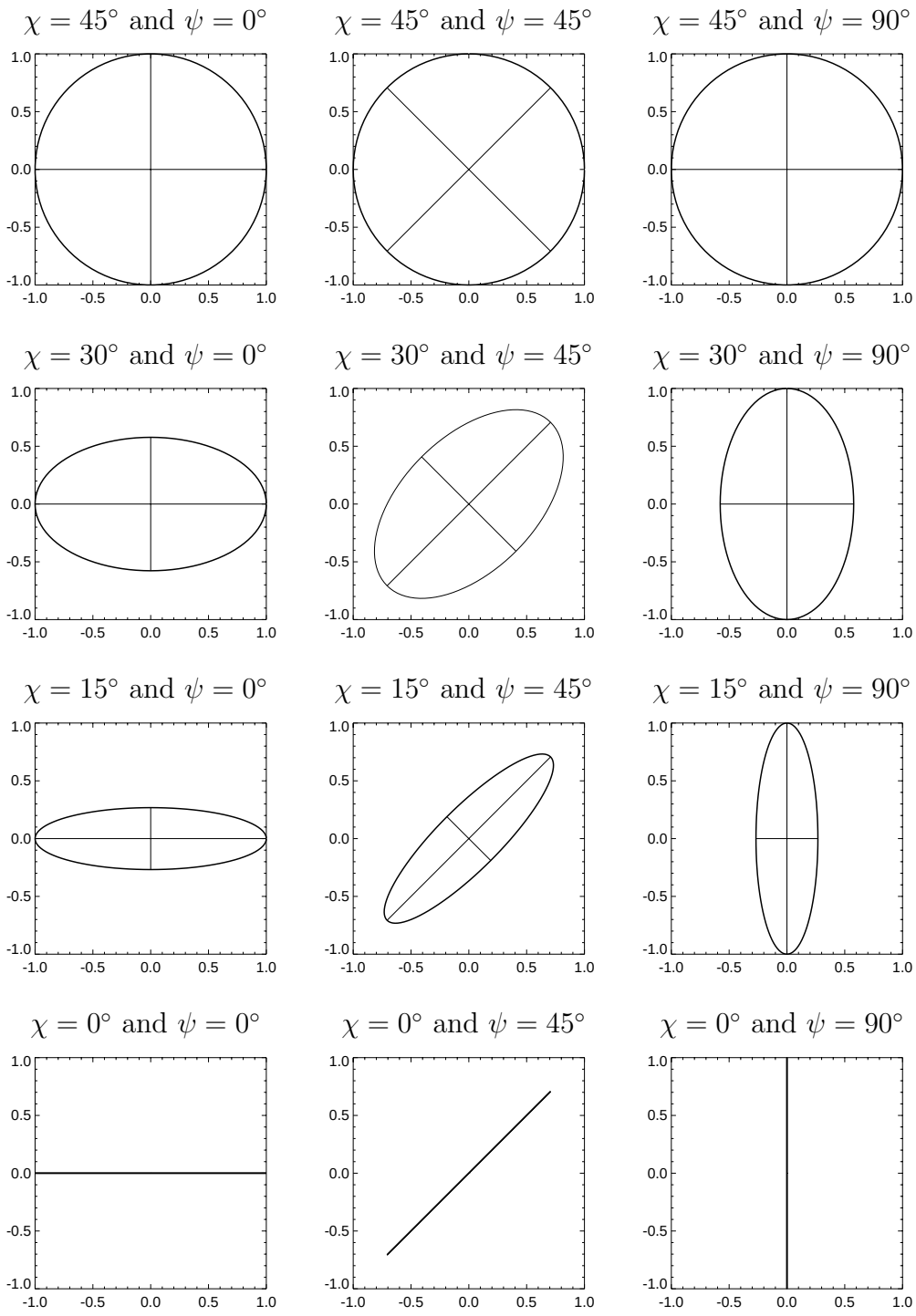

Figure 3.7: Various polarization ellipses.

light. Therefore, it would be useful to have a mathematical tool which describes how the Stokes vector changes as a result of interactions with various optical "systems". Here the term system refers to any mechanism by which the polarization state of a ray is changed as shown in figure 3.6. For example, a system could be as simple as a polarized filter, a quarter wave plate, or reflection from a surface. A system can also be as complex as an entire optical system like a telescope.

Mueller introduced the concept of using a 4×4 matrix to represent the relationship between the incident, $\mathbf{S_{in}}$, and final, $\mathbf{S_{out}}$, polarization states. The Mueller matrix, $\mathbf{M}$, relates the output Stokes parameters, $\mathbf{S_{out}}$, as a linear combination of the input Stokes parameters, $\mathbf{S_{in}}$. The system in figure 3.6 can be represented mathematically with the following matrix equation

$$\mathbf{S_{out}} = \mathbf{M} \cdot \mathbf{S_{in}} \tag{3.46}$$

A cascaded system results in a series of matrix multiplications. Care must be taken to perform the multiplications in the correct order since matrix multiplication is not commutative. The matrix equation for an arbitrary number of cascaded systems is

$$\mathbf{S_{out}} = \mathbf{M_n} \cdots \mathbf{M_2} \cdot \mathbf{M_1} \cdot \mathbf{S_{in}} \tag{3.47}$$

where $\mathbf{M_1}$ and $\mathbf{M_n}$ correspond to the first and last optical systems respectively.

Often it is necessary to rewrite a Stokes vector using a new set of reference axes. This can be accomplished using the Mueller matrix associated with a rotation of the reference coordinate system by the angle θ i.e.;

$$\mathbf{M_{rot}}(\theta) = \begin{pmatrix} 1 & 0 & 0 & 0 \\ 0 & \cos 2\theta & \sin 2\theta & 0 \\ 0 & -\sin 2\theta & \cos 2\theta & 0 \\ 0 & 0 & 0 & 1 \end{pmatrix} \tag{3.48}$$

Optical System	Mueller Matrix	Optical System	Mueller Matrix
Horizontal linear polarizer	$\frac{1}{2}\begin{pmatrix} 1 & 1 & 0 & 0 \\ 1 & 1 & 0 & 0 \\ 0 & 0 & 0 & 0 \\ 0 & 0 & 0 & 0 \end{pmatrix}$	Vertical linear polarizer	$\frac{1}{2}\begin{pmatrix} 1 & -1 & 0 & 0 \\ -1 & 1 & 0 & 0 \\ 0 & 0 & 0 & 0 \\ 0 & 0 & 0 & 0 \end{pmatrix}$
45° linear polarizer	$\frac{1}{2}\begin{pmatrix} 1 & 0 & 1 & 0 \\ 0 & 0 & 0 & 0 \\ 1 & 0 & 1 & 0 \\ 0 & 0 & 0 & 0 \end{pmatrix}$	-45° linear polarizer	$\frac{1}{2}\begin{pmatrix} 1 & 0 & -1 & 0 \\ 0 & 0 & 0 & 0 \\ -1 & 0 & 1 & 0 \\ 0 & 0 & 0 & 0 \end{pmatrix}$
Quarter-wave plate, fast axis vertical	$\begin{pmatrix} 1 & 0 & 0 & 0 \\ 0 & 1 & 0 & 0 \\ 0 & 0 & 0 & -1 \\ 0 & 0 & 1 & 0 \end{pmatrix}$	Quarter-wave plate, fast axis horizontal	$\begin{pmatrix} 1 & 0 & 0 & 0 \\ 0 & 1 & 0 & 0 \\ 0 & 0 & 0 & 1 \\ 0 & 0 & -1 & 0 \end{pmatrix}$
Right circular polarizer	$\frac{1}{2}\begin{pmatrix} 1 & 0 & 0 & 1 \\ 0 & 0 & 0 & 0 \\ 0 & 0 & 0 & 0 \\ 1 & 0 & 0 & 1 \end{pmatrix}$	Left circular polarizer	$\frac{1}{2}\begin{pmatrix} 1 & 0 & 0 & -1 \\ 0 & 0 & 0 & 0 \\ 0 & 0 & 0 & 0 \\ -1 & 0 & 0 & 1 \end{pmatrix}$

Table 3.3: Some standard Mueller matrices.

It will be shown later how the polarized form of the bidirectional reflectance distribution function (BRDF) can be expressed as a Mueller matrix. Table 3.3 lists the Mueller matrices for some simple, ideal optical systems.

3.1.4 Additional Polarization Information

For more in depth information on polarization, the reader is referred to texts by Brosseau (1998), Collett (1993), Coulson (1988), and Hecht (1990). Hecht's book is a standard text on optics as a whole. He dedicates an entire chapter to the general

topic of polarization. Brosseau and Collett both cover classical and quantum theories of light. Collett rigorously derives many of the relationships presented in this section. Coulson's book is dedicated to the interaction of polarized light and the atmosphere.

3.2 Light-Matter Interactions

This section deals with the physics involved when light interacts with matter at a boundary. A review of the classical unpolarized case is presented first followed by an expansion to the polarized case. An accurate characterization of how the polarization state changes as light interacts with various materials plays a key role in generating realistic polarimetric synthetic imagery.

3.2.1 Geometrical Optics

When light strikes a boundary between two different materials (i.e. air and glass), three things can happen. The light could be reflected, transmitted (i.e. refracted), or absorbed. All three of these events can occur to varying degrees depending on a wide range of factors involving geometry, material properties, and the wavelength of the light to name a few. The theory of geometrical optics, covered in most introductory physics text books, can be used to describe these interactions. Geometrical optics assumes that the propagation of light can be approximated using rays. One of the major weaknesses of geometrical optics is the inability to describe the non-rectilinear motion of light, in other words, diffraction. Geometrical optics provides an adequate set of tools for most remote sensing applications.

3.2.1.1 Law of Reflection

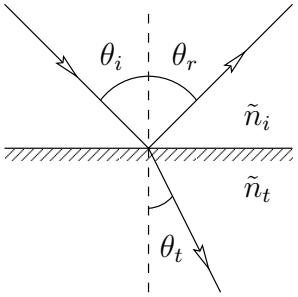

Figure 3.8: Geometry used for the laws of reflection and refraction.

Definition. *Reflection* is the process by which electromagnetic flux, or power, incident on a stationary surface or medium, leaves that surface or medium from the incident side without change in frequency (Nicodemus et al. 1992).

Definition. *Reflectance* is the fraction of the incident flux that is reflected (Nicodemus et al. 1992).

The well known law of reflection states that for an optically smooth, specular surface, the angle of the reflected ray, θ_r, equals the angle of the incident ray, θ_i (see figure 3.8). The requirements of optically smooth and specular restricts the applicability of this law to a very small set of materials. However, this law will be the foundation for other theories and models which describe reflections from rough and non-specular surfaces.

3.2.1.2 Law of Refraction

Definition. *Refraction* is the change of direction of propagation of any wave, such as an electromagnetic or sound wave, when it passes from one medium to another in which the wave velocity is different, or when there is a spatial variation in a medium's wave velocity (Parker 1989).

Fermat's principle, which states that a ray of light travels the quickest path between two points, can be used to determine the angle of the refracted, or transmitted, ray, θ_t. This relationship is known as Snell's law

$$n_i \sin\theta_i = n_t \sin\theta_t \tag{3.49}$$

where n_i and n_t are the real parts of the complex indices of refraction, $\tilde{n_i}$ and $\tilde{n_t}$. Once again, this applies for the case of an optically smooth interface.

3.2.1.3 Fresnel Equations

The laws of reflection and refraction dictate the direction of the reflected and transmitted rays. The Fresnel equations indicate how the energy is distributed between the reflected and transmitted waves. There are separate equations for the parallel and perpendicular components of $\overrightarrow{\boldsymbol{\mathcal{E}}}$. The amplitude reflection coefficients ($r_{||}$ and $r_{\perp}$) relate the magnitudes of the reflected field to the incident field. The amplitude transmission coefficients ($t_{||}$ and $t_{\perp}$) relate the magnitudes of the transmitted field to the incident field. However, when dealing with reflected and transmitted power, it is necessary to use the equations for reflectance (R) and transmittance (T) which are given in equations (3.58) through (3.63).

The two amplitude reflection coefficients are

$$r_{||} = \frac{\tilde{n_t}\cos\theta_i - \tilde{n_i}\cos\theta_t}{\tilde{n_i}\cos\theta_t + \tilde{n_t}\cos\theta_i} \tag{3.50}$$

$$r_{\perp} = \frac{\tilde{n_i}\cos\theta_i - \tilde{n_t}\cos\theta_t}{\tilde{n_i}\cos\theta_i + \tilde{n_t}\cos\theta_t} \tag{3.51}$$

where $\tilde{n}$ is the complex index of refraction, i and t indicate the incident and transmitted mediums. θ_i and θ_t are the incident and transmitted angles respectively. The two amplitude transmission coefficients are

$$t_{||} = \frac{2n_i \cos\theta_i}{\tilde{n_i}\cos\theta_t + \tilde{n_t}\cos\theta_i} \tag{3.52}$$

$$t_{\perp} = \frac{2n_i \cos\theta_i}{\tilde{n_i}\cos\theta_i + \tilde{n_t}\cos\theta_t} \tag{3.53}$$

Applying Snell's law, equations (3.50) through (3.53) become

$$r_{||} = \frac{\tan(\theta_i - \theta_t)}{\tan(\theta_i + \theta_t)} \tag{3.54}$$

$$r_{\perp} = -\frac{\sin(\theta_i - \theta_t)}{\sin(\theta_i + \theta_t)} \tag{3.55}$$

$$t_{||} = \frac{2\sin\theta_t \cos\theta_i}{\sin(\theta_i + \theta_t)\cos(\theta_i - \theta_t)} \tag{3.56}$$

$$t_{\perp} = \frac{2\sin\theta_t \cos\theta_i}{\sin(\theta_i + \theta_t)} \tag{3.57}$$

Combining the Fresnel amplitude coefficients with the definitions of reflectance, R, and transmittance, T,

$$R \equiv \frac{\Phi_r}{\Phi_i} = \frac{I_r \cos\theta_r}{I_i \cos\theta_i} = \frac{I_r}{I_i} \tag{3.58}$$

$$T \equiv \frac{\Phi_t}{\Phi_i} = \frac{I_t \cos\theta_t}{I_i \cos\theta_i} \tag{3.59}$$

yields the following equations

$$R_{||} = r_{||}^2 \tag{3.60}$$

$$R_{\perp} = r_{\perp}^2 \tag{3.61}$$

$$T_{||} = \left(\frac{n_t \cos\theta_t}{n_i \cos\theta_i}\right) t_{||}^2 \tag{3.62}$$

$$T_{\perp} = \left(\frac{n_t \cos\theta_t}{n_i \cos\theta_i}\right) t_{\perp}^2 \tag{3.63}$$

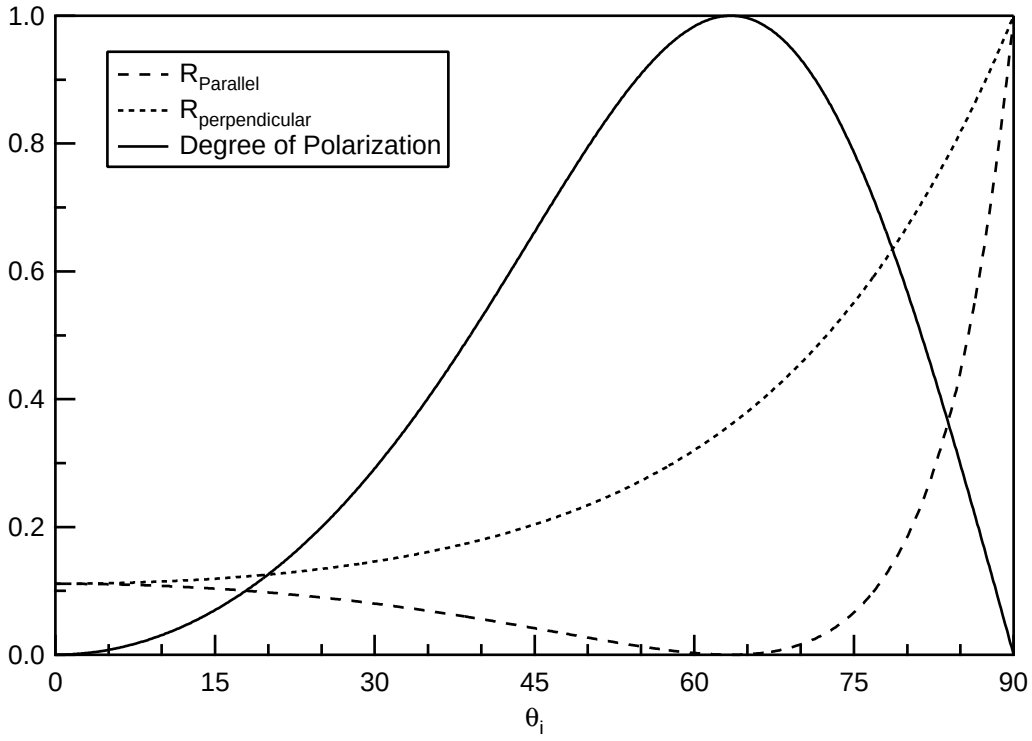

Figure 3.9: Degree of polarization of the reflected light and Fresnel reflection coefficients for $n_i = 1.0$ and $n_t = 2.0$ as a function of the incident zenith angle.

The relationship

$$R + T = 1 \tag{3.64}$$

holds true at the component level, thus

$$R_{||} + T_{||} = 1 \tag{3.65}$$

$$R_{\perp} + T_{\perp} = 1 \tag{3.66}$$

Differences between the values of $R_{||}$ and $R_{\perp}$ (and therefore $T_{||}$ and $T_{\perp}$ by way of equations (3.65) and (3.66)) for a given geometry lead to changes in polarization upon reflection and transmission. Figure 3.9 shows this effect for randomly polarized light being reflected from a dielectric with $n = 2.0$. Notice how the degree of polarization

is nonzero everywhere except at normal and grazing incidence. It increases to a maximum value of 1.0 at the brewster angle.

Later, the laws of reflection and refraction and the Fresnel equations will be combined to model the polarimetric characteristics of light interacting with a wide range of materials and surface characteristics. First, it is necessary to establish the nomenclature and definitions which describe non-specular reflections.

3.2.2 Non-Specular Reflection

The previous section presented the basics of specular reflection and transmission. A perfectly specular reflector is an ideal case which cannot be realized in the real world. At the opposite end of the scale lies a perfectly diffuse reflector which is equally unrealizable. Where a specular surface reflects all incident light from a given direction in a single outbound direction (see figure 3.10(a)), a perfectly diffuse surface distributes the reflected light in all directions equally (see figure 3.10(b)). Real surfaces lie somewhere in between the two extremes. Figure 3.10 shows some of the possible variations. Notice that cases exist which are not simple "interpolations" of the two extremes (see figure 3.10(c)).

3.2.2.1 Unpolarized Bidirectional Reflectance Distribution Function

The bidirectional reflectance distribution function (BRDF), as defined by Nicodemus et al. (1992), is the mechanism used to describe reflections for all possible combinations of incident and reflected geometries. It is necessary to understand the BRDF in terms of unpolarized radiative transfer before extending it to the polarized case.

Figure 3.11 shows the geometry used by Nicodemus et al. (1992) to define the

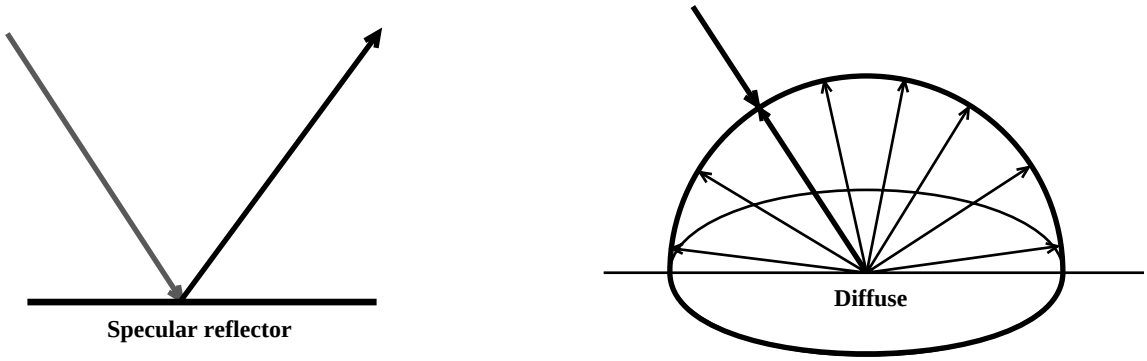

(a) Specular Reflector

(b) Diffuse

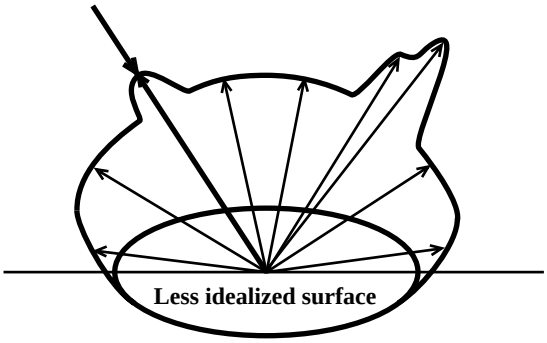

(c) Less idealized surface

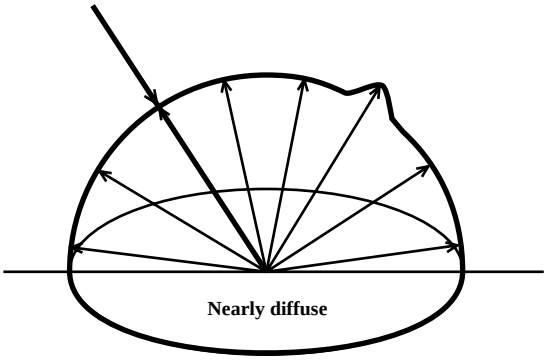

(d) Nearly Diffuse

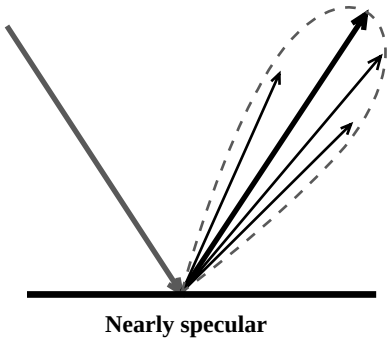

(e) Nearly Specular

Figure 3.10: Reflectance characteristics of some simple materials. Figures courtesy of Schott (1997, pg. 100).

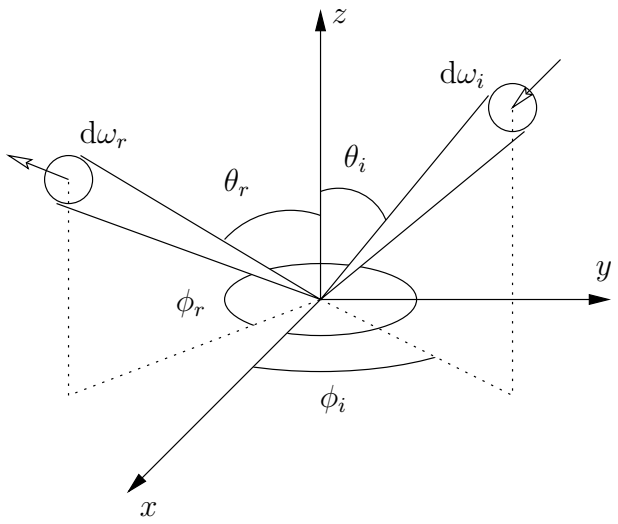

Figure 3.11: BRDF geometry

BRDF and related quantities. The BRDF is defined as the ratio of the scattered radiance to the incident irradiance

$$f \equiv \frac{L(\theta_r, \phi_r)}{E(\theta_i, \phi_i)} \left[sr^{-1}\right] \tag{3.67}$$

In general, the BRDF is a function of all four geometry angles. However, in the case of isotropic reflectors, the circular symmetry introduces redundancy which can be eliminated by expressing the BRDF as a function of the two zenith angles and the difference of the two azimuth angles. Since the BRDF is a ratio of radiance to irradiance, it can take on values ranging from zero to infinity. Highly specular materials will have large BRDF values in the specular direction since the reflected radiance is distributed over a small solid angle. Integrating the BRDF over the entire hemisphere results in a quantity called the directional hemispherical reflectance (DHR)

$$DHR = \int_{2\pi} f \cos\theta_r \, d\omega_r \tag{3.68}$$

The DHR is a unitless quantity limited to the range 0 to 1 inclusive. The DHR indicates how much of the total incident flux from a particular direction is reflected into the hemisphere. Due to reciprocity, the DHR can be measured in one of two ways. The first method uses full hemispherical illumination and measures the reflected flux in a particular direction (i.e. θ_r and ϕ_r). The second method illuminates from a single direction (i.e. θ_i and ϕ_i) and measures the reflected flux over the entire hemisphere. The second method is the preferred experimental approach since it is easier to perform.

A close relative of the BRDF is the bidirectional reflectance factor (BDRF).

> **Definition.** *BDRF* is the ratio of the radiance reflected into a particular direction to the radiance that would be reflected into the same direction by a perfect Lambertian radiator illuminated in an identical fashion (Schott 1997).

Feng et al. (1993) derive the following simple relationship between the BRDF and the BDRF

$$f = \frac{\rho(\theta_i, \phi_i; 2\pi)}{\pi} \tag{3.69}$$

where $\rho(\theta_i, \phi_i; 2\pi)$ is recommended nomenclature for the BRDF as given by Nicodemus et al. (1992). The BDRF is a unitless quantity because the π in the denominator has units of sr.

3.2.2.2 Polarized Bidirectional Reflectance Distribution Function

he definitions in the previous section work well when one ignores the polarization state of the light and deals only with the total radiance. However, when dealing with polarized (or partially polarized) light, the scalar radiometric quantities become Stokes vectors. This adds a dimension of complexity when describing the possible interactions of light with a surface boundary. It was shown in section 3.2.1.3 that

reflection from a smooth dielectric surface almost always changes the polarization state. Therefore it should not be surprising that the polarimetric version of the BRDF will have to account for interactions between all four Stokes parameters of the incident and reflected light.

Flynn and Alexander (1995) indicate the unpolarized BRDF equation

$$dL = f dE \tag{3.70}$$

becomes the matrix equation

$$d\mathbf{L} = \boldsymbol{f} d\mathbf{E} \tag{3.71}$$

where $\mathbf{L}$ and $\mathbf{E}$ are the radiance and irradiance Stokes vectors

$$\mathbf{E} = E_i \mathbf{S_i} \tag{3.72}$$

$$\mathbf{L} = L_o \mathbf{S_o} \tag{3.73}$$

$$\tag{3.74}$$

where E_i is the total incident irradiance and $\mathbf{S_i}$ is the normalized Stokes vector of the incident irradiance. Similarly, L_i is the total reflected radiance and $\mathbf{S_o}$ is the normalized Stokes vector of the reflected radiance. $\boldsymbol{f}$ is Mueller matrix analagous to the BRDF. The order of multiplication in equation (3.71) is important because matrix multiplication does not commutate.

Equation (3.71) gives the following equation for the first element of $\mathbf{L}$, which corresponds to the total radiance,

$$dL_1 = f_{11} dE_1 + (f_{12} dE_2 + f_{13} dE_3 + f_{14} dE_4) \tag{3.75}$$

where f_{rc} is the value in the r^{th} row and c^{th} column. The terms in parenthesis are the added polarimetric complexity. If all the terms in parenthesis are zero, then equation

(3.75) reduces to equation (3.70). This is the case for randomly polarized irradiance or completely depolarizing surfaces. However, the remaining elements of $\mathbf{L}$ can be nonzero for the randomly polarized irradiance case.

3.2.3 Mueller Matrices for Reflections

Collett (1993) derives the Mueller matrices for first surface reflections from dielectric and metal surfaces. For dielectrics, the Mueller matrix is

$$\mathbf{M} = \frac{1}{2}\left(\frac{\tan\alpha_-}{\sin\alpha_+}\right)^2 \times \begin{pmatrix} \cos^2\alpha_- + \cos^2\alpha_+ & \cos^2\alpha_- - \cos^2\alpha_+ & 0 & 0 \\ \cos^2\alpha_- - \cos^2\alpha_+ & \cos^2\alpha_- + \cos^2\alpha_+ & 0 & 0 \\ 0 & 0 & -2\cos\alpha_+\cos\alpha_- & 0 \\ 0 & 0 & 0 & -2\cos\alpha_+\cos\alpha_- \end{pmatrix} \tag{3.76}$$

where $\alpha_\pm = \theta_i \pm \theta_r$ and θ_i and θ_r are the incident and reflected angles respectively. The Mueller matrix for metal surfaces is

$$\mathbf{M} = \frac{1}{2}\begin{pmatrix} r_\perp^2 + r_{||}^2 & r_\perp^2 - r_{||}^2 & 0 & 0 \\ r_\perp^2 - r_{||}^2 & r_\perp^2 + r_{||}^2 & 0 & 0 \\ 0 & 0 & 2r_\perp r_{||}\cos\Delta & -2r_\perp r_{||}\sin\Delta \\ 0 & 0 & 2r_\perp r_{||}\sin\Delta & 2r_\perp r_{||}\cos\Delta \end{pmatrix} \tag{3.77}$$

where $\Delta = \phi_\perp - \phi_{||}$. $\phi_\perp$ and $\phi_{||}$ are the phase changes for the out-of-plane of incidence and the in-plane of incidence polarizations respectively. These phase changes can be nonzero since the index of refraction for metals is a complex number. Combining equations (3.50), (3.51), and (3.77) and recognizing that $\Delta = 0$ for reflections from dielectrics, it can be shown that equation (3.76) is just a special case of the the more general equation for metallic reflections.

3.2.4 Mueller Matrix for Transmission

Collett (1993) also derives the following Mueller matrix for transmission through a dielectric boundary

$$\mathbf{M} = \frac{\sin 2\theta_i \sin 2\theta_t}{2\left(\sin\alpha_+ \cos\alpha_-\right)^2} \times \begin{pmatrix} \cos^2\alpha_- + 1 & \cos^2\alpha_- - 1 & 0 & 0 \\ \cos^2\alpha_- - 1 & \cos^2\alpha_- + 1 & 0 & 0 \\ 0 & 0 & 2\cos\alpha_- & 0 \\ 0 & 0 & 0 & 2\cos\alpha_- \end{pmatrix} \tag{3.78}$$

3.3 Atmospheric Scattering

Atmospheric scattering is a complex process and beyond the scope of this effort. However, it is important to realize that atmospheric scattering leads to partial polarization of the incident illumination. In particular, scattered skylight has varying degrees of polarization based on sun position and sensor view angles. The Air Force Research Lab (AFRL) is working on upgrading their atmospheric modeling software, MODTRAN, to include polarization effects. Therefore, it is not necessary or desirable to duplicate their efforts.

While the prediction of polarization caused by atmospheric scattering is beyond the scope of this effort, it is still necessary to be able to account for such polarization effects. Therefore, it will be necessary to estimate the polarization effects caused by atmospheric scattering. The Coulson tables provide one source of information for estimating the polarization of sky radiances. A developmental version of the polarized MODTRAN program was made available for integration testing with DIRSIG. These

two sources provided reasonable estimates of typical polarization characteristics of the sky dome radiances. Exact duplication of any given atmospheric condition was not the goal of this research. Instead I chose to demonstrate plausible effects of sky dome induced polarization using the alpha test version of the polarized MODTRAN model.

3.3.1 Coulson Tables

The Coulson tables (Coulson et al. 1960) provide tabulated estimates of the skylight polarization. Coulson used Chandrasekhar's solution for Rayleigh scattering from a plane-parallel atmosphere to calculate the polarization characteristics of downwelled and upwelled radiation. The tables published include the S_0 through S_2 parameters as well as the degree of polarization and the orientation of the plane of polarization. The latter two quantities can be calculated from the first three quantities. The values are tabulated as a function of optical thickness (τ), sun and sensor zenith distances (μ_0 and μ), surface albedo (A), and relative azimuth angle (ϕ).

The Coulson data was used to verify the plausibility of the polarimetric data obtained from the alpha test version of the polarized MODTRAN model. This also provided a sanity check on the integration of the polarized MODTRAN data into DIRSIG.

Chapter 4

Modeling an Imaging System

> Prediction is difficult, especially the future.
>
> Niels Bohr

This chapter discuses the science of modeling an imaging system as it pertains to remote sensing. A brief overview of remote sensing is presented. Next, the concept of synthetic image generation (SIG) is presented followed by a discussion of the Digital Imaging and Remote Sensing Image Generation (DIRSIG) model.

4.1 Remote Sensing

> **Definition.** *Remote Sensing* is the field of study associated with extracting information about an object without coming into physical contact with it (Schott 1997).

For the purposes of this research, remote sensing will be limited to earth observation from overhead. Furthermore, we are only concerned with passive observations in

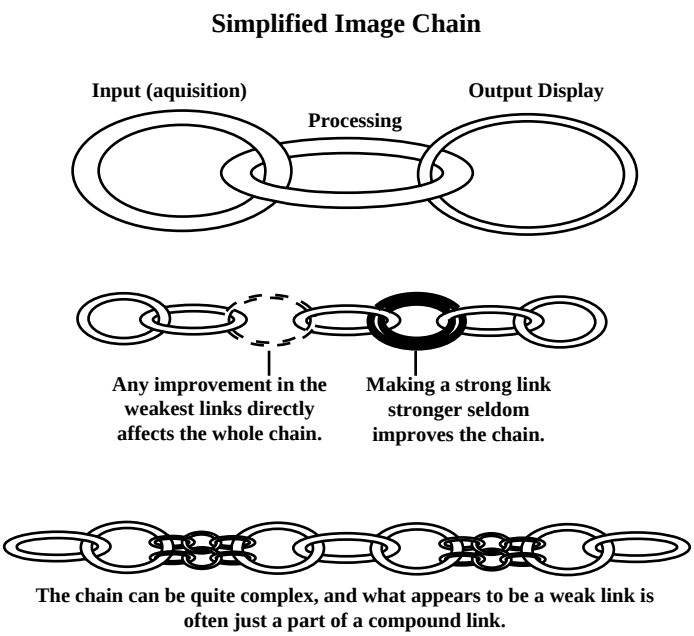

Figure 4.1: Illustration of the image chain analogy. Figure courtesy of Schott (1997, pg. 15).

the 0.4 to 1.0 μm range. Obviously, we are interested in sensors which are sensitive to the polarization state of the observed radiance.

4.1.1 Imaging Chain

Schott (1997) presents the concept of an imaging chain to describe an imaging system from start to finish. This approach allows us to consider the remote sensing process as a chain of events. The input is typically a scene of interest to the user and the output is some kind of image. In between are the various elements of the remote sensing system or links along the imaging chain. These links may include the collection system, image processing and enhancement, and finally, image production. The final image may be a display on a computer screen or a hard copy image from a printer. Each link can be subdivided into additional mini-links. Schott indicates

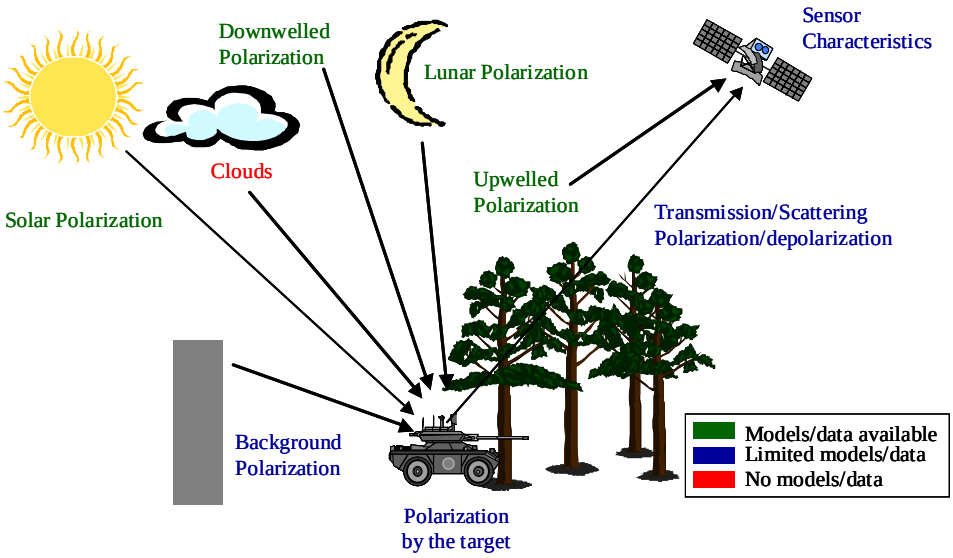

Figure 4.2: Sources of polarization in the imaging change.

that improvements to the weakest link often directly impacts the whole system while changes to stronger links rarely improve the overall system.

4.1.2 Polarimetric Remote Sensing

In this research, the image chain approach was used to analyze and model the various aspects of polarimetric remote sensing. For the purposes of this research, the imaging chain can be thought of as having the following links (see figure 4.2):

Extraterrestrial Illumination The primary source of illumination will be the sun. Other sources may include moon light, star light and manmade sources.

Downwelled Sky Radiance This will primarily be scattered extraterrestrial radiance and is the primary source of polarization in the illumination field.

Target This is the focus of the imaging operation. The primary concern will be

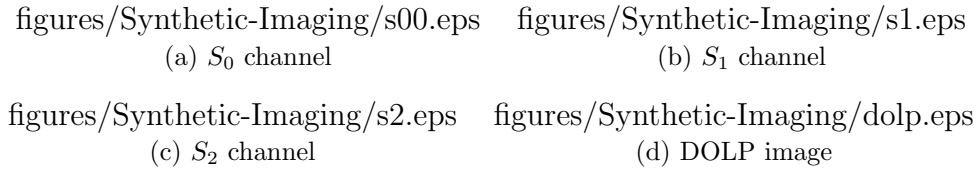

figures/Synthetic-Imaging/s00.eps figures/Synthetic-Imaging/s1.eps

(a) S_0 channel (b) S_1 channel

figures/Synthetic-Imaging/s2.eps figures/Synthetic-Imaging/dolp.eps

(c) S_2 channel (d) DOLP image

Figure 4.3: Sample broadband polarimetric images. The system only collected S_0 through S_2. The degree of linear polarization (DOLP) image was created from the other three images. Images courtesy of the Air Force Research Lab, Kirtland AFB.

determining the polarimetric BRDF of the target.

Background This includes anything that interacts with the illumination field and the target. For example, this may be buildings, the ground, trees, etc. The difference between targets and background is mostly semantics.

Upwelled Sky Radiance Again, this will primarily be scattered extraterrestrial radiance.

Sensor This is the system that images the scene and produces an output image. The sensor system will almost always have polarization biases which must be modeled.

Each of these links will be modeled individually. The complete system will then be simulated by combining the individual pieces. This simplifies the modeling process and allows for a modular upgrading process. Additionally, it simplifies the process of evaluating the relative importance of each step along the imaging chain.

Broadband polarimetric imaging (PI) produces four images for each scene. These images can be considered as separate channels. The first image is identical to the unpolarized intensity image normally produced by a typical broadband imaging system. The other three images correspond to intensity images that have been passed

through one of three polarized filters. The first two filters are linear with one aligned vertically or horizontally and the other aligned at a 45° angle. The third filter is either right-hand or left-hand circular. The same applies for each band in spectral images.

These images can be analyzed as is or they can be combined to produce additional polarization image products. It is common to produce a set of images showing the degree of polarization. This can be done for all possible polarization states (i.e. degree of polarization) or for a subset of the polarization states (i.e. degree of linear polarization or degree of circular polarization). Figure 4.3 shows some sample broadband polarimetric images.

4.2 Synthetic Imagery

Advances in computer technology provide the capability to generate synthetic images of complex scenes (Schott et al. 1997). Synthetic image generation (SIG) models attempt to reproduce what a real sensor would collect under a given set of conditions (Schott et al. 1999). The ideal modeling method uses a first principles physics based approach. Using this approach, the model is applicable to the largest possible set of conditions. This type of approach also simplifies the modeling of complex interactions (i.e. shadowing effects) because the model is attempting to simulate the actual physical processes involved.

High fidelity synthetic imagery can be used in a number of applications ranging from sensor design studies to algorithm development and testing to analyst training. One of the major benefits of using synthetic imagery is the inherent truth data sets. It is extremely difficult to collect a large truth data set for real remotely sensed imagery. However, since the synthetic imagery came from a scene model, truth data is available

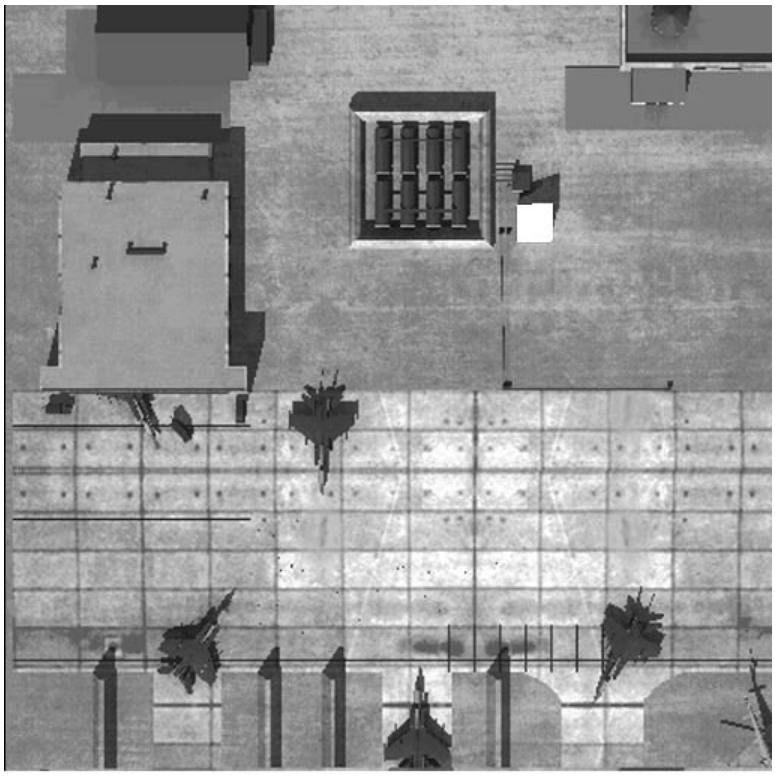

Figure 4.4: Sample DIRSIG image courtesy of Schott (1997, pg. 381).

for every pixel in the scene.

Another big advantage of using synthetic imagery is the cost savings. Synthetic images can be relatively easily generated for a range of variables. This also provides the capability to strictly control all of the variables to better determine the impacts of each one. This is something which is extremely difficult and costly to do, if at all possible, with a real remote sensing system.

Schott et al. (1999) indicate that the need for diverse sets of imagery for training automatic target recognition algorithms (ATRs) has been a major driver of SIG development. Consequently, the early SIG development tended to focus on broad band thermal infrared image simulation. As more advanced remote sensing systems started

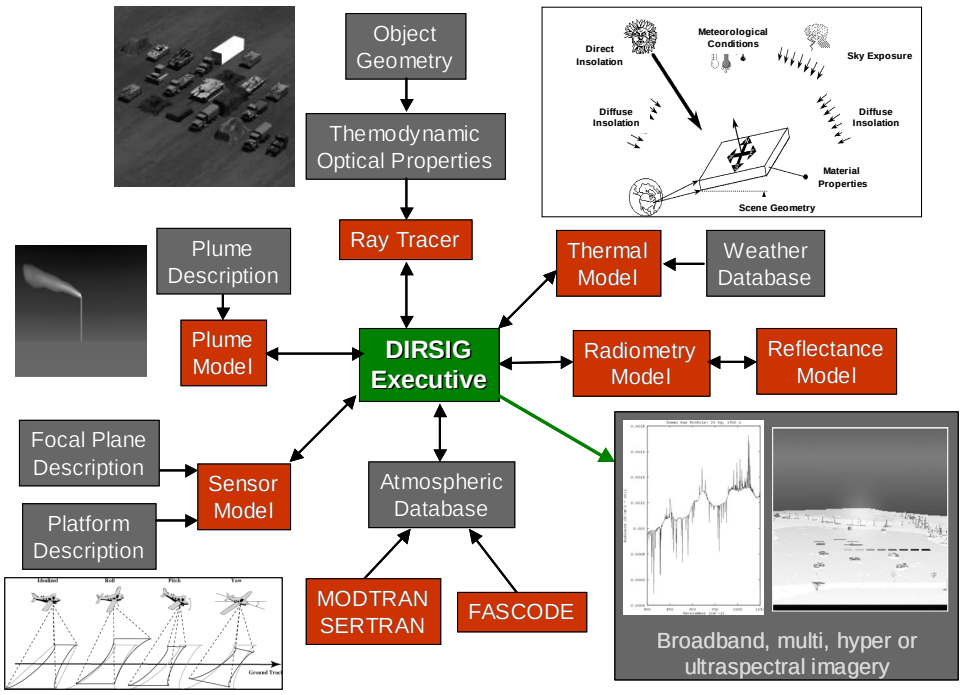

Figure 4.5: Diagram of DIRSIG submodel integration. (Figure curtesy of Brown)

to become available and advances in computer technology enabled more complex modeling, SIG models have widened their applicability to hyperspectral applications in the 0.3 μm to 20 μm range (Brown et al. 1996).

4.3 DIRSIG

Over the past twenty years, the Carlson Center for Imaging Science at RIT has been developing a high fidelity SIG model called DIRSIG. The DIRSIG model consists of a variety of independent submodels which have been integrated. Figure 4.5 shows a diagram of the current DIRSIG conglomeration of models. The modular design simplifies the debugging and enhancement processes. The modular design also provides

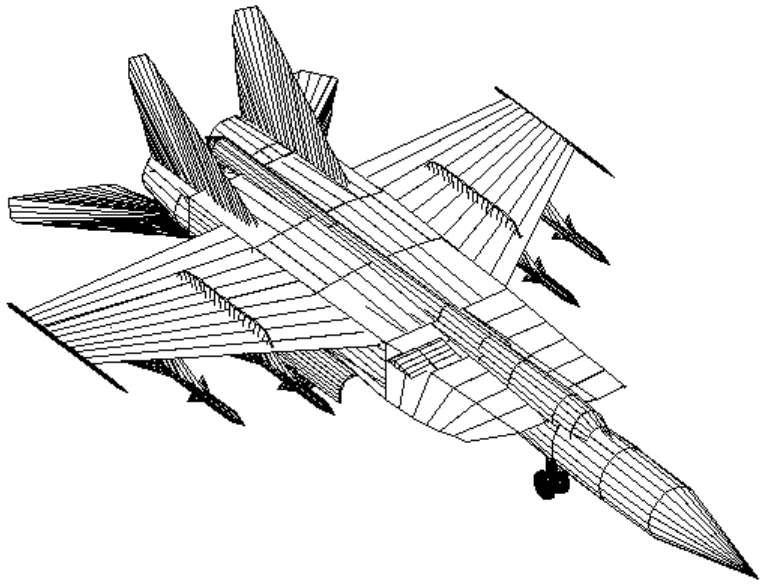

Figure 4.6: A sample facet geometry model used by DIRSIG. The model was built using a CAD software package. Specific material types can be assigned to each facet. Figure courtesy of Schott (1997, pg. 374).

a great amount of flexibility by enabling a simple substitution of various submodels.

The information in sections 4.3.1 through 4.3.5 comes from the DIRSIG website (`http://www.cis.rit.edu/~dirsig`) and the DIRSIG User's Manual (Brown 2001).

4.3.1 Scene Geometry

The scene geometry is modeled using flat facet models. Objects in the scene can be built using CAD software. A collection of object files can then be combined to create the complex scene to be imaged. Thermodynamic and optical properties are assigned to each individual facet in the scene. Sub-facet level characteristics can be applied using various mapping files. For example, spectral texturing is applied

through the use of texture maps. A single facet can be assigned multiple material types by using a material map.

4.3.2 Ray Tracing

DIRSIG uses a ray tracing algorithm to determine which facets contribute radiance to each pixel in a synthetic image. The ray tracer accounts for opaque and transmissive facets. It also accounts for limited multibounce to account for interactions between facets within a scene. The unpolarized version of DIRSIG (3.4) uses a "two and one-half" bounce approach. The ray tracer shoots a ray from the sensor and finds the first opaque facet. At this point, the hemisphere above the facet is sampled to determine the sky radiance contribution. Next a new ray is shot in the specular direction to determine if a background facet contributes to the reflected radiance from the first opaque facet. If a background facet is located, the sky radiance from its specular direction is sampled and added to the reflected radiance from the first facet. In addition to the specular direction, rays are also shot towards all sources from both facets (see figure 4.7). Transmission losses are taken into account when tracing all of the rays.

4.3.3 Thermal Model

Facet temperatures are obtained using a differential model called THERM. The model accounts for material properties, meteorological histories, and the solar shadow history. The THERM model can be overridden at the facet level if a better temperature prediction method is available (i.e. an offline engine model). The temperature predictions are used to determine the self-emitted radiance from the targets and background. Because the model inputs tend to vary on a pixel-by-pixel basis, a high level

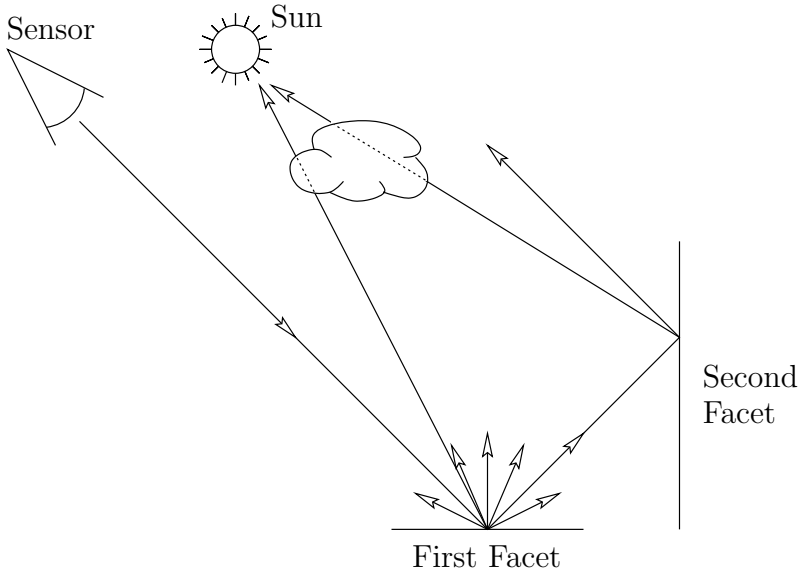

Figure 4.7: Graphical representation of DIRSIG's two and one-half bounce ray tracing algorithm.

of temperature fidelity is obtained from this model.

4.3.4 Radiometry Model

DIRSIG uses the Air Force's MODTRAN radiation propagation code to obtain exoatmospheric irradiances, emitted and scattered upwelled and downwelled radiances, and optical path transmissions. The radiometry model uses the paths obtained by the ray tracer to determine the sensor reaching spectral radiances. The spectral resolution of the radiometry model is only limited by MODTRAN. The radiometry model can also use the FASCODE model for ultrahigh spectral resolution simulations.

4.3.5 Sensor Model

The sensor model is responsible for determining which ray will be used for each pixel in the synthetic image. The sensor model accounts for the type of imaging sys-

tem (i.e. framing array, line scanner, pushbroom, etc.), flight profile, and the spectral characteristics of the sensor. The sensor model convolves the output of the radiometry model with the sensor response function to obtain the integrated radiances for each of the sensor's bands.

4.4 Summary

Using the imaging chain analysis approach, we are able to identify the weakest links in the synthetic imaging models. By addressing the weakest links, we get the greatest amount of improvement in the models for a given amount of effort. This research specifically addresses DIRSIG's inability to model polarized light. The imaging chain analysis approach was also used to identify the specific focus areas most critical to modeling polarimetric imaging. For example, since AFRL was already addressing the issue of polarized atmospheric modeling, this effort focused minimal work on modeling the atmosphere. Instead more work was focused on the issue of ray tracing and BRDF modeling since these areas were the weakest links in polarimetric modeling. Not all of the issues were resolved and the recommendations for future work reflect the current status of areas needing further research. These areas represent the weakest links as they now exist in the polarimetric modeling process.

Chapter 5

BRDF Models

If the facts don't fit the theory, change the facts.

Albert Einstein

This chapter discusses the pros and cons of various BRDF models found in the literature. The discussion begins with the unpolarized BRDF model used in previous versions of DIRSIG. This is followed by a discussion of various BRDF models which were candidates for upgrading the previously used model. Each of the models has it strengths and weaknesses. No one model is capable of predicting useful BRDFs for all types of materials. Therefore, multiple models will have to be incorporated into DIRSIG to enable modeling a wide range of scenarios.

BRDF models can be loosely divided into two classes: analytical and empirical. Based on DIRSIG's first-principles modeling approach, the preference is for analytically based models. However, it will be shown that this would severely limit the number and types of materials that DIRSIG could model. Typically, most models are not purely analytical or empirical; but some form of hybrid. For example, the Torrance-Sparrow model (section 5.2.1) is primarily analytical; however, it uses empirical methods to

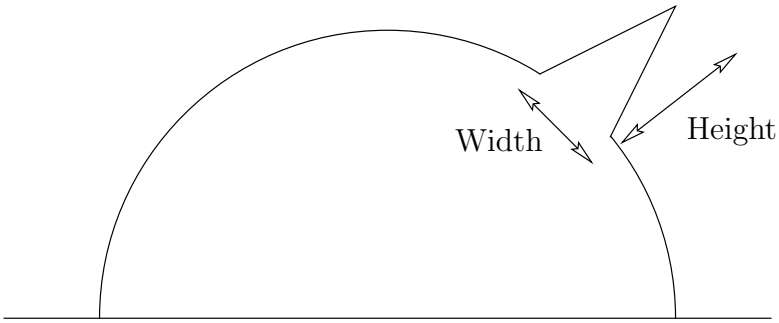

Figure 5.1: Unpolarized BRDF model used by earlier versions of DIRSIG. The specular lobe is defined using the *height* and *width* parameters. Figure redrawn from Brown et al. (1997).

determine the ratio of diffuse and specular reflections.

5.1 Current Unpolarized DIRSIG BRDF Model

The current unpolarized BRDF model used by DIRSIG uses a simplified specular and diffuse component model (Brown et al. 1997). DIRSIG uses a parameterized BRDF function to eliminate the requirement to store large BRDF data files. The parameters are wavelength dependent which allows the shape of the BRDF to vary spectrally. The BRDF is calculated by combining a diffuse component and a specular lobe (see figure 5.1).

The shape of the specular lobe is controlled by specifying one of three different functional forms: cone (or triangle), cosine, or exponential. The height and width are controlled by parameters appropriate to the functional shape. The combination of parameters allows the user to specify many different BRDF functions without having to store tabulated BRDF data files. This model greatly reduces the required storage space and provides limited insight into the physical nature of the material BRDF.

While the current model allows for a wide range of BRDF functions, it has some

important deficiencies. First, the model is totally empirical because the parameters are obtained from measured BRDF data instead of being calculated from first principles. Second, the model is limited to an ideal diffuse component and a specular lobe. This combination cannot be used to model variations in the diffuse portion of the BRDF. The Torrance-Sparrow model (section 5.2.1) addresses both of these issues. Finally, the current implementation of the model does not provide for a way to specify a polarimetric BRDF.

5.2 Analytical Models

Analytical or first-principles based models attempt to accurately model the various physical interactions involved in scattering light. These models use basic laws of physics like Snell's Law and the Fresnel reflectance coefficients to model the scattering phenomena. Due to complexities involved in light scattering, analytical models are often limited to a narrow range of problems. This requires either a large library of analytical models or the use of simplifying assumptions which increase the range of applicability at the cost of decreased accuracy.

The following models are primarily analytical in nature. While some of the models, like Torrance-Sparrow, include some empirical methods, the equations used are typically based on first-principles.

5.2.1 Torrance-Sparrow

It is common to model rough surfaces as diffuse reflectors with little or no specular component. Experimental measurements of the BRDF of roughened metallic and nonmetallic surfaces exhibit an off-specular peak (Torrance and Sparrow 1967). Tor-

rance and Sparrow indicate off-specular peaks appear when the RMS of the surface roughness (σ_m) satisfies

$$\frac{\sigma_m}{\lambda} \gtrsim 1.0 \tag{5.1}$$

where λ is the wavelength of the incident radiation. The magnitude of the off-specular peak increases with increasing incident zenith angles. The experimental data presented by Torrance and Sparrow indicate the off-specular peak becomes significant around an incident zenith angle of 45°.

Torrance and Sparrow developed an unpolarized theoretical model which predicts and describes the nature of the off-specular peak. Their model assumes the surface can be described by a Gaussian distribution of miniature facets. Geometrical optics is used to predict the scattered radiance. The reflection from each facet is modelled with a specular and a diffuse component. The model uses a geometrical attenuation factor to account for shadowing effects caused by neighboring facets. Torrance and Sparrow begin by expressing the reflected radiance as

$$dL_r = dL_{r,s} + dL_{r,d} \tag{5.2}$$

where $L_{r,s}$ and $L_{r,d}$ are the specularly and diffusely reflected radiances. The diffuse component is given by

$$dL_{r,d} = aL_i \cos\theta_i \tag{5.3}$$

where a is a constant and is one of the parameters in the model, L_i is the incident radiance, and θ_i is the angle of incidence. The specular component is given by

$$dL_{r,s} = \left(\frac{A_f L_i d\omega_i}{4}\right)\left(\frac{G}{\cos\theta_r}\right)(F)P(\alpha) \tag{5.4}$$

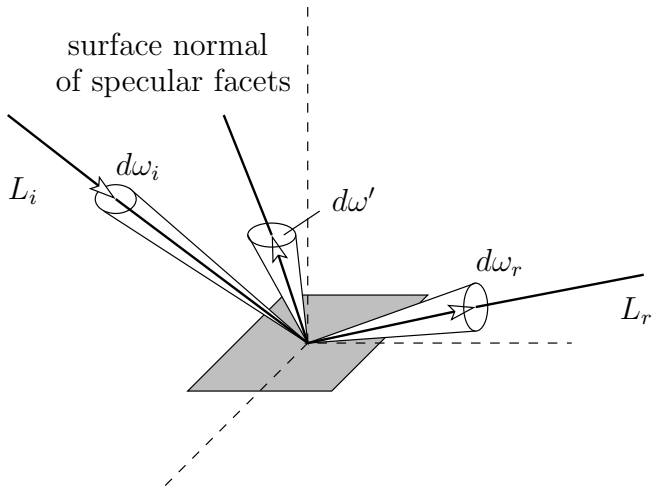

Figure 5.2: Torrance-Sparrow BRDF model geometry.

where

A_f = area of one facet $[m^{-2}]$ $\quad$ θ_r = reflected zenith angle

L_i = incident radiance $\left[\frac{W}{m^2 \cdot sr}\right]$ $\quad$ F = Fresnel reflectance

G = Geometrical attenuation factor that accounts for shadowing $\quad$ $d\omega_i$ = incident solid angle $[sr]$

$P(\alpha)$ = probability distribution of facets normals within $d\omega'$ $\quad \left[\frac{1}{m^2 \cdot sr^1}\right]$

The solid angle $d\omega'$ is a differential solid angle centered on the ray in the plane containing the incident and reflected rays and half way between the two rays (see figure 5.2). In other words, the facets with normals within $d\omega'$ are those which produce specular reflections in the reflected direction.

Torrance and Sparrow (1967) give the following equation for the BRDF

$$f = \frac{dL_r}{L_i \cos(\theta_i) d\omega_i} \tag{5.5}$$

Combining equations (5.2) through (5.6) results in the following expression for the

BRDF based on the Torrance-Sparrow model

$$f = \frac{F\, A_f\, G\, P(\alpha)}{4 \cos\theta_i \cos\theta_r} + \frac{a}{d\omega_i} \tag{5.6}$$

The first term of (5.6) is the specular component and the second term is the diffuse component.

The diffuse component is assumed to be perfectly Lambertian and therefore completely depolarizing. However, the specular contribution can introduce polarization effects through the Fresnel reflectance factor, F. Circular polarization can also be introduced through the Fresnel reflectance factor if the material's index of refraction is complex.

Priest and Germer (2002) polarized the Torrance and Sparrow model by combining it with the Mueller matrix for a microfacet surface. The equation for the polarimetric BRDF is given in Priest and Germer as

$$f_{j,k}(\theta_i, \theta_r, \phi_r - \phi_i) = \frac{1}{2\pi} \frac{1}{4\sigma^2} \frac{1}{\cos^4(\theta)} \frac{\exp(-\frac{\tan^2(\theta)}{2\sigma^2})}{\cos(\theta_r)\cos(\theta_i)} M_{j,k}(\theta_i, \theta_r, \phi_r - \phi_i) \tag{5.7}$$

where j and k are the indices of the Mueller matrix, θ (with no subscript) is the angle of incidence and reflection for the specular microfacets generating the return for the given geometry, θ_i and θ_r are the zenith angles, ϕ_i and ϕ_r are the azimuth angles, σ is the surface roughness parameter, and M is the microfacet Mueller matrix. The subscripts i and r refer to the incident and reflected directions respectively in the macro facet reference frame.

The Priest and Germer modification only includes the specular component of the Torrance and Sparrow BRDF. Wellems et al. (2000) proposed estimating a diffuse, depolarizing term by integrating the BRDF over the entire hemisphere for a perfectly reflecting microfacet surface with a given surface roughness. The difference between the integrated value and 1.0 can be attributed to diffuse scattering resulting from

multiple bounces and subsurface interactions. This depolarizing term is a function of only the surface roughness and not the material's complex index of refraction. This depolarizing term is included as an optional term in the DIRSIG implementation of the Torrance and Sparrow BRDF model.

Earlier geometrical optics based models predicted an infinite reflectance when the scattering angle equals 90°. The Torrance-Sparrow model over comes this major deficiency through an appropriate shadowing function and accurately predicts a finite reflectance for all scattering angles.

Torrance and Sparrow successfully modeled the off-specular peaks they observed in their measured data using this model. They concluded the off-specular peaks are caused by an interaction between the Fresnel reflection for each facet and the increased shadowing as the incident angle approaches near-grazing. Their experimental and theoretical results both agree that the diffuse reflector approximation is only valid for near normal incident angles. This model provides a simple method for predicting the off-specular peaks based on the surface roughness and incident and scattering angles.

Currently, the modified Torrance and Sparrow model is the only polarized BRDF model which was successfully integrated into the polarized version of DIRSIG.

5.2.2 Glossy Coatings

Many BRDF models, like Beard-Maxwell (section 5.3.2) and Torrance-Sparrow (section 5.2.1), assume volume scattering is completely randomly polarized due to multiple scattering. These models assume the polarized reflectance is solely due to the first surface reflections. However, Ellis (1996) derived an analytic expression for glossy coatings which indicates the volume scattering can be partially polarized. Furthermore, Ellis discovered that the first surface reflections and volume scattering are

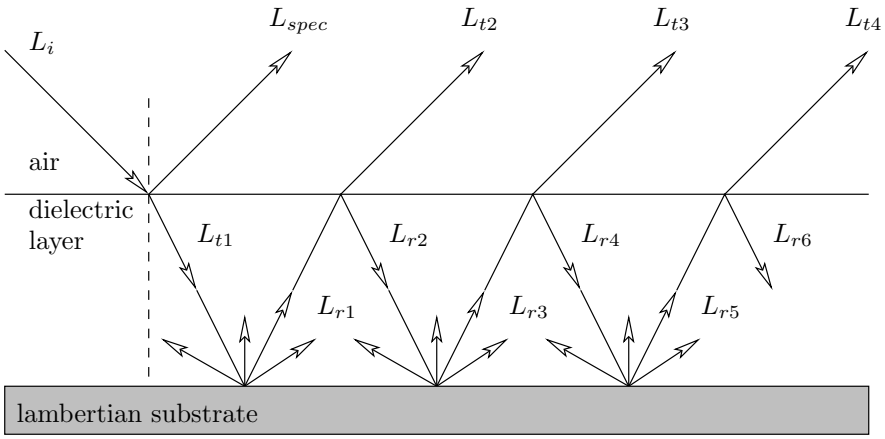

Figure 5.3: Reflection and transmission geometry for the Ellis glossy coatings model. (figure redrawn from Ellis (1996, fig 1, pg 1759))

not decoupled as is commonly assumed in simpler models. This coupling is responsible for polarizing the volume scattering.

Ellis' model assumes a specular, nonabsorbing dielectric layer which covers a perfectly Lambertian substrate. Many analytic models empirically determine the ratio of specular and diffuse reflectance. However, this model uses only two physical parameters to predict the ratio: the index of refraction of the coating and the diffuse reflectance of the substrate. Figure 5.3 shows how the first surface and volume scattering terms are coupled. The Fresnel reflection coefficients predict the polarization state of the specular scattering term, L_{spec}. Since the substrate is assumed to be perfectly Lambertian, the radiance reflected from the substrate (i.e. L_{r1}, L_{r3}, L_{r5}, ...) will be completely randomly polarized. However, the radiance transmitted back through the dielectric-air interface (i.e. L_{t2}, L_{t3}, L_{t4}, ...) will be partially polarized as predicted by the Fresnel transmission coefficients. The summation of these radiances results in the diffuse component of the reflection.

Ellis' glossy coating BRDF model was derived only for a single smooth layer. He

indicates that the model can be expanded to include rough surfaces as well. Because the model was derived from basic principles, the functions are non-negative and they automatically account for reciprocity and conservation of energy.

This is a potentially very useful model since it requires only two optical parameters and does not rely on empirical data in any way. The usefulness of this model can be increased by incorporating some of the strengths of the Torrance-Sparrow model which account for rough surfaces. While this model would be very useful for various types of painted and coated surfaces, it was not chosen for integration into the current version of DIRSIG. A lack of continuing support and database of material parameters were the main factors for not implementing this model. In the future when additional material properties are more readily available, this type of model may be a good candidate for expansion of the library of polarized BRDF models.

5.2.3 F-BEAM

The Environmental Research Institute of Michigan (ERIM) developed a first-principles based paint reflectance model (F-BEAM) which predicts the polarimetric BRDF of a multi-layer coating (Ellis et al. 1995). In certain areas, F-BEAM can handle more complex problems than Ellis' glossy coatings model; but in other areas it makes simplifying assumptions which Ellis discovered aren't always valid. For example, F-BEAM can handle multiple paint layers and predicts pigment scattering using Mie theory. However, F-BEAM makes the assumption that the volume scattering is completely randomly polarized. F-BEAM models rough surfaces using randomly oriented facets. It appears that F-BEAM is a successor of the Coatings Engineering Evaluation Program (CREEP) described by Ellis (1994) in a web based tutorial on modeling BRDFs.

Unlike the Torrance-Sparrow model, F-BEAM does not account for facet shadowing at large incident elevation angles. Also, the model only handles single scattering at the surface. Therefore, it tends to deviate from measured data at large angles. Future improvements to F-BEAM were planned (Ellis et al. 1995) to account for some of these limitations. However, no additional information is available since the code was presented at the Sixth Target Modeling and Validation Conference. When asked about the availability of F-BEAM, Veridian, which acquired ERIM, indicated that the code had been sold to Surface Optics.

Since F-BEAM requires detailed recipe information for each paint layer, it is not suitable for integration into DIRSIG as a part of this effort. However, it may be useful to individual DIRSIG users for computing specific BRDF files for specialized cases where the details are fully known. These BRDF files could then be used in a look-up table fashion or parameterized using an empirically based model. These BRDF files could then be integrated into a DIRSIG simulation.

5.3 Empirical Models

Empirical models are primarily based on fitting a function or group of functions to measured BRDF data. The parameters obtained can then be used to calculate an estimate of the BRDF "on-the-fly". This approach greatly reduces the amount of computer storage space required to maintain a library of BRDFs. Empirical models can often be used to characterize complex scattering phenomena which are difficult or impossible to model. Unfortunately it is often not possible to extrapolate empirical models for cases where measured data are unavailable.

The following models are primarily empirical in nature. Therefore, they heavily rely on measured BRDFs to determine the required parameters. In some cases, the

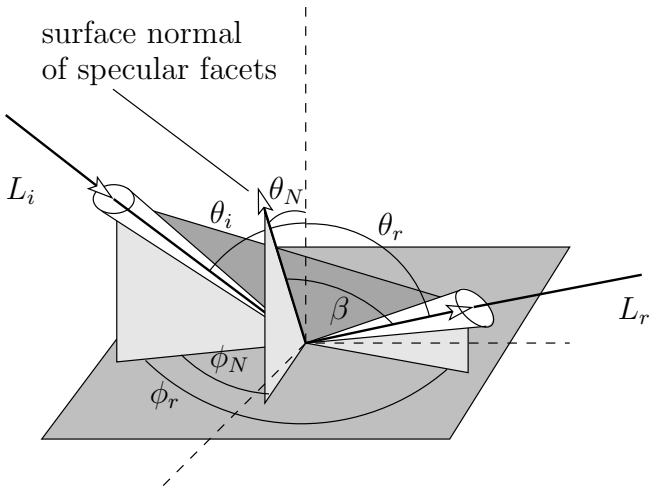

Figure 5.4: Beard-Maxwell BRDF model geometry. (Figure redrawn from Maxwell et al. (1973, fig 1, pg 4))

parameters may have a physical relevance. In other cases, the parameters are simply the weights of the basis functions used to model the BRDF. In all cases, the models attempt to approximate the complex nature of the measured BRDF with as few parameters as possible.

5.3.1 Robertson-Sandford

The Robertson-Sandford model uses four parameters to model the specular reflection from the first surface as well as the diffuse components. This model is intended for IR calculations and does not account for polarization effects (Ellis 1994). Therefore, this model is not useful for this effort.

5.3.2 Beard-Maxwell

The Beard-Maxwell model (Maxwell et al. 1973) uses six parameters to model the BRDF of a variety of materials. The model uses the Fresnel equations to predict

the first surface specular reflection from randomly distributed facets. The diffuse scattering is predicted using a combination of a pure Lambertian term and an isotropic Hapke/Lommel-Seeliger model. The Hapke/Lommel-Seeliger model is a modification of the simple Lambertian model which accounts for decreased reflectance at large angles. It was originally developed for predicting the lunar BRDF. Note that in this section only, I have chosen to use the nomenclature used by Beard and Maxwell (1973). Specifically, Beard and Maxwell us the symbol ρ' to denote the BRDF. In the Beard-Maxwell model, the BRDF is given by

$$\rho' = \frac{\mathrm{R}(\beta)}{\mathrm{R}(0)} \frac{\rho_{_{fs}} \cos^2 \theta_N}{\cos\theta_r \cos\theta_i} \left[\frac{1+\theta_N}{1+\frac{\theta_N}{\Omega}\, e^{\frac{-2\beta}{\tau}}} \right] + \rho_{_d} + \frac{2\,\rho_v}{\cos\theta_r + \cos\theta_i} \tag{5.8}$$

where R is the Fresnel reflectance function, $\rho_{_{fs}}$ is the first surface BRDF, Ω and τ are shadowing and obscuration function parameters, $\rho_{_d}$ is the diffuse component, and ρ_v is the volumetric component (Maxwell et al. 1973; Ellis 1994). The various geometry related variables are illustrated in figure 5.4. The Fresnel reflectance function requires the complex index of refraction as a function of wavelength. $\rho_{_{fs}}$ is obtained from a zero bi-static BRDF scan of the surface. In reality, it is a near zero bi-static scan since it is not possible to exactly collocate the transmitter and receiver. Maxwell et al. (1973) simply state, without specifying units, that values of $\tau = 15$ and $\Omega = 40$ were used in their study. In general, the values for τ and Ω can be obtained from fitting the following equation to the measured zero bi-static BRDF scan:

$$\rho'\left(\theta_{\hat{n}}, \phi_{\hat{n}}; \theta_{\hat{n}}, \phi_{\hat{n}}\right) = \frac{\mathrm{R}(0)}{\mathrm{R}(\beta)} \frac{\rho'\left(\theta_i, \phi_i; \theta_r, \phi_r\right) \cos\theta_i \cos\theta_r}{\left(\cos^2\theta_{\hat{n}}\right) \mathrm{SO}(\beta, \tau, \Omega, \theta_{\hat{n}}, \theta_i)} \tag{5.9}$$

where SO is the empirical shadowing and obscuration function and R is the Fresnel reflectance function. Maxwell defines SO as:

$$\mathrm{SO}(\beta, \tau, \Omega, \theta_{\hat{n}}, \theta_i) = \frac{1+\frac{\theta_{\hat{n}}}{\Omega}\, e^{\frac{-2\beta}{\tau}}}{1+\frac{\theta_{\hat{n}}}{\Omega}} \left(\frac{1}{1+\frac{\theta_{\hat{n}}}{\Omega}\frac{\theta_i}{\Omega}} \right) \tag{5.10}$$

An analysis of the Beard-Maxwell implementation used by the NEF data system (see section 5.4) indicates the parameters τ and Ω have the same angular units used for θ and β.

One known limitation of the Beard-Maxwell model is the assumption that the first surface scattering does not depolarize while the volume and diffuse scattering completely depolarizes. This assumption is required for determining some of the model parameters. Ellis has shown this assumption to be invalid for glossy coatings but did not address the validity of the assumption for roughened surfaces (Ellis 1996). Maxwell et al. recognized the need for modeling partially polarized volume scattering. Therefore, they included two additional factors in the last term of equation (5.8) to result in the most general form of the model

$$\rho' = \frac{\mathrm{R}(\beta)}{\mathrm{R}(0)} \frac{\rho_{_{fs}} \cos^2\theta_N}{\cos\theta_r \cos\theta_i} \left[\frac{1+\theta_N}{1+\frac{\theta_N}{\Omega}\, e^{\frac{-2\beta}{\tau}}} \right] + \rho_{_d} + \frac{2\,\rho_v f(\beta) g(\theta_{\hat{n}})}{\cos\theta_r + \cos\theta_i} \tag{5.11}$$

$f(\beta)$ and $g(\theta_{\hat{n}})$ are arbitrary functions which can be used to empirically model variations in the volume scattering. Maxwell et al. set $f(\beta) = g(\theta_{\hat{n}}) = 1$.

Like the Torrance-Sparrow model, the Beard-Maxwell model can be modified to produce polarized BRDFs by using the Fresnel reflectance function to predict the polarimetric reflections from the first surface reflections. The model has been used to empirically model the BRDF of a variety of materials. Therefore, it promises to be a valuable tool for modeling polarimetric reflections within DIRSIG. The major limitation will be obtaining measured parameters for a wide variety of materials. Currently, the NEF database is the best source of parameter data for the Beard-Maxwell model. NEF database details are presented in section 5.4.

5.3.3 Basis Function Decomposition

Complex continuous functions are often represented by a linear combination of appropriate basis functions. For example, time varying signals can be approximated using a Fourier series of sines and cosines. The same type of approach is applicable to describing complex BRDFs.

Rusinkiewicz (1998) describes a simple change of variable which can drastically reduce the number of coefficients required to adequately represent complex BRDFs. The transformation is based on the fact that many BRDFs are highly symmetric. It also takes advantage of Snell's law of reflection and the symmetry inherent about the half angle between the incident angle and specular lobe angle.

Obviously this type of model requires fully measured BRDFs. Therefore, it should only be used as a last resort in an effort to reduce the amount of storage space required for look-up table based BRDFs. Due to a lack of measured polarimetric BRDF data, this option could not be explored. However, it remains a good candidate if measured BRDF data becomes readily available.

5.4 NEF Database and Data System

The Nonconventional Exploitation Factors (NEF) database contains a collection of measured and computed optical, thermal, and electromagnetic properties for various materials. The NEF database comes with a set of software tools for accessing and processing the NEF data. This collection of software is called the NEFDS (NEF Data System). The NEFDS was developed to assist in the spectroradiometric exploitation of remotely sensed imagery and for input into modeling systems like DIRSIG (NEFDS User's Manual 1996). The NEF database contains about 400 materials and 40 groups

of materials. Of these 400 database entries, approximately 300 have Beard-Maxwell parameters.

While the NEFDS contains a powerful set of utilities, there are some significant limitations. First, it only calculates unpolarized BRDFs. Although the derivation of the Beard-Maxwell model is suitable for performing polarized BRDF predictions, the data collected for the NEF database is not suitable for polarimetric predictions. The parameters in the NEF database were not constrained by the physical representations of the individual parameters. For example, the values of n and k often differ significantly from the actual values. Therefore, the physically based model was implemented in an empirical manner which severely limits the ability to extrapolate to a polarized BRDF. Additional significant characteristics of the NEFDS BRDF utility are presented in the following sections.

5.4.1 Modification of the Diffuse Reflectance Terms

According to Metzler (2001), the NEFDS implements a slightly modified version of the Beard-Maxwell BRDF model. In the NEFDS implementation, ρ_v and ρ_d can be simultaneously nonzero. This was done to better fit the cross-polarized component of the near zero bistatic scan. The developers of the NEFDS consulted Beard and Maxwell on this modification and they were comfortable with this change (Metzler 2001).

5.4.2 First Surface BRDF Approximation

Another significant characteristic of the NEFDS BRDF utility involves the first surface BRDF, $\rho_{_{fs}}$, computation. The first surface BRDF was measured using a near zero bistatic scan (zbs) as described by Beard and Maxwell. However, the

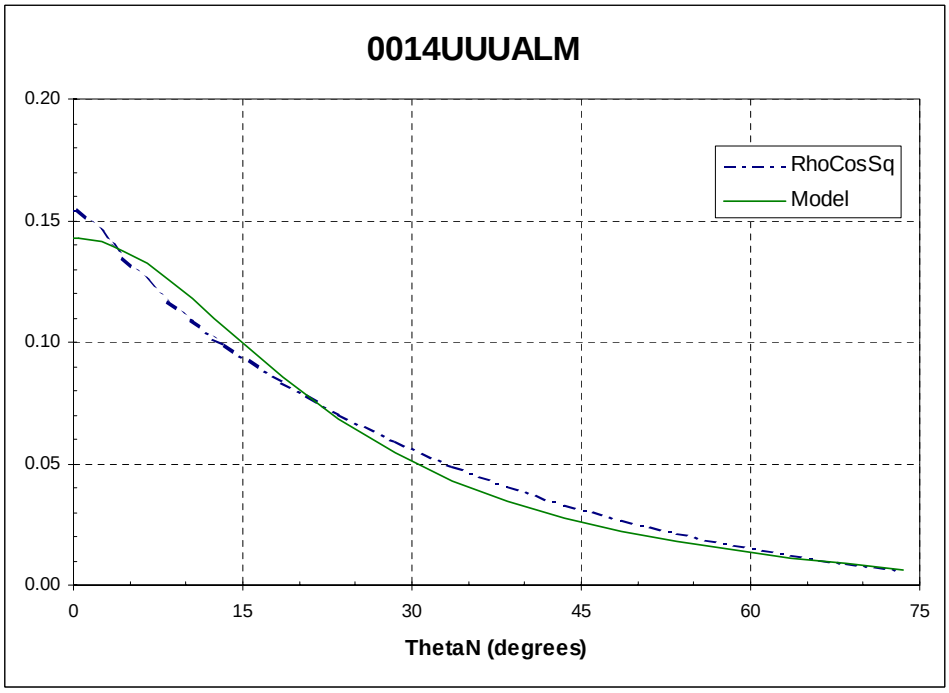

Figure 5.5: Comparison between Beard-Maxwell scanned first surface data and the fitted model. This example is for the roughened aluminium sample #0014UUUALM at $\lambda = 0.647\mu m$. The most significant differences occur where $\theta_N < 20°$.

error propagation tools in the NEFDS required a small perturbation approximation. Therefore the developers of the NEFDS decided to fit the zbs data to the function

$$\Xi = \frac{Bias}{\cos\theta_N \left[\sigma^2 + \tan^2\theta_N\right]} \tag{5.12}$$

where $Bias$ and σ are the fitting parameters. While this approach provides a functional form for the first surface scan data, it also introduces additional errors. These errors are greatest in the region where $\theta_N < 20°$ which correspond to reflections in the specular region (see figure 5.5). It is difficult to quantify the significance of these differences in the absence of measured polarimetric BRDF data. Metzler gives the following explanation of the small perturbation approximation used by the NEFDS:

A modified Cauchy distribution is fit to the potentially noisy first-

surface facet distribution function for several reasons. 1) An analytical form of the distribution is needed to support the error propagation calculations required by the NEF, 2) when the zbs [zero bistatic scan] data are noisy near the peak, the importance sampling portion of the Monte-Carlo hemispherical integration can get mislead by anomalous "peaks", and 3) when the zbs data are noisy, the NEF output results can be noisy with respect to elevation angle. This caused problems for some users, and using an analytical function fit to the zbs data effectively smoothed the "noise". Finally, since the modelled BRDF is effectively scaled by the DHR, differences in the calculated (hemispherically integrated) values between using the measured zbs and the fit Cauchy are quite small. This may not always be the case for the BRDF at a specific geometry (Metzler 2001).

5.4.3 Spectral Integration

Since the NEF database only contains Beard-Maxwell parameters at five wavelengths, it is necessary to spectrally interpolate the BRDF calculations between the reference wavelengths. The developers of the NEFDS decided to use the spectral directional hemispherical reflectance (DHR) data as a weighting factor for the spectral interpolation. The interpolation involves the following steps:

1. The Beard-Maxwell BRDF model (as implemented in the NEFDS) is used to estimate the DHR at each of the reference wavelengths.

2. The BRDF for the desired geometry is calculated at the reference wavelengths.

3. The BRDF at the intermediate wavelengths is calculated using

$$\rho'(\overline{\Theta},\lambda) = \rho_d(\lambda)\left[\frac{\rho'(\overline{\Theta},\lambda_{r1})}{\iint\limits_{hemisphere}\rho'(\overline{\Theta}_{DHR},\lambda_{r1})\cos(\theta_i)d\theta_i d\phi_i}A + \frac{\rho'(\overline{\Theta},\lambda_{r2})}{\iint\limits_{hemisphere}\rho'(\overline{\Theta}_{DHR},\lambda_{r2})\cos(\theta_i)d\theta_i d\phi_i}B\right] \tag{5.13}$$

where

$$A = \frac{\lambda_{r2} - \lambda}{\lambda_{r2} - \lambda_{r1}} \tag{5.14}$$

$$B = \frac{\lambda - \lambda_{r1}}{\lambda_{r2} - \lambda_{r1}} \tag{5.15}$$

and,

$\rho'(\overline{\Theta}, \lambda)$	Modeled BRDF at specified geometry and wavelength
$\rho_d(\lambda)$	Measured DHR
$\lambda_{r1}, \lambda_{r2}$	Reference wavelengths in NEF database
λ	Wavelength of interest
$\overline{\Theta}$	Geometry of interest (i.e. $\theta_i, \phi_i, \theta_r, \phi_r$)
$\overline{\Theta}_{DHR}$	Geometry of NEF DHR measurements (i.e. $\theta_i, \phi_i, \theta_{DHR}, \phi_{DHR}$)

Comparisons of the measured and modeled DHR values indicate significant differences. Part of the differences can be attributed to limitations of the model. These differences tend to increase as the material becomes more specular. Unfortunately, the errors introduced by the first surface BRDF approximation also increase these differences.

5.4.4 DHR Integration

The NEFDS code attempts to simulate the DHR measurement at the reference wavelengths by performing an integration over the entire hemisphere. The integration algorithm uses a nonuniform sampling grid which concentrates on the specular lobe region. A plot of the sampling grid for one of the database entries shows an interesting pattern and a significant difference in the sampling frequency in and out of the specular lobe region (see figure 5.6).

In addition to the peculiar sampling grid, the integration algorithm does not take advantage of symmetry. For isotropic materials, the BRDF will have azimuthal

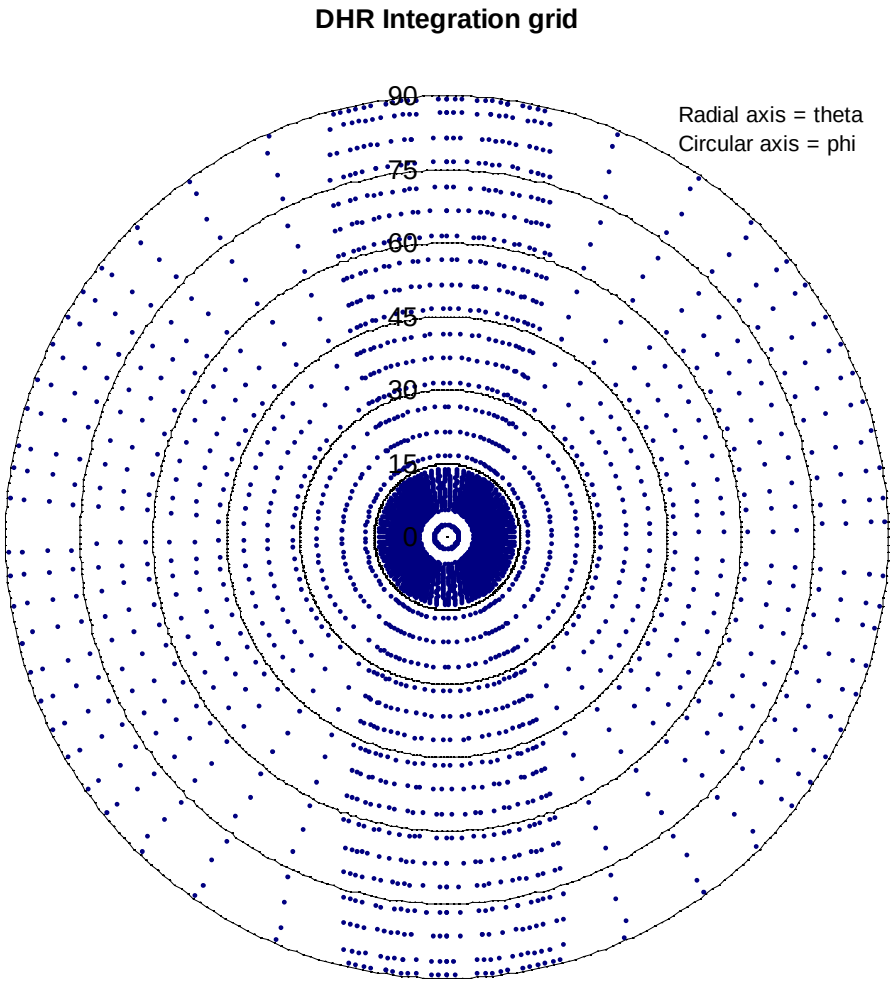

Figure 5.6: Hemispherical sampling grid used to estimate the DHR of the roughened aluminium sample (#0014UUUALM) at $\lambda = 0.647\mu m$. The specular lobe width was approximately 45°. The measured DHR was 0.40303 and the modeled DHR was 0.36880.

symmetry (i.e. $f(\theta_i, \phi_i, \theta_r, \phi_r) = f(\theta_i, \phi_i, \theta_r, -\phi_r)$). Therefore, half of the integration points can be eliminated while maintaining the same level of accuracy. When it becomes feasible to implement a NEF-like Beard-Maxwell based BRDF model within DIRSIG, better methods of performing the DHR integration should be explored.

5.4.5 Usefulness of the NEF Utilities and Database

Currently the NEF database is the only source of data available for calculating Beard-Maxwell based polarimetric BRDFs. The database contains Beard-Maxwell model parameters for up to 300 materials. The actual number of materials is significantly less than this number since there are multiple entries for the same type of material (i.e. there are multiple aluminum samples which cover different surface roughnesses and levels of oxidation).

The fact that the NEFDS BRDF utility does not calculate a polarimetric BRDF immediately eliminates it as a potential for integration into DIRSIG. The other computational characteristics discussed above also limit the potential for a direct integration. AFRL and the National Imagery and Mapping Agency (NIMA) are currently investigating options for expanding the NEF database and recomputing the Beard-Maxwell parameters in order to support polarimetric calculations. If this actually happens, then the NEF database and a Beard-Maxwell based model may become the best source of polarimetric BRDFs. Until then, other polarized BRDF models, like Torrance and Sparrow must be used.

5.5 Summary

Analytical BRDF models are the desired choice for integration with DIRSIG since they calculate the BRDF by modeling the underlying physics. Unfortunately, very few analytical BRDF models exist that also account for polarization. And the analytical models that do exist are often implemented empirically because of small amount of measured polarized BRDF data available for model validation and parameter estimation. The major disadvantage of using empirical methods is the inability to extrapolate the results beyond the domain of the data used to derive the model's parameters.

Chapter 6

Approach

Experiments should be reproducible—they should all fail in the same way.

Finagle's Rule

This chapter presents the approach and methods used to achieve the objectives of this dissertation. It discusses how the polarimetric modeling was integrated into DIRSIG and the tests used to verify the accuracy of the new capabilities.

6.1 Modifications to the Core DIRSIG Program

The implementation of polarimetric modeling within DIRSIG required significant modifications to the way DIRSIG stores and processes the data used to perform a simulation. For example, in the unpolarized version, irradiance and radiance values were stored using a single floating point value. In the polarized version up to four double precision floating point values are needed to store and process irradiances and radiances. Additional complexities resulted from the requirement to be able to perform polarized and unpolarized computations simultaneously within a single

simulation. This requirement ensures that the new polarimetric modeling tools can still be used with a limited amount of polarimetric information. The following sections discuss the modifications made to the core part of DIRSIG.

In addition to the modifications required for the polarimetric simulations, the entire DIRSIG code was rewritten as part of a simultaneous project. The new version was developed using the C++ object oriented programming language. The polarimetric capabilities were implemented using an object oriented approach and helped dictate the structure of other parts of the DIRSIG rewrite. The new code was written using the literate programming model. Therefore, the documentation and computer code coexist in a single document. The reasons for many of the design choices presented here are presented in the code documentation.

6.1.1 Mueller Calculus Additions

All polarimetric based calculations within DIRSIG require the use of Mueller calculus. Therefore, it was necessary to develop a set of C++ classes which could handle Stokes vectors and Mueller matrices. These classes take care of storing the polarized and unpolarized data (i.e. radiance values and BRDFs), converting between polarized and unpolarized representations, and all of the associated mathematical computations. The mathematical computations supported include all of the matrix operations required for Mueller calculus calculations. In addition, the classes also handle computations like degree of polarization, vector and matrix rotations, and other polarimetric related calculations. The classes were designed to support calculations using any combination of polarized and unpolarized quantities. Specifics about the capabilities and implementation of the Stokes vector and Mueller matrix classes is provided in the documentation of these classes.

6.1.2 Spectral Vector Modifications

Since DIRSIG performs all radiometric computations spectrally, an efficient method of handling spectrally varying data was developed. DIRSIG needs to be able to store various polarized and unpolarized quantities as a function of wavelength. In the case of radiances, these quantities will be Stokes vectors and in the case of BRDFs, these quantities will be Mueller matrices. While other data, like scale factors, will be simple scalar quantities.

DIRSIG needed a way of storing and processing this wide variety of spectral data. The result was the development of a C++ class template which could be used with any C++ data storage class developed for DIRSIG or any inherent C++ data class. The individual data storage classes (i.e. the Stokes vector and Mueller matrix classes) are responsible for storing the polarized data and performing all of the associated mathematical operations. The spectral vector template provides the framework for storing all of the spectral quantities associated with the polarized data and performing spectrally based computations like spectral averaging, interpolation, and extrapolation. The spectral vector template also provides the interface to access the mathematical functionality provided by the individual data storage classes. Figure 6.1 shows the relationships between the Stokes vector and Mueller matrix classes and the spectral vector classes.

A single spectral vector contains only one type of data (i.e. Stokes vectors, Mueller matrices, or scalars). However, the individual data values for each spectral vector location can be any mixture of polarized and unpolarized quantities. Therefore, if polarization data is only available for a limited set of spectral values, DIRSIG can use a combination of polarized and unpolarized values for the overall simulation. The associated Stokes vector and Mueller matrix classes automatically handle switching

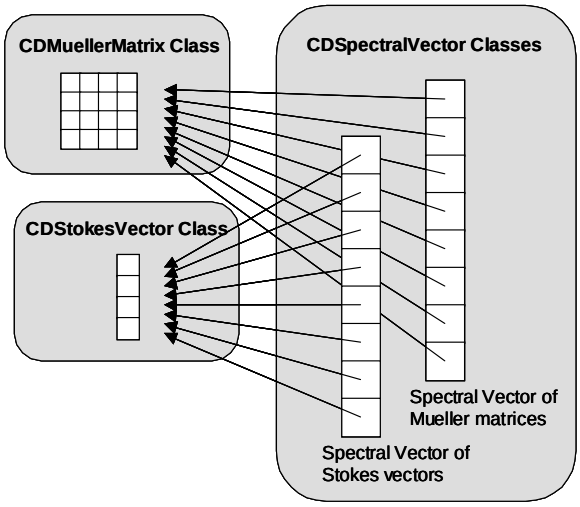

Figure 6.1: Relationship between the spectral vector classes and the data storage classes. The spectral vectors contain a list of individual Stokes vectors or Mueller matrices (or other data types) and uses those classes to perform the Mueller calculus operations at each spectral location.

between polarized and unpolarized calculations as needed. An example of this is demonstrated with this simple three band scenario.

In this example, data are available for three spectral bands, 450 nm, 550 nm, and 650 nm. However, polarization data is only available for the the radiances in the 450 nm and 550 nm bands while unpolarized data are available for the 650 nm band. The light is reflected from a surface for which the polarized BRDF is known in all three bands. The following equations demonstrate how the spectral vector class handles this scenario.

The irradiances are given as

$$\mathbf{E_{in}}(450\text{nm}) = \begin{pmatrix} 5.0 \\ 2.0 \\ -1.0 \\ 0.0 \end{pmatrix} \quad \mathbf{E_{in}}(550\text{nm}) = \begin{pmatrix} 6.0 \\ 0.0 \\ -2.5 \\ 1.0 \end{pmatrix} \quad \mathbf{E_{in}}(650\text{nm}) = 7 \qquad (6.1)$$

and are stored in a spectral vector of Stokes vectors like this

$$\text{Ein}[0] = [5.0, 2.0, -1.0, 0.0] \tag{6.2}$$

$$\text{Ein}[1] = [6.0, 0.0, -2.5, 1.0] \tag{6.3}$$

$$\text{Ein}[2] = [7.0] \tag{6.4}$$

along with information indicating the wavelength associated with each spectral vector location.

The Mueller matrices for the BRDFs are given as

$$\mathbf{f}(450\text{nm}) = \begin{pmatrix} 1.5 & 0.01 & 0 & 0 \\ 0.01 & 1.7 & 0 & 0 \\ 0 & 0 & -1.2 & 0.4 \\ 0 & 0 & -0.4 & 1.2 \end{pmatrix} \tag{6.5}$$

$$\mathbf{f}(550\text{nm}) = \begin{pmatrix} 1.6 & 0.02 & 0 & 0 \\ 0.02 & 1.75 & 0 & 0 \\ 0 & 0 & -1.15 & 0.35 \\ 0 & 0 & -0.35 & 1.15 \end{pmatrix} \tag{6.6}$$

$$\mathbf{f}(650\text{nm}) = \begin{pmatrix} 1.7 & 0.03 & 0 & 0 \\ 0.03 & 1.8 & 0 & 0 \\ 0 & 0 & -1.1 & 0.3 \\ 0 & 0 & -0.3 & 1.1 \end{pmatrix} \tag{6.7}$$

and are stored in a spectral vector of Stokes vectors like this

$$\begin{aligned}\text{brdf}[0] = [&1.5,\ 0.01,\ 0.0,\ 0.0,\ 0.01,\ 1.7,\ 0.0,\ 0.0,\\ &0.0,\ 0.0,\ -1.2,\ 0.4,\ 0.0,\ 0.0,\ -0.4,\ 1.2]\end{aligned} \tag{6.8}$$

$$\begin{aligned}\text{brdf}[1] = [&1.6,\ 0.02,\ 0.0,\ 0.0,\ 0.02,\ 1.75,\ 0.0,\ 0.0,\\ &0.0,\ 0.0,\ -1.15,\ 0.35,\ 0.0,\ 0.0,\ -0.35,\ 1.15]\end{aligned} \tag{6.9}$$

$$\begin{aligned}\text{brdf}[2] = [&1.7,\ 0.03,\ 0.0,\ 0.0,\ 0.03,\ 1.8,\ 0.0,\ 0.0,\\ &0.0,\ 0.0,\ -1.1,\ 0.3,\ 0.0,\ 0.0,\ -0.3,\ 1.1]\end{aligned} \tag{6.10}$$

along with information indicating the wavelength associated with each spectral vector location.

The reflected radiances are calculated as such

$$\mathbf{L_{out}}(450\text{nm}) = \begin{pmatrix} 1.5 & 0.01 & 0 & 0 \\ 0.01 & 1.7 & 0 & 0 \\ 0 & 0 & -1.2 & 0.4 \\ 0 & 0 & -0.4 & 1.2 \end{pmatrix} \begin{pmatrix} 5.0 \\ 2.0 \\ -1.0 \\ 0.0 \end{pmatrix} = \begin{pmatrix} 5.02 \\ 3.45 \\ 1.10 \\ 0.40 \end{pmatrix} \tag{6.11}$$

$$\mathbf{L_{out}}(550\text{nm}) = \begin{pmatrix} 1.6 & 0.02 & 0 & 0 \\ 0.02 & 1.75 & 0 & 0 \\ 0 & 0 & -1.15 & 0.35 \\ 0 & 0 & -0.35 & 1.15 \end{pmatrix} \begin{pmatrix} 6.0 \\ 0.0 \\ -2.5 \\ 1.0 \end{pmatrix} = \begin{pmatrix} 9.600 \\ 0.120 \\ 3.225 \\ 2.025 \end{pmatrix} \tag{6.12}$$

$$\mathbf{L_{out}}(650\text{nm}) = \begin{pmatrix} 1.7 & 0.03 & 0 & 0 \\ 0.03 & 1.8 & 0 & 0 \\ 0 & 0 & -1.1 & 0.3 \\ 0 & 0 & -0.3 & 1.1 \end{pmatrix} \begin{pmatrix} 7.0 \\ 0.0 \\ 0.0 \\ 0.0 \end{pmatrix} = \begin{pmatrix} 11.90 \\ 0.21 \\ 0.00 \\ 0.00 \end{pmatrix} \tag{6.13}$$

Notice that although there was no polarized information available for the 650 nm irradiance, the polarized BRDF at 650 nm produced a polarized reflection which was

automatical accounted for using the spectral vector methods. The results are then stored in another spectral vector.

6.2 The New BRDF Module Interface

In order to facilitate future upgrades and modifications to DIRSIG, much of the functionality is being modularized. Since no single BRDF model adequately represents all materials of interest, it was necessary to develop the capability to accommodate multiple methods of obtaining BRDF values. A new BRDF module and interface was developed to support multiple BRDF models. This approach provides a single common interface for the core part of DIRSIG to use when requesting a BRDF calculation. It also simplifies the task of integrating new BRDF models as they become available. By supporting multiple BRDF models, it is possible to associate a particular model with a specific material type. This enables the use of the most appropriate BRDF model for a given material in a scene.

The new BRDF module was implemented using a hierarchy of C++ classes. At the top is an abstract class which defines the interface for all of the individual BRDF models. Each BRDF model is then implemented as a subclass of the top level BRDF class. This approach ensures the core part of DIRSIG uses a single common interface with all of the BRDF models. Figure 6.2 shows this hierarchy of classes. Note that the Torrance and Sparrow BRDF model is more complicated than the simple Lambertian diffuse model. Therefore, the Torrance and Sparrow based model uses an additional class to estimate the diffuse scattering. The core part of DIRSIG is isolated from this level of detail and simply access both BRDF models through the common BRDF interface.

A database of BRDF values can be easily integrated into the new BRDF module.

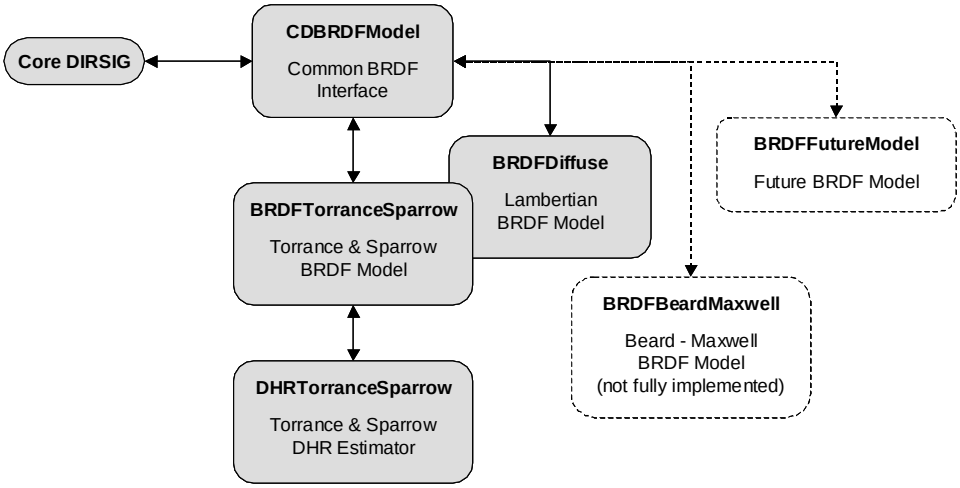

Figure 6.2: Relationship between the top level BRDF class, DIRSIG and the individual BRDF classes. The classes in white boxes with dashed lines are not fully implemented in the current version of DIRSIG and represent future expansion.

All that would be required is a new BRDF class which knows the structure of the database and can fulfill requests from the BRDF interface. The database class could be built to perform interpolation and extrapolation as desired based on the database population. Since no such databases currently exist, this capability was not added as a part of this effort.

Currently, only two BRDF models have been implemented in the new version of DIRSIG. Both models are described in the following sections.

6.2.1 Torrance-Sparrow BRDF Model

A Torrance and Sparrow based BRDF model was implemented as the primary polarimetric BRDF model. I implemented the model as described by Priest and Germer (2002) with the addition of the diffuse term estimation as described by Wellems et al. (2000). As implemented, the model requires three parameters: the complex index of refraction (n and k) and the surface roughness. The model assumes a normal

random distribution for the zenith angles of the microfacet normals. The standard deviation (σ) of this distribution is the surface roughness and has units of radians. As implemented, all three parameters can vary spectrally.

Strictly speaking, the surface roughness parameter should not be dependent upon wavelength since it is derived from the distribution of the microfacet normals. However, the limited set of parameter values available from AFRL allows the surface roughness parameter to vary as a function of wavelength in an effort to get a better fitting model. This is an example of the delicate trade-offs that have to be made due to a lack of measured data and more sophisticated physical models.

A database of estimated DHR values for perfectly reflecting microfacet surfaces of varying surface roughness was built. This database is then used by the Torrance and Sparrow BRDF model to estimate the magnitude of the diffuse term added to the microfacet specular returns predicted by the model. This database was precalculated using a 500,000 point hemispherical integration to obtain a high fidelity for the DHR estimates. When the BRDF model requests a value not in the look up table (LUT), its value is interpolated from the four nearest neighbors. Pre-computing the LUT, avoids a significant amount of computations during runtime. Since the DHR values are only dependent on zenith angle and surface roughness, they are reusable from one material to the next. The user has the option of turning the diffuse term on or off.

The simplicity and first principles base approach of the Torrance and Sparrow model makes it an ideal candidate for inclusion in the DIRSIG model. However, the simple assumptions of this BRDF model result in some significant limitations. The model only accounts for first surface scattering and is not well suited for materials with significant volume scattering contributions. The only depolarizing contribution comes from the DHR estimation.

The model assumes knowledge of the material's complex index of refraction. In practice, the complex index of refraction is a very difficult parameter to measure. One approach determines the three model parameters empirically for a given material sample based on a series of BRDF measurements. A major disadvantage of this approach is the abandonment of the first principles nature of the model. The resulting parameter values simply become empirical quantities which are not necessarily constrained by their physical representations.

The polarimetric modeling and simulation branch of AFRL has been exploring the usefulness of the Torrance and Sparrow BRDF model for a variety of materials. They have a very small database of parameters for about ten materials at two visible wavelengths (550nm and 650nm). In the case of elemental metals (i.e. gold, silver, aluminum, copper, etc.) tables of n and k values exist which can be used along with an estimate of the material's surface roughness.

6.2.2 Lambertian BRDF Model

Initially, one would not think of a Lambertian BRDF model as a polarized BRDF model. However, since a truly Lambertian surface totally depolarizes all reflections, it requires a polarized BRDF model. The model requires a single parameter value, the diffuse reflectance as a function of wavelength. It simply returns the same Mueller matrix for any valid geometry. The Mueller matrix is that of a totally depolarizing element and contains all zeros except for the upper left corner which contains the

diffuse BRDF value (ρ_d):

$$\text{Lambertian BRDF} = \begin{pmatrix} \rho_d & 0 & 0 & 0 \\ 0 & 0 & 0 & 0 \\ 0 & 0 & 0 & 0 \\ 0 & 0 & 0 & 0 \end{pmatrix}. \tag{6.14}$$

The "unpolarized" extension of the depolarizing Lambertian BRDF model simply places the diffuse BRDF along the major diagonal of the Mueller matrix:

$$\text{Unpolarized Lambertian BRDF} = \begin{pmatrix} \rho_d & 0 & 0 & 0 \\ 0 & \rho_d & 0 & 0 \\ 0 & 0 & \rho_d & 0 \\ 0 & 0 & 0 & \rho_d \end{pmatrix}. \tag{6.15}$$

This has the effect of preserving the polarization of the incident radiance while attenuating the reflected radiance by the diffuse reflectance. This is referred to as an "unpolarized", or polarization neutral, BRDF since it does not alter the polarization state of the reflected radiance.

The most general case combines the two extremes. A scale factor, $0 \leq s \leq 1$ is added to the three lower diagonal elements

$$\text{Generalized Lambertian BRDF} = \begin{pmatrix} \rho_d & 0 & 0 & 0 \\ 0 & s\,\rho_d & 0 & 0 \\ 0 & 0 & s\,\rho_d & 0 \\ 0 & 0 & 0 & s\,\rho_d \end{pmatrix} \tag{6.16}$$

which has the effect of scaling how much the BRDF depolarizes the reflections. The value of s can be estimated by measuring the degree of polarization for fully polarized light reflected by the Lambertian material.

The Lambertian model provides the user with an option of returning a totally depolarizing diffuse BRDF (standard Lambertian definition) or an "unpolarized" BRDF which does not alter the polarization upon reflection.

6.2.3 BRDF Sampling

The top level BRDF class, CDBRDFModel, supports three methods of automatically sampling the BRDF function. This provides the radiometry model within DIRSIG a simple way of consistently sampling the background radiance field at each bounce while ray tracing. The three methods provide varying degrees of complexity and flexibility in controlling the BRDF sampling. In all three cases, the maximum zenith angle can be specified to prevent sampling a BRDF model where it begins to break down or becomes mathematically unstable.

6.2.3.1 Random BRDF Sampling

The simplest sampling method randomly samples the BRDF and background radiance. The interface requires only the total number of samples desired and the maximum allowable zenith angle. It returns a set of randomly generated sample points along with a uniformly estimated solid angle for each of the sample points. The random sampling function makes the simplifying assumption that the solid angle associated with each sample point is simply 2π divided by the total number of sample points. This assumption ignores the fact that the solid angle is actually a function of zenith angle. As the number of sample points increases, the validity of this assumption becomes less critical.

6.2.3.2 Uniform Grid BRDF Sampling

The next level of complexity involves specifying a uniform grid over which to sample the BRDF function. This sampling function requires the desired number of azimuth and zenith samples. It then creates a grid spaced uniformly in azimuth and zenith. Once again, the maximum zenith angle can be specified.

The advantage of this approach is the ability to accurately calculate the solid angle associated with each sample point. Unfortunately, this method tends to over sample the "top" of the BRDF (i.e. small zenith angles) since the spacing between azimuth samples decreases with decreasing zenith angle.

Previous DIRSIG research has discovered problems associated with a rigid uniform sampling grid approach. The discrete nature of the sampling grid leads to harsh transitions in shadow regions and "star" shaped artifacts. This results from the fact that adjacent ray intersections always sample in the exact same directions. To help alleviate this problem, the uniform sampling routine implemented provides an optional deviation parameter can be specified to control how far from the uniform grid each sample point is allowed to deviate. The deviations are random in nature and weighted toward the center of each sampling bin. If the sample points are not allowed to vary significantly in zenith, the solid angles computed based on the center point of each sampling bin will be very close approximations. Once again, the effects of this simplification decrease as the number of sample points increases.

6.2.3.3 Adaptive BRDF Sampling

The most complex sampling scheme implemented attempts to sample the BRDF in the most significant regions. As a material's BRDF increases in specularity, the relevant sampling region decreases. In other words, it is not necessary, or desirable,

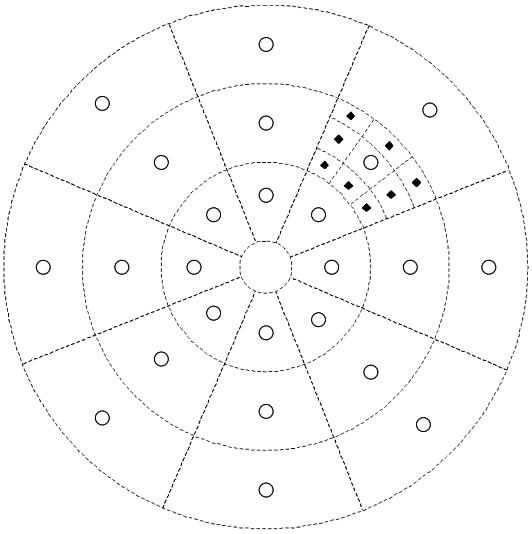

Figure 6.3: Example adaptive sampling grid. The gray circles represent the initial 24 sampling points. The black diamonds represent the next level of sampling. The radial lines are the zenith axes and the circular lines are the azimuthal axes.

to cast rays in directions where the BRDF is significantly reduced in value. Most of the total integrated radiance will come from the specular direction. Therefore, the third sampling approach uses an adaptive method to determine where best to cast a given number of rays.

The adaptive sampling function samples the BRDF using an adaptive approach which uses a score value obtained from the specific BRDF model being sampled. The sampling function begins by sampling the BRDF at 24 uniformly spaced points. It then subsamples at the highest scoring point. The subsampling adds eight more points to the sample pool. The next highest scoring sample is then subsampled to yield eight more sample points. This process is repeated until the requested number of sample points are obtained. Figure 6.3 shows an example of the first two steps of this process. The function then returns the list of sample points along with the associated solid angles.

6.3 Low Level Code Testing and Validation

Since this effort was part of the overall DIRSIG rewrite, it was necessary to perform rigorous testing and validation of each of the C++ classes developed to support the polarimetric calculations. Table 6.1 lists the classes which were primarily developed and tested as part of this research effort. Each class was rigorously tested to verify its output and performance under a wide range of inputs to ensure a high level of confidence. By rigorously testing each of these classes independently and in small groups, we were able to verify they worked as desired. This greatly simplifies future validation efforts by ensuring the low level functions perform accurately. In several cases, we built specialized testing programs which can be used to verify future upgrades and modifications to the classes developed under this effort.

CDPolarimetricMath	CDVector
CDSpectralVector	CDSpectralLocation
CDSpectralPoint	CDSpectralUnits
CDBRDFModel	BRDFDiffuse
BRDFTorranceSparrow	DHRTorranceSparrow

Table 6.1: List of DIRSIG classes developed and tested primarily as a part of this research effort.

6.4 Atmospheric Modeling

DIRSIG uses MODTRAN (Berk et al. 1989) to calculate solar and skylight radiance values as well as atmospheric transmissions. The current public release version of MODTRAN does not support polarimetric calculations. However, DIRSIG's modular

design will easily incorporate an upgraded polarimetric version of MODTRAN as soon as it becomes publicly available.

A polarized version of MODTRAN is currently being developed by AFRL. The DIRSIG development team is working closely with AFRL to ensure the polarized version of MODTRAN will integrate with DIRSIG as soon as it is available. The polarized version of MODTRAN hasn't been fully validated and is currently in developmental testing. Therefore we used this version to produce plausible polarized sky illumination and performed some limited sensitivity analysis to determine how finely the sky dome needs to be sampled.

6.5 Polarized Sensor Model

The DIRSIG sensor models will be polarized on a per pixel basis using a Mueller matrix transformation function. This approach allows the user to fully characterize the polarimetric response of a real or simulated sensor. By characterizing the sensor on a pixel-by-pixel basis, it is possible to introduce polarization sensitivities as a function of the focal plane location. DIRSIG is not intended to model each internal component of a sensor; therefore, it does not perform a rigorous physics based simulation of the optical components. However, it does model many of the physical aspects like platform motion, off-axis imaging, and image formation techniques (i.e. framing array versus scanning systems) which contribute to the overall system MTF and allows the user to describe the net effects of detailed sensor models for each detector element.

A simple example of how the polarized sensor model can be used involves simulating a four camera polarimetric imaging system. Each camera is modeled as a 2-D framing array system with a polarizing filter in front of the optics. The filters are chosen such that the four resulting images can be processed to produce S_0 through S_3

Stokes parameter images. This type of system can be easily simulated in DIRSIG by applying the appropriate Mueller matrix for each filter to the radiance field reaching each of the four cameras. If a per pixel calibration is available for each of the four cameras, a different Mueller matrix can be specified for each pixel in the system. This type of approach can be expanded to any type of imaging system DIRSIG supports.

The upgraded DIRSIG sensor model is part of a separate effort which was not completed in time to be tested as part of this research effort. Therefore, a representative example of the capabilities that will be available was generated. All of the required polarization tools are ready and available for the sensors team to integrate into the new sensor model as it is built.

6.6 BRDF Model Characterization

An important part of implementing the modified Torrance and Sparrow BRDF model was a characterization of the model performance as a function of the three input parameters. The parameters are associated with real physical quantities which are not always easy to directly measure. Therefore, it was useful to characterize the behavior of the modeled BRDF based on variations in the three input parameters. This information will assist users in selecting plausible parameter values in the absence of physically derived parameter values.

A majority of the characterization focused on the shape of the BRDF as a function of the three parameters. The results of the BRDF characterization are given in section 7.3. This was followed by a few simple DIRSIG sensor simulations which demonstrate how these changes in the BRDF impact the images. The images are presented in section 7.6.

6.7 Sensitivity Analysis

One of the biggest unknowns when using a ray based simulation is how many rays must be used to get a reasonable sampling of the scene illumination. Using too few rays can result in significant errors and harsh unrealistic shadows. Using too many rays consumes too many computer resources and increases the simulation time. A very simple geometric scene was used to characterize the sensitivity associated with sampling the sky dome radiance. The same geometry was used with a variety of material parameters to also asses the impact of different materials on the required sampling fidelity.

6.8 Summary

The major efforts of this research resulted in significant modifications to the central part of DIRSIG. The data storage and handling routines were enhanced to handle polarized data along with unpolarized data. More efficient spectral vector data storage and handling was also developed. All of these fundamental changes to DIRSIG were tested and verified to ensure accurate implementation of the new tools. A new BRDF interface was developed and two BRDF models were built and tested with the new interface. The BRDF module now handles the task of sampling the hemisphere over the target. This allows the BRDF model to influence the sampling of the hemisphere based on the shape and location of the specular lobe. Finally a series of simple simulations were performed to test and demonstrate the interaction of the new polarimetric features. The results of all the testing and characterization are presented in the next chapter.

Chapter 7

Results

> All of physics is either impossible or trivial. It is impossible until you understand it, and then it becomes trivial.
>
> Ernest Rutherford
> *English physicist, Nobel prize for chemistry 1908.*

7.1 DIRSIG Radiometry Validation

7.1.1 Validation of Polarized Radiometry Calculations

A set of polarized radiometry calculations for a simple flat plate geometry were performed by hand and compared with the results of a DIRSIG simulation. The simulations and calculations used a copper plate and a monochromatic 600 nm illumination field. This comparison verifies the integration of the ray tracing and radiometry modules within the new version of DIRSIG. Figure 7.1 shows the geometry used to validate the radiometric calculations.

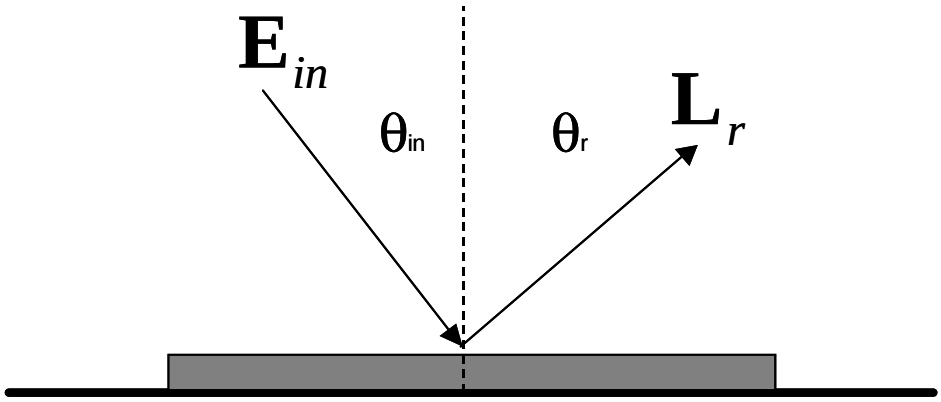

Figure 7.1: Flat plate geometry used to verify DIRSIG radiometry calculations.

The reflected radiance was calculated using the following equation:

$$\mathbf{L}_r \left[\frac{\mathrm{W}}{\mathrm{m}^2\,\mathrm{sr}}\right] = \boldsymbol{f}[\mathrm{sr}^{-1}]\,\mathbf{E}_{in} \left[\frac{\mathrm{W}}{\mathrm{m}^2}\right] \cos(\theta_{in}). \tag{7.1}$$

The following zenith (θ) and azimuth (ϕ) angles were used:

$$\theta_{in} = 30^\circ \tag{7.2}$$

$$\theta_r = 40^\circ \tag{7.3}$$

$$\phi = 180^\circ. \tag{7.4}$$

The following parameter values were used with the Torrance-Sparrow BRDF model to calculate the polarized BRDF

$$n = 0.405 \tag{7.5}$$

$$k = 2.950 \tag{7.6}$$

$$\sigma = 0.2 \text{ rad.} \tag{7.7}$$

The n and k values were interpolated from CRC tables (Weast and Lide 1990). The

Input		Output			
		Manual Calc		DIRSIG Calc	
$\mathbf{E}_{in}$	Stats	$\mathbf{L}_r$	Stats	$\mathbf{L}_r$	Stats
$\begin{pmatrix}100\\0\\0\\0\end{pmatrix}$	$DoP:\ 0\%$ $DoLP: 0\%$ $DoCP: 0\%$	$\begin{pmatrix}102.2\\3.464\\0\\0\end{pmatrix}$	$DoP:\ 3.4\%$ $DoLP: 3.4\%$ $DoCP:\ 0\%$	$\begin{pmatrix}102.2\\3.474\\0.0056\\0\end{pmatrix}$	$DoP:\ 3.4\%$ $DoLP: 3.4\%$ $DoCP:\ 0\%$
$\begin{pmatrix}100\\30\\40\\0\end{pmatrix}$	$DoP:\ 50\%$ $DoLP: 50\%$ $DoCP:\ 0\%$	$\begin{pmatrix}103.2\\33.91\\-39.18\\-10.48\end{pmatrix}$	$DoP:\ 51.2\%$ $DoLP: 50.2\%$ $DoCP: 10.2\%$	$\begin{pmatrix}103.2\\34.07\\-39.07\\-10.49\end{pmatrix}$	$DoP:\ 51.2\%$ $DoLP: 50.2\%$ $DoCP: 10.2\%$
$\begin{pmatrix}100\\20\\30\\60\end{pmatrix}$	$DoP:\ 70\%$ $DoLP: 36.1\%$ $DoCP:\ 60\%$	$\begin{pmatrix}102.9\\23.76\\-13.66\\-66.63\end{pmatrix}$	$DoP:\ 70\%$ $DoLP: 26.6\%$ $DoCP: 64.8\%$	$\begin{pmatrix}102.9\\23.86\\-13.56\\-66.60\end{pmatrix}$	$DoP:\ 70.1\%$ $DoLP: 26.7\%$ $DoCP: 64.8\%$

Table 7.1: List of input irradiances, reflected radiances (calculated manually and by DIRSIG) and the degrees of polarization used for radiometric validation.

polarized BRDF for this geometry was calculated to be

$$\boldsymbol{f} = \begin{pmatrix} 1.18 & 0.04 & 0 & 0 \\ 0.04 & 1.172 & 0 & 0 \\ 0 & 0 & -1.131 & 0.3026 \\ 0 & 0 & -0.3026 & 1.131 \end{pmatrix}. \tag{7.8}$$

Table 7.1 lists the three input radiance values chosen to validate the radiometry calculations. The three radiances were chosen to have three distinct levels of polarization. The first one was totally unpolarized, the second one had only linear polarization, and the third one had linear and circular polarization.

To reproduce these results, three DIRSIG simulations were performed using a large square flat plate with a single point source illumination field. The scene was imaged

using a 128×128 pixel framing array at the appropriate viewing angle. The following vectors were used to set up the illumination and viewing geometries

$$Illumination = \begin{pmatrix} -0.5 \\ 0 \\ 0.866 \end{pmatrix} \tag{7.9}$$

$$View = \begin{pmatrix} 0.643 \\ 0 \\ 0.766 \end{pmatrix} \tag{7.10}$$

The center pixel of the image was used to compare with the hand calculations. Comparisons of the manual and DIRSIG calculations are given in table 7.1.

The slight differences between the hand calculations and the DIRSIG results can be attributed to computational round-off errors and the fact that the center point of the square facet was precisely on the edge between the two center pixels. For example, in the DIRSIG simulation, the S_3 value in the first case had equal magnitudes and opposite signs for each of the pixels on either side of the center line. Therefore, averaging these two pixels would agree exactly with the hand calculation of zero for that particular case.

7.1.2 Polarized Versus Unpolarized Computations

A set of representative radiometry calculations based on the calculations in the previous section were performed using polarized and unpolarized computations to determine the expected level of differences. Depending upon the polarization sensitivity of the sensor and the degree of polarization of the illuminating field, the results indicate there there can be as much as a 5% or greater difference in predicted results

when using polarized versus unpolarized calculations. In each case, the unpolarized calculations predicted less total radiance reaching the sensor.

7.1.2.1 Differences in Sensor Reaching Radiance Calculations

The first set of calculations compares the differences in the predicted sensor reaching radiance and used the same conditions and geometry presented in the previous section. Eleven calculations were performed. The total irradiance (i.e. E_0) remained constant at $100\frac{W}{m^2}$ while the degree of linear polarization was varied from 0.0 to 1.0. The desired DoLP values were obtained by varying the E_1 Stokes value of the irradiance while E_2 and E_3 remained fixed at 0.0.

For all eleven cases, the unpolarized calculation produced the same result for the total sensor reaching radiance and is given by the following equations:

$$L_{unpolarized} = f_{00}\, E_0\, \cos\theta_{in} \tag{7.11}$$

$$= (1.18)(100)(0.866) \tag{7.12}$$

$$= 102.19\ \left[\frac{W}{m^2\, sr}\right] \tag{7.13}$$

Using the polarized calculations resulted in the following equations:

$$L_{polarized} = (f_{00}\, E_0 + f_{01}\, E_1)\cos\theta_{in} \tag{7.14}$$

The results of the polarized calculations are given in table 7.2. The percent error compares the total sensor reaching radiance predicted by the polarized calculations to that predicted by the unpolarized calculations. Clearly as the DoLP of the irradiance field increases, the differences between the two sets of calculations increases. The polarized BRDF Mueller matrix will also influence the amount of the differences as well. When predicting only the total sensor reaching radiance, only the first column of the BRDF Mueller matrix is significant and the remainder of the Mueller matrix can

DoLP	Polarized L_0	Error
0.0	102.19	0.0 %
0.1	102.54	0.3 %
0.2	102.88	0.7 %
0.3	103.23	1.0 %
0.4	103.58	1.4 %
0.5	103.92	1.7 %
0.6	104.27	2.0 %
0.7	104.62	2.4 %
0.8	104.96	2.7 %
0.9	105.31	3.1 %
1.0	105.66	3.4 %

Table 7.2: Total sensor reaching radiance predicted using polarized calculations as a function of irradiance DoLP and the resulting error compared to the unpolarized prediction.

be safely ignored. However, the remainder of the BRDF Mueller matrix is required for a full polarimetric characterization of the sensor reaching radiance.

7.1.2.2 Differences in Sensor Detected Radiance Calculations

The second set of calculations compares the differences in the predicted sensor detected radiance and used the same conditions and geometry presented in the previous section. This time however, instead of varying the DoLP of the irradiance, the DoP was varied instead. The desired DoP was achieved by setting $E_1 = E_2 = E_3 = S$ so that the polarization was equally divided among the Stokes parameters. The value of S is given by

$$S = \frac{E_0 \, \mathrm{DoP}}{\sqrt{3}} \tag{7.15}$$

where DoP is the desired DoP level.

Once again, the unpolarized equations result in the same value as before, $102.19 \frac{W}{m^2 \, sr}$. Since the unpolarized calculations do not take into account sensor polarization sen-

sitivities, the predicted detected radiance value is the same as the predicted sensor reaching value.

For the polarized calculations, a generic sensor hypothetical sensor was used. Two different polarization sensitivities were studied: 1% and 5%. The detector's Mueller matrix was calculated using the following equation:

$$M_{detector} = \begin{pmatrix} 1 & 1+s & 1+s & 1+s \\ 1+s & 1+s & 0 & 0 \\ 1+s & 0 & 1+s & 0 \\ 1+s & 0 & 0 & 1+s \end{pmatrix} \tag{7.16}$$

where s is the detector's polarization sensitivity.

Eleven sets of polarization calculations were performed for DoP values ranging from 0.0 to 1.0. The results are given in tables 7.3 and 7.4 for a 1% and 5% polarization sensitive detectors.

The results clearly show better agreement between the polarized calculations and the sensor's detected value than the unpolarized calculations and the sensor's detected value. As the degree of polarization increases, the differences also increase.

Assuming an acceptable error tolerance of 1%, the results for a 1% polarization sensitive sensor indicates unpolarized calculations will suffice for irradiance fields with 30% or less polarization. Simply performing polarized radiative transfer calculations without characterizing the sensor will suffice for irradiance fields with 80% or less polarization. For this scenario, only very highly polarized irradiance fields require polarization calculations and full sensor characterization. For the 5% sensitive detector, these thresholds drop to about 10% and 15% polarized irradiance fields.

The required level of polarization characterization and computation complexity is clearly dependent on several factors. These factors include the polarization level of

	Sensor Reaching L_0		Detected L_0	Error	
DoP	Unpol calc	Pol calc	Pol calc	UnPol vs Det	Pol vs Det
0.0	102.19	102.19	102.23	0.03 %	0.03 %
0.1	102.19	102.39	102.56	0.36 %	0.16 %
0.2	102.19	102.59	102.89	0.68 %	0.29 %
0.3	102.19	102.79	103.22	1.00 %	0.41 %
0.4	102.19	102.99	103.55	1.33 %	0.54 %
0.5	102.19	103.19	103.88	1.65 %	0.66 %
0.6	102.19	103.39	104.21	1.97 %	0.79 %
0.7	102.19	103.59	104.54	2.30 %	0.91 %
0.8	102.19	103.79	104.87	2.62 %	1.04 %
0.9	102.19	103.99	105.20	2.94 %	1.16 %
1.0	102.19	104.19	105.53	3.27 %	1.28 %

Table 7.3: Comparison of sensor reaching and detected total radiances for a 1% polarization sensitive sensor. The error values show the differences between the detected value and the polarized and unpolarized sensor reaching computations.

	Sensor Reaching L_0		Detected L_0	Error	
DoP	Unpol calc	Pol calc	Pol calc	UnPol vs Det	Pol vs Det
0.0	102.19	102.19	102.36	0.17 %	0.17 %
0.1	102.19	102.39	102.22	1.00 %	0.81 %
0.2	102.19	102.59	102.07	1.84 %	1.44 %
0.3	102.19	102.79	103.92	2.67 %	2.07 %
0.4	102.19	102.99	103.77	3.50 %	2.70 %
0.5	102.19	103.19	103.62	4.34 %	3.32 %
0.6	102.19	103.39	104.47	5.17 %	3.95 %
0.7	102.19	103.59	104.32	6.00 %	4.57 %
0.8	102.19	103.79	104.18	6.83 %	5.19 %
0.9	102.19	103.99	105.03	7.67 %	5.80 %
1.0	102.19	104.19	105.88	8.50 %	6.42 %

Table 7.4: Comparison of sensor reaching and detected total radiances for a 5% polarization sensitive sensor. The error values show the differences between the detected value and the polarized and unpolarized sensor reaching computations.

the irradiance field, the polarization characteristics of the BRDF Mueller matrix, and the polarization sensitivity of the detector.

7.2 Validation of BRDF Model Implementation

Two tests were conducted to verify the integration of the Torrance-Sparrow BRDF model into DIRSIG. The first test compared the Torrance-Sparrow BRDF model with theoretical results predicted by Fresnel reflections. The second test used the DIRSIG implementation of the Torrance-Sparrow BRDF to reproduce the data in figures 5 and 6 of Priest and Germer (2002).

7.2.1 Comparison of DIRSIG BRDF and Fresnel Theory

DIRSIG's implementation of the Torrance-Sparrow BRDF model was used to predict the degree of polarization (DoP) for unpolarized light reflected from a smooth dielectric surface. The results are shown in figure 7.2. The surface had a complex index of reflection of $n = 2.0$ and $k = 0.0$. A surface roughness of $\sigma = 0.05$ rad was used to represent a very smooth surface. The theoretical data was calculated using the Fresnel reflection equations. Figure 7.2 shows excellent agreement between DIRSIG and the theoretical calculations.

7.2.2 Comparison of DIRSIG and Priest-Germer Results

The DIRSIG implementation of the Torrance-Sparrow BRDF was used to reproduce the results of Priest and Germer (2002). The results are shown in figure 7.3. Note that the data for the Priest and Germer plot lines was hand digitized using a PDF file of the published results. The data in both plots used an incident angle of

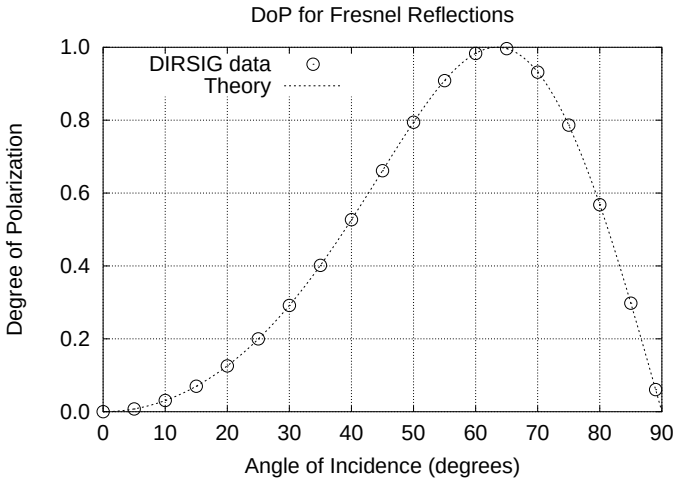

Figure 7.2: Comparison of DIRSIG Torrance-Sparrow BRDF with Fresnel reflection theory. The degree of polarization for a very smooth dielectric surface ($n = 2.0$ $k = 0$) was calculated using DIRSIG and the Fresnel reflection equations.

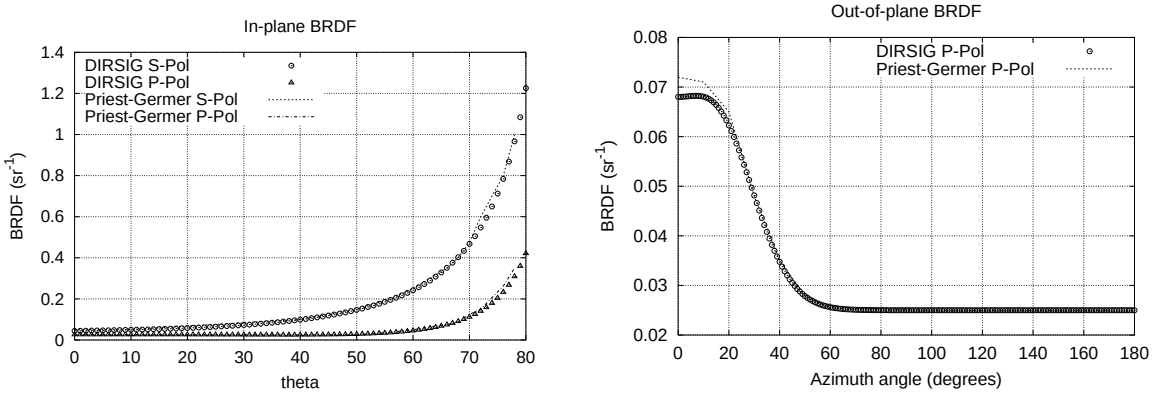

(a) Priest and Germer figure 5

(b) Priest and Germer figure 6

Figure 7.3: Comparison of DIRSIG and Priest and Germer (2000) Torrance-Sparrow BRDF calculations. The Priest and Germer data was hand digitized. The Torrance-Sparrow BRDF parameters for both plots were: $n = 1.25$, $k = 0$, and $\sigma = 0.3$ rad.

65° an index of refraction of $n = 1.25$ and $k = 0$, and a surface roughness of $\sigma = 0.3$. The in-plane results compare very nicely with the Priest and Germer results. The out-of-plane results differ slightly as the azimuth angle approaches zero.

7.3 Torrance-Sparrow BRDF Model Characterization

The complex nature of a fully polarimetric BRDF is difficult to capture in a single figure. The following sections show the effects of variations in the modified Torrance-Sparrow BRDF model parameters. A combination of zenith and azimuthal plots are used to quantitatively characterize the BRDF. The variation in specular lobe width and location is characterized. A full characterization of the polarized BRDF model requires analyzing all sixteen Mueller matrix elements. To simplify the characterization, only those elements most significant when dealing with unpolarized illumination are presented. In the following sections, the notation f_{ij} refers to the $[i, j]$ element of the BRDF Mueller matrix.

7.3.1 Surface Roughness Effects

The surface roughness parameter, σ, has a large impact on the shape and characteristic of the BRDF. Plots of the f_{00} element of the BRDF Mueller matrix correlate closely to unpolarized BRDF values. Plots of f_{00} in the plane of incidence (i.e. $\phi_i - \phi_r = \pm 180^\circ$) show the specular lobe characteristics of the BRDF model (see figure 7.4).

The BRDF plots in figure 7.4 are for roughened aluminum. The simulations used values of $n = 1.304$ and $k = 7.479$ which correspond to a wavelength of 620 nm(Weast and Lide 1990). The incident zenith angle is 45° and a Gaussian microfacet distri-

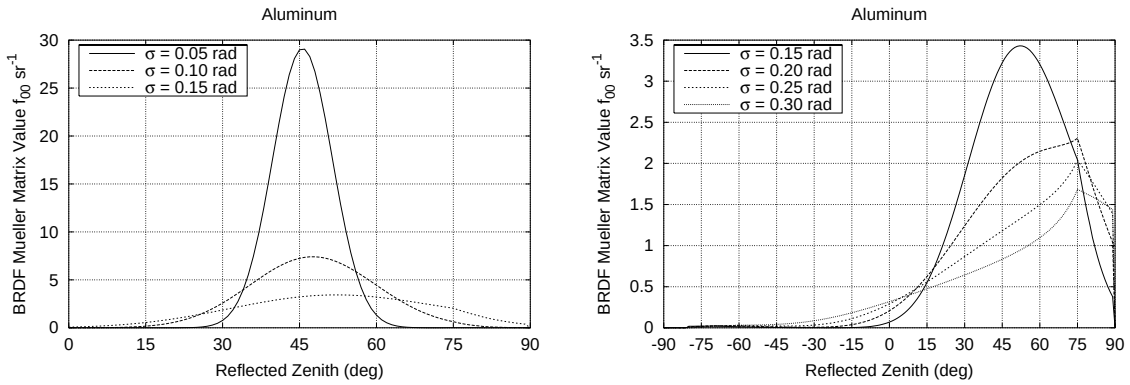

(a) Smooth surfaces (b) Rough surfaces

Figure 7.4: In-plane Torrance-Sparrow BRDF (f_{00} Mueller matrix element) plotted as a function of the reflected zenith angle. for an incident zenith angle of 45°.

bution was used. The plots show how the surface roughness parameter, σ, affects the specular lobe shape and location. As the roughness increases, the BRDF becomes less specular, the lobe width increases, and the peak of the lobe shifts to larger zenith angles. The shift in forward scattering is predicted by the model and was observed in measured data by Torrance and Sparrow(Torrance and Sparrow 1967). The rougher surfaces (figure 7.4(b)) also show the effects of the shadowing function which is prominent above 75°.

The azimuthal characteristics of the polarization sensitive elements f_{10} and f_{20} are shown in figure 7.5. For the case of unpolarized illumination, these two Mueller matrix elements determine the amount and orientation of the linear polarization in the reflected radiance. Once again, the shape of the curves decrease in height and increase in width as the roughness increases. Also note that f_{10} peaks and f_{20} changes sign as the reflected angle passes through the plane-of-incidence (i.e. reflected azimuth = 180°).

The plots in Figure 7.6 show how the location and width of the specular lobe varies

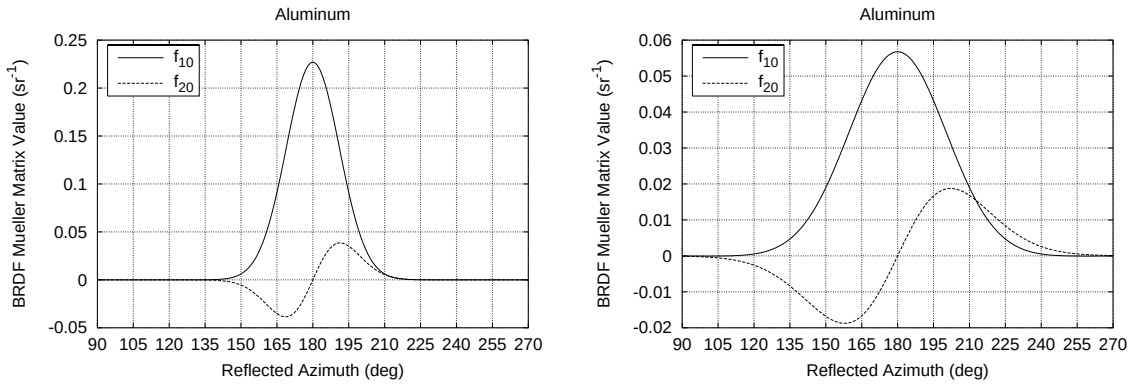

(a) Smooth surface, $\sigma = 0.10$ rad

(b) Rough surface, $\sigma = 0.20$ rad

Figure 7.5: Out-of-plane Torrance-Sparrow BRDF (f_{10} and f_{20} Mueller matrix elements) plotted as a function of the reflected azimuth angle for an incident zenith angle of 45°.

as a function of the incident zenith angle and the surface roughness. Once again, values of $n = 1.304$ and $k = 7.479$ were used. The forward shift of the specular lobe location is linear for zenith angles less than 50°. The specular lobe width was defined as the full width at half the maximum value (FWHM). The lobe width is dependent mostly on the surface roughness. As the surface roughness increases, the lobe width tends to increase slightly with increasing zenith angles. The large decrease in lobe width for the roughest materials is actually caused by a "clipping" or "masking" of the specular lobe at the horizon. Since the specular lobe can't extend past a zenith of 90°, the lobe width is truncated at the horizon resulting in artificially small widths as the lobe's location approaches the horizon. This phenomenon is shown in figure 7.4(b).

7.3.2 Index of refraction effects

The previous section presented the effects of varying the material's surface roughness parameter. Now we present the impacts of varying the values of n and k. The

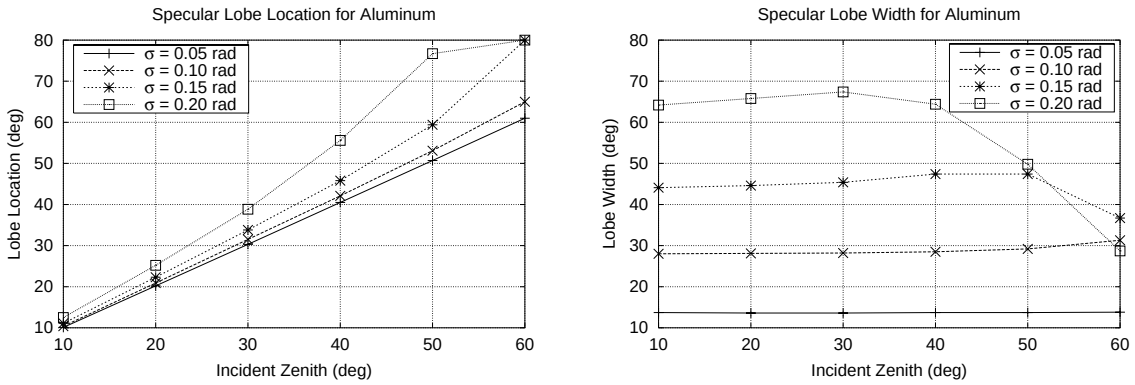

Figure 7.6: Torrance-Sparrow BRDF specular lobe characteristics for Aluminum at 620 nm.

values of n and k are instrumental in identifying the material. For example non-metallic materials tend to have small k values or k values of zero. Whereas metals will have significantly larger k values. One of the most common optical characteristics associated with the index of refraction is the Brewster angle (or pseudo-Brewster angle for metals). The values of n and k also have a large impact on the BRDF characteristics.

The plots in figure 7.7 show the effects of varying the real part of the index of refraction, n while holding k constant at 0. The zenith angle of the incident energy was 10° and the reflected angle was kept in the plane of incidence. The two graphs show how the surface roughness interacts to create a specular versus diffuse reflector. Both graphs exhibit secondary peaks at extremely high grazing angles. In this region, all four plots over lay each other. This phenomenon is caused by the addition of the estimated diffuse term. Since the diffuse term is only a function of the surface roughness, it will be the same for all materials. As the index of refraction increases, so does the magnitude and width of the specular lobe. However, unlike the surface roughness parameter, there is no shift in the location of the peak. The two graphs

also show how a small variation in the surface roughness parameter can lead to a quick transition from a highly specular material to a predominantly diffuse one. The transition is more pronounced for smaller values of n.

The plots in figure 7.8 show the effects of varying the imaginary part of the index of refraction, k, while holding n constant at 1.7 and σ constant at 0.2. The zenith angle of incident was 10° and the reflected angle was kept in the plane of incidence. The bottom curve ($k = 0$) in figure 7.8(a) is the same as the $n = 1.7$ curve in figure 7.7(b). This indicates that increasing the value of k increases both the specular lobe peak and lobe width without changing the lobe location.

Another significant effect of changing the value of k is the introduction of circular polarization which results in elliptical polarization when combined with the linear polarizations. The curves in figure 7.8(b) show that f_{23} becomes non-zero when k is non-zero. Since $f_{32} = -f_{23}$, the same applies for f_{32}. These two terms are responsible for converting ±45° linear polarization into circular polarization. Also note that the peak in f_{23} is not in the specular direction. Finally, the effects of the shadowing function start to appear around a zenith angle of 70°.

7.3.3 Comparison with Measured Data

Roughened metallic surfaces are excellent candidates for testing the modified Torrance and Sparrow BRDF model. Reflections from metal surfaces are dominated by first surface reflections and there is essentially no subsurface or volume scattering involved.

BRDF-like measurements were made of two copper plates (figure 7.9) using an ASD field spectrometer with a three degree field of view optic. The data measured are not truly BRDFs as defined by Nicodemus et al. (1992) because we used an extended

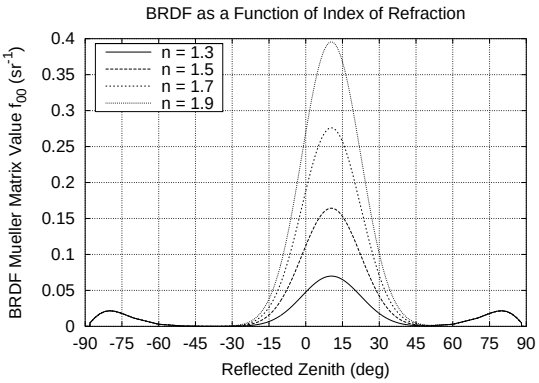

(a) $\sigma = 0.10$ rad

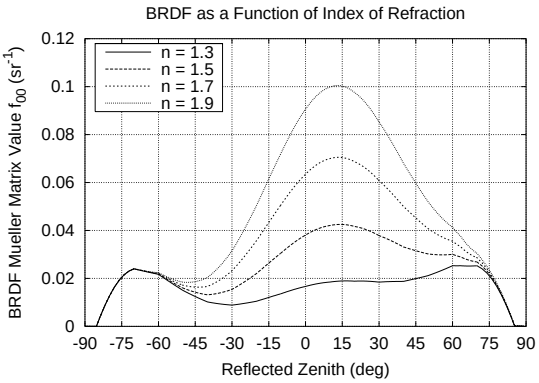

(b) $\sigma = 0.20$ rad

Figure 7.7: Torrance-Sparrow BRDF as a function of the real component of the index of refraction.

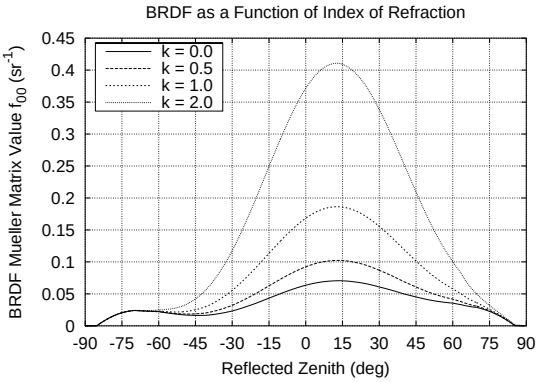

(a) f_{00}

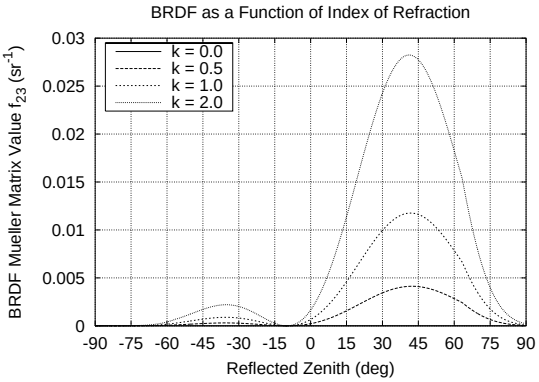

(b) f_{23} introduces circular polarization

Figure 7.8: Torrance-Sparrow BRDF as a function of the imaginary component of the index of refraction.

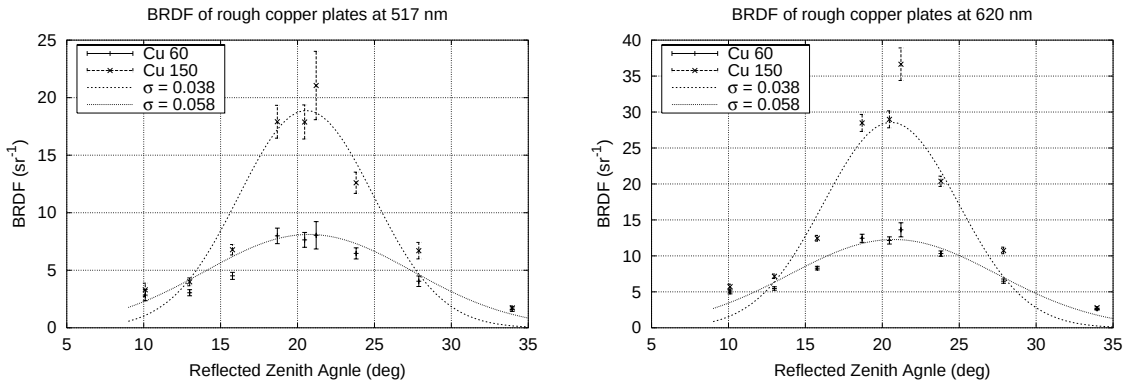

(a) 517 nm (b) 620 nm

Figure 7.9: Comparison of measured BRDF (points) and Torrance-Sparrow predicted BRDF (lines).

light source to provide an uniform illumination over the entire sample. The BRDF was estimated by calculating the ratio of the radiance reflected by the metal sample to the radiance reflected by a diffuse spectralon reference. Both copper plates were roughened by sandblasting them, one with 60 grit and the other with 150 grit sand.

The n and k values for the Torrance and Sparrow BRDF were obtained from the CRC tables (Weast and Lide 1990). Next, the Torrance and Sparrow BRDF was calculated for multiple surface roughnesses and the best curve was chosen for each data set. The process was repeated at two wavelengths to investigate if the surface roughness parameter is truly independent of wavelength as assumed by the model. Figure 7.9 shows that the Torrance and Sparrow predictions follow the general trend of the measured data. The most significant deviations occur outside the main lobe region. This suggests the distribution of microfacet normals may differ from the assumed Gaussian distribution. Better characterization of the microfacet distribution should improve the accuracy of the model.

Another factor contributing to the differences is the measurement of the incident

and reflected zenith angles. The light source and ASD optic were mounted on two separate tripods. While the light source remained fixed throughout all of the measurements, the detector's tripod was moved along a line in the plane of incidence. The angles were calculated using trigonometric relationships between the horizontal and vertical distances from the center of the sample. The linear distances could only be measured to an accuracy of about 5 mm. Finally, the intensity of the light source fluctuated with variations in the supply voltage. The effects of these fluctuations were reduced by taking 20 ASD samples for each data point and averaging the results.

7.3.4 Torrance and Sparrow BRDF Conclusions

The Torrance-Sparrow model provides a simple, physics based BRDF model that is well suited for materials dominated by first surface reflections. Being a physics based model, the user is required to have extensive knowledge about the materials optical and physical characteristics. Slight changes in the surface roughness have significant impacts on the specular nature of the predicted BRDF. The difficulty associated with directly measuring the complex index of refraction as a function of wavelength for a given material will severely limit the number of materials for which this model can be used.

The issue of characterizing common materials is common to any method used for modeling polarized and unpolarized BRDFs. The comparisons of the model results with the copper measurements indicates that using tabulated n and k values from common reference books, like the CRC handbook, appears to be a reasonable approach for metallic materials.

Research conducted at the Air Force Research Lab (AFRL) indicates that it might be possible to empirically derive the n, k, and σ values from a series of pseudo BRDF

measurements for various painted metal surfaces. Unfortunately, using an empirical method to derive the model parameters severely limits the ability to extrapolate the model beyond the measured domain.

7.4 Degree of Linear Polarization Characterization

The previous section characterized the Torrance-Sparrow BRDF model. In this section, we use the Torrance-Sparrow model to characterize the polarization behavior of aluminum. For the purposes of this characterization, the incident light was limited to totally unpolarized light. This allows us to see how much polarization can be introduced by a single reflection from a metallic facet. The simulation was performed by computing the BRDF Mueller matrix for a range of incident and reflected angles in the plane of incidence (i.e. $\Delta\phi = 180^\circ$). The incident light was unpolarized, $S_1 = S_2 = S_3 = 0$; therefore, the Stokes vector of the reflected light is simply a scaled version of the first column of the BRDF Mueller matrix:

$$a \begin{pmatrix} m_{00} \\ m_{10} \\ m_{20} \\ m_{30} \end{pmatrix} = \begin{pmatrix} m_{00} & m_{01} & m_{02} & m_{03} \\ m_{10} & m_{11} & m_{12} & m_{13} \\ m_{20} & m_{21} & m_{22} & m_{23} \\ m_{30} & m_{31} & m_{32} & m_{33} \end{pmatrix} \begin{pmatrix} a \\ 0 \\ 0 \\ 0 \end{pmatrix} \tag{7.17}$$

The degree of linear polarization calculation then becomes

$$\text{DoLP} = \frac{\sqrt{m_{10}^2 + m_{20}^2}}{m_{00}} \tag{7.18}$$

Figure 7.10 shows how the DoLP varies as a function of the incident and reflected zenith angles in the plane of incidence. The simulation was performed at a wavelength of 650 nm and a surface roughness of $\sigma = 0.2$. Reflections close to normal incidence produce the strongest polarization at a view angle between 60° and 70°.

As the incident angle increases, so does the DoLP and the peak between 60° and 70° disappears.

The out-of-plane behavior of the DoLP is shown in figure 7.11. For the case of near normal incidence, figure 7.11(a), the DoLP exhibits the same trend as the in-plane case over the entire range of azimuth angles. Once again, all of the DoLP values peak around a reflected angle of 60°. Figure 7.11(b) shows that for large incident angles, the DoLP continues to increase with increasing reflected angles. In addition, figure 7.11 shows that the lobe around the forward scattering region becomes narrower as the reflected angle approaches grazing incidence.

Due to reciprocity, the incident and reflected angles can be interchanged and still get the same BRDF. Therefore, all of the simulations in this section apply equally well when the sensor and illumination are interchanged.

7.5 Illumination Sampling Characterization

Synthetic image generation always involves a trade off between computation time and accuracy. Better accuracy typically involves increased computation time. The total number of rays shot is one of the biggest factors controlling the balance between accuracy and computation time. Shooting more rays results in a finer sampling of the illumination field. Finding a good balance between accuracy and computation time is not always an easy task. The following sections present data collected to assist in determining the appropriate number of rays needed for a chosen level of accuracy. The desired level of accuracy is often dictated by the intended use of the synthetic imagery.

Due to a lack of measured data for comparison, the following sections do not directly address the issue of accuracy. Instead, they asses how quickly the DIRSIG

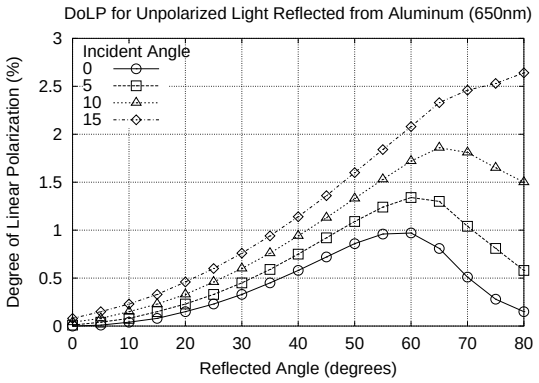

(a) Small incident zenith angles

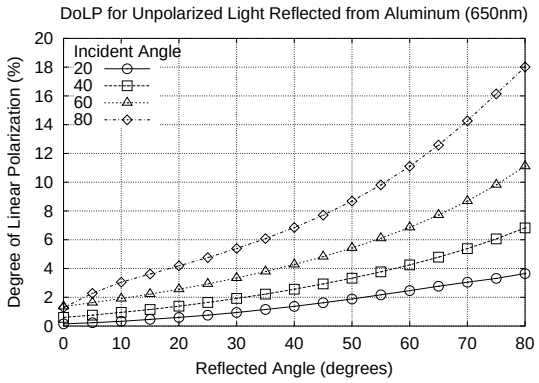

(b) Large incident zenith angles

Figure 7.10: Predictions of in-plane DoLP for unpolarized light reflected by aluminum with surface roughness $\sigma = 0.2$ rad.

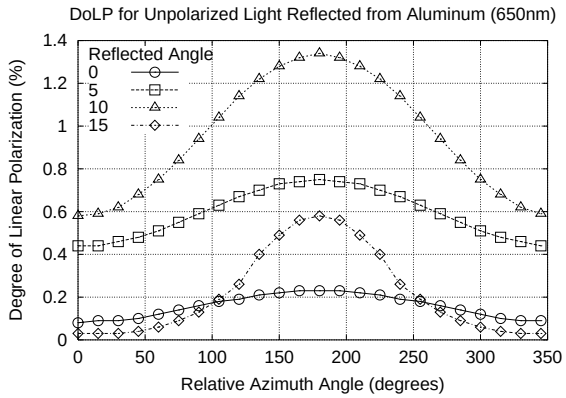

(a) Incident zenith angle of 5°.

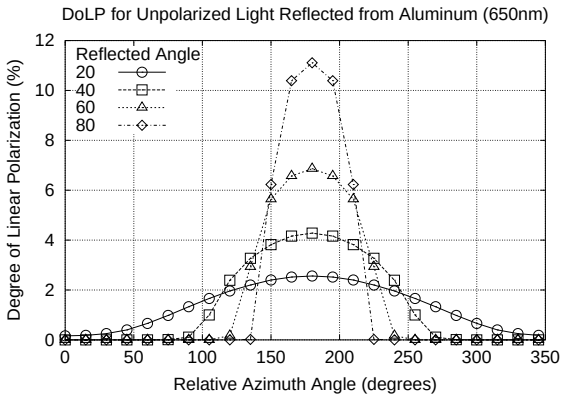

(b) Incident zenith angle of 60°.

Figure 7.11: Predictions of out-of-plane DoLP for unpolarized light reflected by aluminum with surface roughness $\sigma = 0.2$ rad.

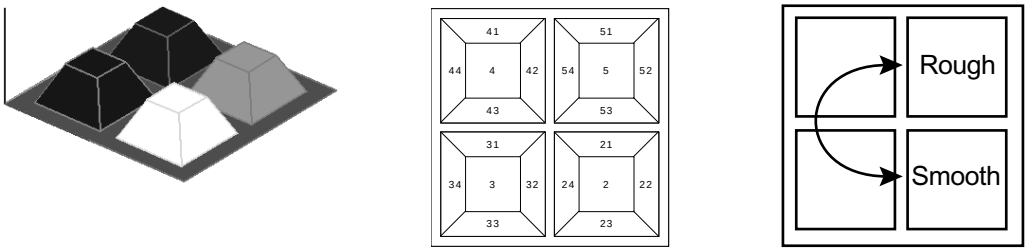

(a) Chunky bar geometry (b) Facet ID numbers (c) Facet Roughness

Figure 7.12: Diagram of the chunky bar scenes used for model validation.

simulations converge as a function of the total number of rays shot. The task of determining absolute accuracy is a candidate for further study.

The convergence tests used a simple geometry scene known as the "chunky bar" scene (see figure 7.12). The chunky bar scene provides a relatively simple geometry which includes some easy to understand multiple bounce cases. In addition, the flat tops of the chunks provide a region which only experiences direct illumination and no multiple bounces. Therefore, a single scene can be used to evaluate single and multiple interactions in a single simulation. The four chunks also provide an opportunity to compare up to four different materials side-by-side. The diagram in figure 7.12(b) shows the facet ID numbers associated with each facet in the scene. These ID numbers are used to describe phenomena observed on the various facets.

7.5.1 Random Sampling Issues

DIRSIG's ray tracer must decide how many rays to use for sampling the illumination field at each intersection. The unpolarized versions of DIRSIG shot more rays for the first intersected surface and fewer rays for the second surface and none after that.

This was based on the assumption that most of the illumination for a facet comes from direct illumination instead of reflected light. To fully model potential polarization effects, a minimum of two bounces are required and possibly more. Therefore, it is necessary to determine how to best distribute the total number of rays to be shot between the first intersection and subsequent intersections.

Once the number of rays has been determined, the next step requires distributing those rays over the hemisphere. Several issues arise during this step. Ideally, the sampling would be random and weighted by the BRDF and background illumination field. Care must be taken to ensure that adequate sampling of all relevant light sources occurs. As you begin to consider all of the factors, the sampling task quickly becomes extremely complex. A uniform sampling technique is relatively simple to implement. However, it can also introduce significant patterned artifacts in the scene. This is most significant in the shadow regions where the shadow become unrealistically harsh as an entire row of pixels becomes shadowed simultaneously due to course sampling.

The problem associated with uniform sampling leads to the solution of using random sampling. The first problem with this approach is the issue of double sampling bright sources like the sun. The effects of this are shown later as artificial "hot spots" in the images. We tried a couple of different random sampling schemes with varying levels of success. The first scheme resulted from a programming bug which produced rather interesting results. The random number generator was being reseeded with the same seed at the beginning of the calculations for each pixel in the scene. This was done in an attempt to use the same set of initial rays as we varied the number of rays shot. This way the simulations with more rays used the same rays as before but added more rays. While this approach produced very smooth images, there were significant variations between simulations as a function of the number of rays being cast. Initially,

this was assumed to be a convergence issue. However, additional testing indicated that was not the case. The problem was that when one pixel happened to shoot a ray towards a bright source, all of its neighboring rays also hit that same source. Therefore, the overall brightness level increased for the entire region artificially.

The next step was to seed the random number generator only once at the very beginning of the simulation. This ensured that neighboring pixels used a totally different set of rays. As a result, the large fluctuations between runs was eliminated. The consequence was increased "noisiness" of the images as some pixels became artificially too "hot". This was a surprising result since the simulations were initially being performed using all Lambertian materials and a totally uniform illumination field. Initially it appeared that there could be no source for the fluctuations. However, a careful analysis of the radiometry identified the problem. The solid angle associated with each ray was assumed to be the same for each of the random rays. This greatly simplified the solid angle computation by simply dividing the hemisphere's 2π steradians by the total number of rays. In actuality, the sun's ray was calculated separately from all of the rest so that it wouldn't be artificially increased when small numbers of rays were cast. The problem is that the solid angle of each ray is a function of the ray's zenith angle. By assuming all of the rays have the same solid angle, variations are introduced by the cosine term in the radiometry integral. In essence, by not carefully calculating the solid angle for each ray, the DHR was being allowed to fluctuate as a function of exactly where the rays were cast.

One way of reducing this error is to calculate the actual solid angle associated with each ray. Once all of the rays have been cast, all of the solid angles are summed and normalized to the full 2π steradians. The normalization process adds a significant number of calculations and similar results may be achieved by a better, more efficient

sampling method than a totally random approach.

The simple solution implemented for this analysis was to use a uniform grid sampling with a random azimuth offset for each pixel. This approach eliminated the DHR calculation errors by allowing a simple solid angle calculation for each of the rays while reducing the effects of using a uniform gird sampling scheme. The results using this approach still have some fluctuations from pixel to pixel, but they are much lower and decrease more quickly as the number of rays increases.

7.5.2 First Surface Sampling

This section presents data which characterize how quickly DIRSIG converges on a solution when only one bounce is involved. The tops of the chunky bars present an excellent test case because the facets receive only direct illumination. Several simulations were run where the total number of rays shot were varied. The first set used an all Lambertian chunky bar scene with different levels of reflectance for two pairs of the chunky bars. A uniform unpolarized sky was used as the illumination field. This represents the simplest scenario for interactions between the BRDF and the illumination field. In this case, both quantities are uniform over the entire range of azimuth and zenith angles. The only exception is the presence of solar illumination at a specific azimuth and zenith. In each run, the first ray samples the solar illumination and any and all subsequent rays sample the sky dome.

For this set of simulations, the spatial sampling used a uniform grid which was randomly rotated in azimuth for each pixel. Therefore, each pixel has the same relative azimuth and zenith sampling but different absolute sampling in the overall scene reference frame. This approach reduces the DHR error variation from pixel to pixel while avoiding some artifacts associated with using a purely uniform sampling grid.

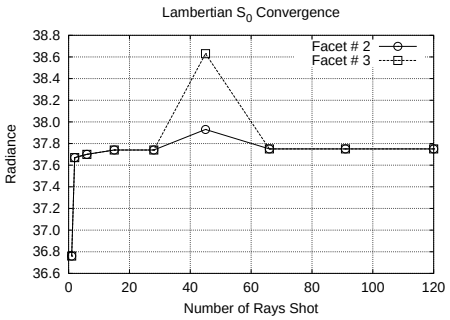

(a) Tops of Lambertian chunks

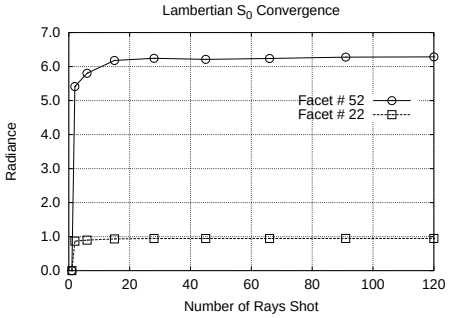

(b) Sides of Lambertian chunks

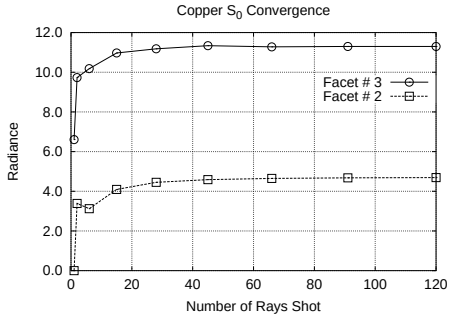

(c) Tops of Copper chunks

Figure 7.13: Comparison of S_0 convergence for Lambertian and copper surfaces in a single bounce scenario.

The same random number seed was used at the beginning of each simulation. Therefore, runs with the same number of rays but different materials represent identical sampling points. This allows for better comparisons between scenes with different materials.

7.5.2.1 Single Bounce Convergence Data

Figure 7.13 shows how DIRSIG converges for a single bounce scenario as a function of rays shot. The values plotted are the average value of all the pixels associated with the indicated facet. All three convergence tests show a similar pattern. The results change rapidly below 20 rays. For S_0, the results appear to be relatively constant

above 20 rays. The peak at 45 rays (see figure 7.13(a)) is a result of "hot spots" on the tops of the chunks. This happens when a small number of pixels happen to sample the solar irradiance more than once. This issue is discussed in greater detail in the next section and was resolved by ensuring the sun was sampled only once per pixel.

7.5.2.2 Single Bounce Images

The images in figures 7.14 and 7.15 show the effects of increasing the number of rays used to sample the illumination field. As the number of rays increases, the subtle shadowing on the sides of the upper left pyramid become smoother and exhibit more shades of gray. While the gray scale of these images had to be significantly stretched (figure 7.15) to observe this effect for this set of simulations, this same affect will occur in higher contrast areas of more complex scenes involving significant amounts of multiple bounces.

Originally, white specs were present in images using 45 rays or more and were dubbed "hot spots". They were the result of randomly sampling the solar disk more than once. This phenomenon is more likely to occur as the number of rays increases. However, at the same time, as the number of rays increases, the influence of the "hot rays" decreases since the solid angle associated with the ray also decreases. As the number of rays increased, the number of "hot spots" also increased and and their relative brightnesses decreased. This problem was solved by ensuring only one ray was cast towards the solar disk. The first ray cast, was directed towards the solar disk. After that, each subsequent ray was tested to see if it fell within the width of the solar disk as reported by the atmospheric model. If a subsequent ray was directed at the sun, it was eliminated. Figure 7.16 shows a pair of images before and after the

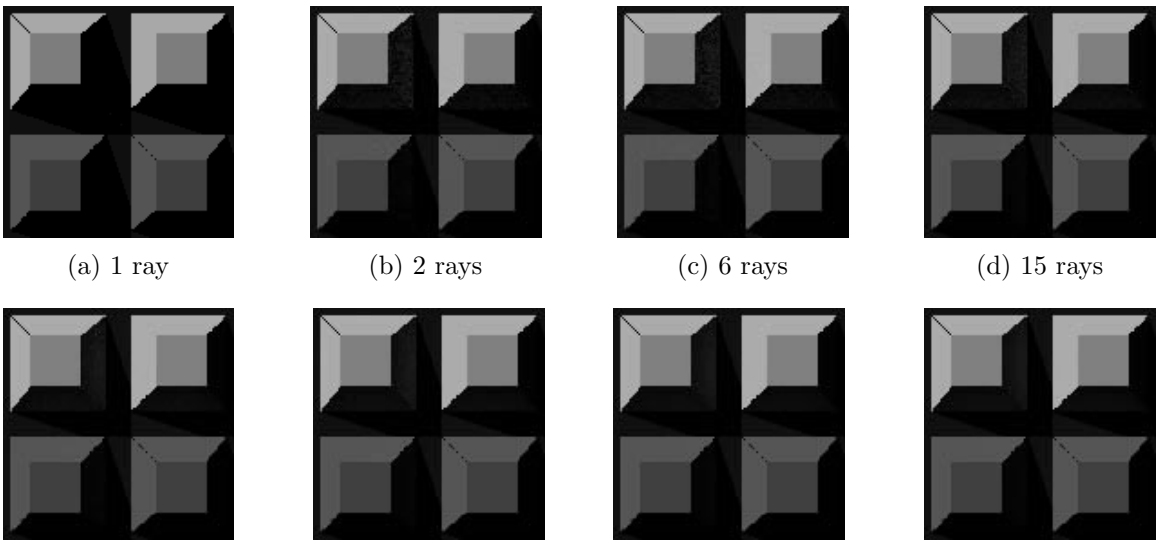

(a) 1 ray (b) 2 rays (c) 6 rays (d) 15 rays

(e) 28 rays (f) 45 rays (g) 66 rays (h) 91 rays

Figure 7.14: Effects of increasing the number of rays used to generate a synthetic image of an all Lambertian scene. All images have a common linear gray scale.

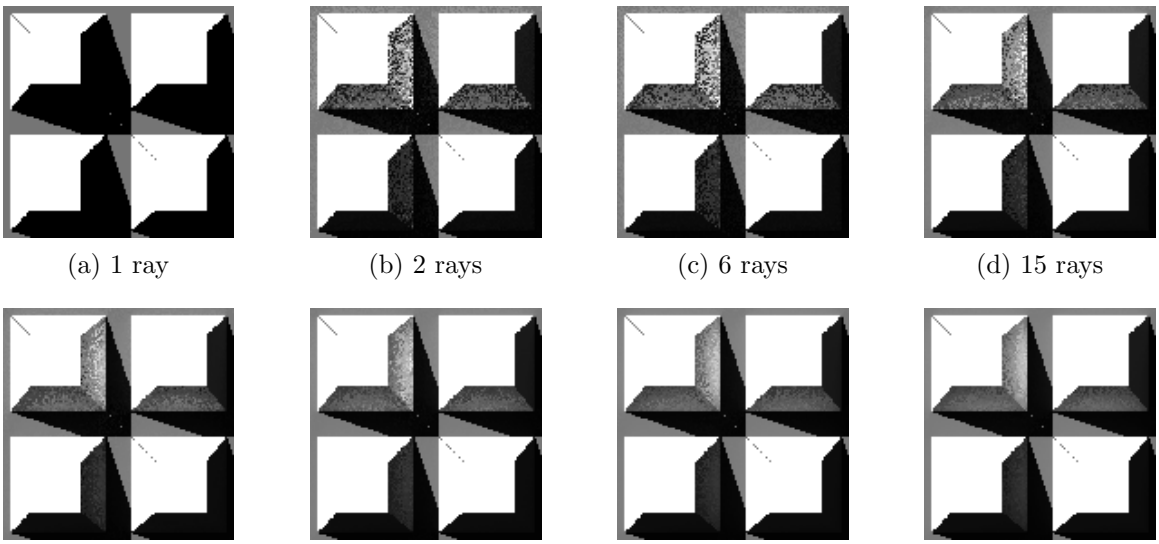

(a) 1 ray (b) 2 rays (c) 6 rays (d) 15 rays

(e) 28 rays (f) 45 rays (g) 66 rays (h) 91 rays

Figure 7.15: The same set of images from figure 7.14 stretched to show the variations in the dark shadow regions.

(a) Scene with hot spots

(b) Scene without hot spots

Figure 7.16: The hot spots present in the left image were eliminated by ensuring the solar disk was sampled only once per pixel.

hot spots were eliminated.

Preventing over sampling of the solar disk, while not trivial, is much simpler than the more general issue of preventing over sampling of multiple sources in a generic simulation. The best long term solution to this problem is to allow for multiple sampling of the sun and other sources while ensuring an appropriate solid angle is associated with any rays that intersect light sources. Finding an efficient method of sampling multiple sources is an area that requires additional research.

The same set of single bounce simulations were performed using four copper chunks. The surface roughnesses for each chunk is shown in table 7.5. The S_0 images

Facet ID	Sigma	Facet ID	Sigma
4	0.2	5	0.3
3	0.15	2	0.1

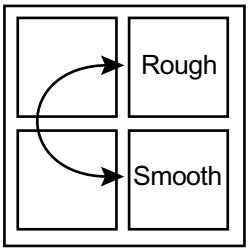

Table 7.5: Surface roughness for each chunk in the copper chunk scenes.

are shown in figures 7.17 and 7.18 and show trends similar to the Lambertian scene. The images clearly show that under sampling is more of a problem for specular materials. These images do contain any hot spots. The variations along the sides of the chunks is due to coarse sampling of highly specular materials. Ideally, the sampling would be weighted towards the specular lobe region instead of uniformly sampling the entire hemisphere.

The polarization images, S_1 through S_3, are shown in figures 7.19 through 7.21. The S_1 and S_2 images show the effects of variations caused by under sampling specular materials. As the number of rays increases, the speckling increases in quantity but decreases in magnitude. The increase in quantity is due to the increased number of samples allowing for a greater variance among the pixels. The decrease in relative magnitude is due to the averaging nature of increasing the number of samples. Other than that, there isn't much difference in these images. The S_3 images on the other hand, show how important it is to have the proper level of sampling in order to fully characterize the polarimetric signals. For this scenario, S_3 polarization only results from multiple bounces and therefore requires a significant number of rays to be cast.

Finally, the DoLP images are shown in figure 7.22. Clearly the DoLP image is highly influenced by the variations seen in all of the other images. This is to be expected since the DoLP is often a ratio of small numbers. Therefore, fluctuations in these small numbers greatly influences the DoLP image as seen.

7.5.2.3 Double Bounce Images

A second set of simulations was performed similar to the ones presented in the previous section. In this case, the number of rays cast from the first intersection was held constant at 120 and the number of rays cast from the second intersection

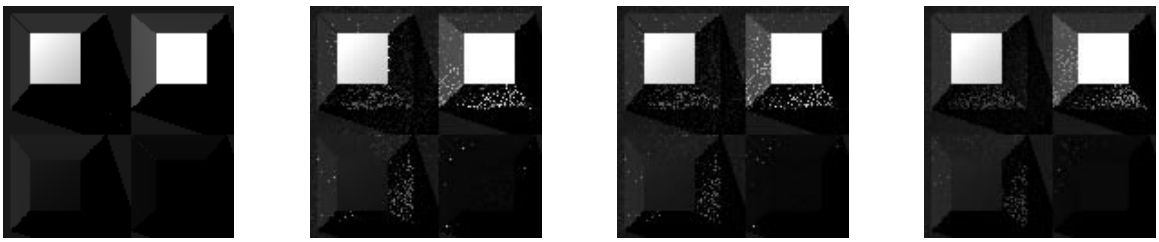

(a) 1 ray (b) 2 rays (c) 6 rays (d) 15 rays

(e) 28 rays (f) 45 rays (g) 66 rays (h) 91 rays

Figure 7.17: Effects of increasing the number of rays used to generate a synthetic image of a copper scene. All images have a common linear gray scale.

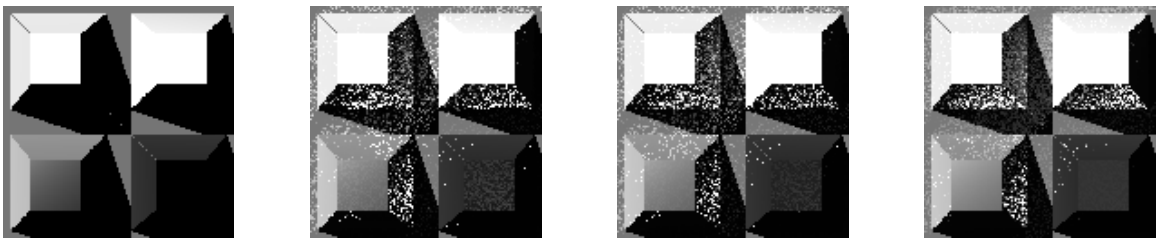

(a) 1 ray (b) 2 rays (c) 6 rays (d) 15 rays

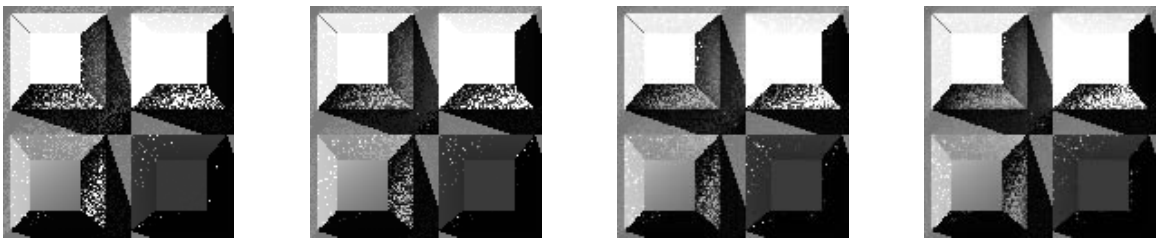

(e) 28 rays (f) 45 rays (g) 66 rays (h) 91 rays

Figure 7.18: The same set of images from figure 7.17 stretched to show the variations in the dark shadow regions.

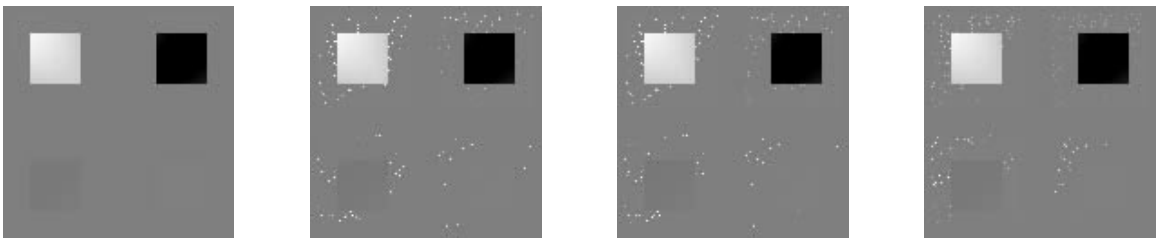

(a) 1 ray (b) 2 rays (c) 6 rays (d) 15 rays

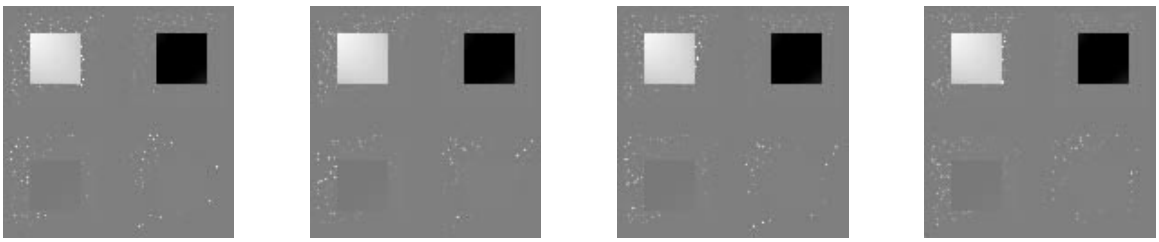

(e) 28 rays (f) 45 rays (g) 66 rays (h) 91 rays

Figure 7.19: Effects of increasing the number of rays used to generate a synthetic S_1 image of a copper scene. All images have a common linear gray scale.

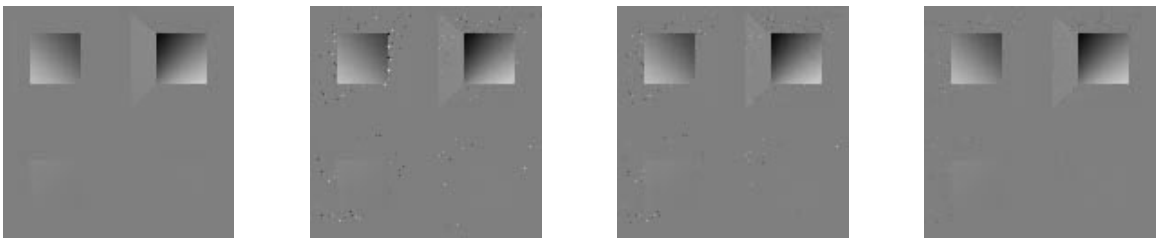

(a) 1 ray (b) 2 rays (c) 6 rays (d) 15 rays

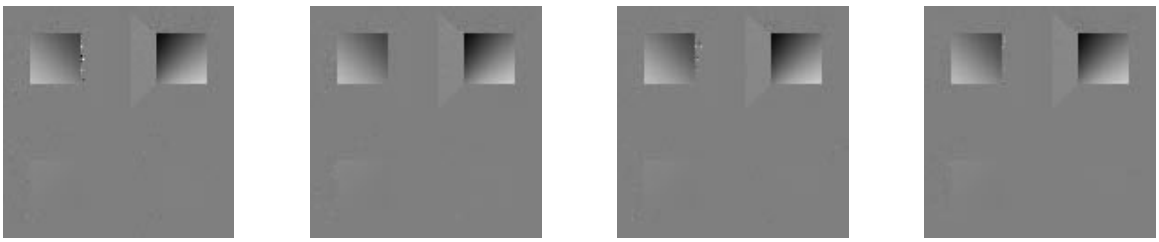

(e) 28 rays (f) 45 rays (g) 66 rays (h) 91 rays

Figure 7.20: Effects of increasing the number of rays used to generate a synthetic S_2 image of a copper scene. All images have a common linear gray scale.

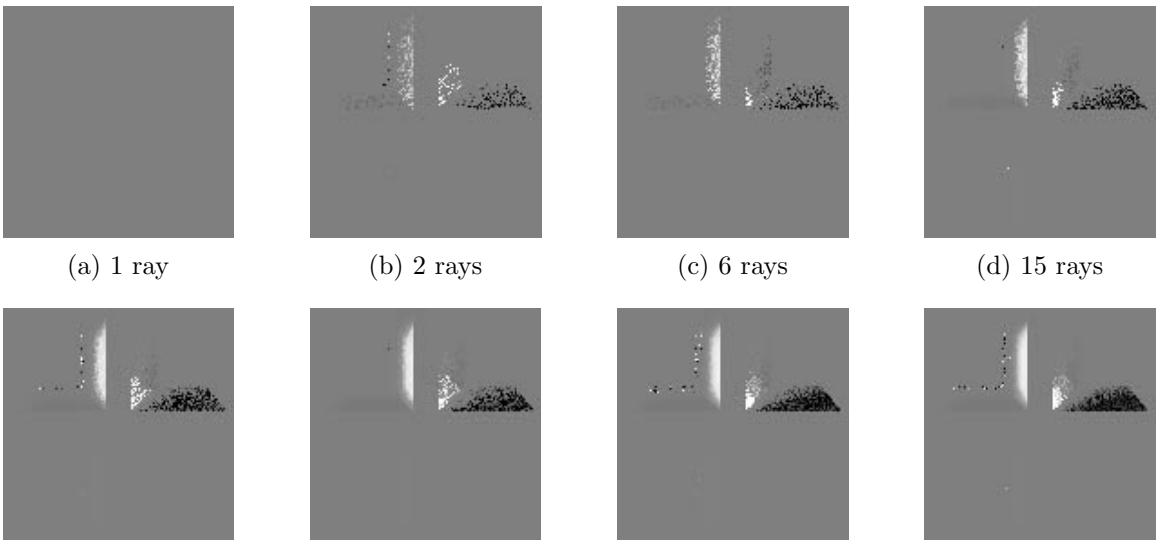

(a) 1 ray (b) 2 rays (c) 6 rays (d) 15 rays

(e) 28 rays (f) 45 rays (g) 66 rays (h) 91 rays

Figure 7.21: Effects of increasing the number of rays used to generate a synthetic S_3 image of a copper scene. All images have a common linear gray scale.

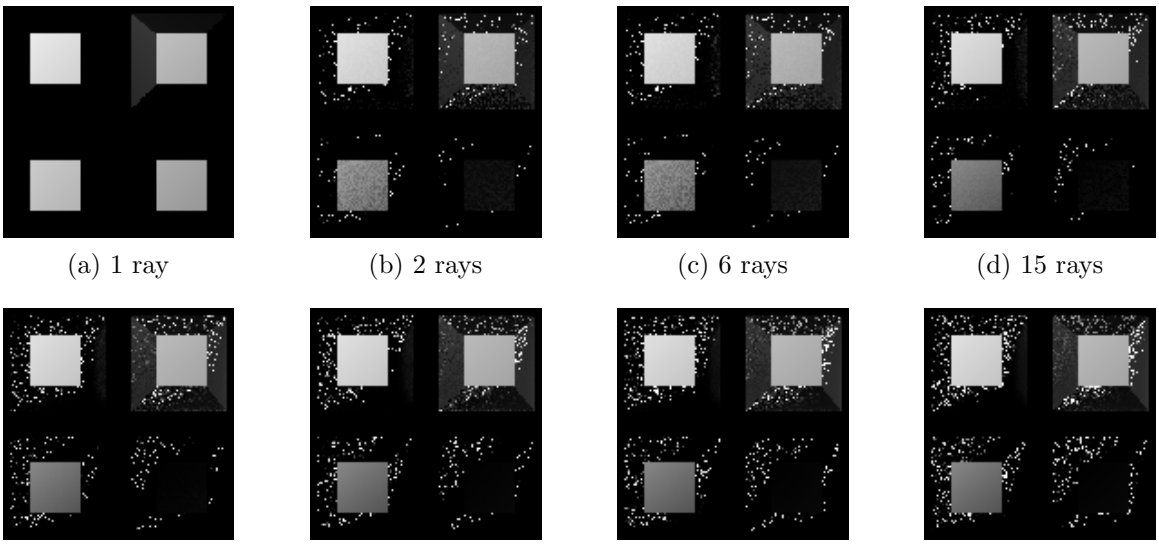

(a) 1 ray (b) 2 rays (c) 6 rays (d) 15 rays

(e) 28 rays (f) 45 rays (g) 66 rays (h) 91 rays

Figure 7.22: Effects of increasing the number of rays used to generate a synthetic DoLP image of a copper scene. All images have a common linear gray scale.

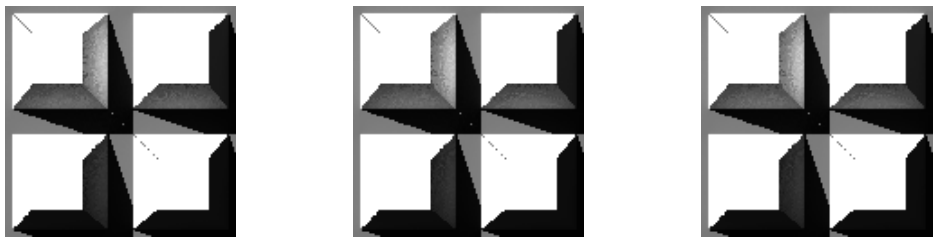

(a) 1 ray (b) 2 rays (c) 6 rays

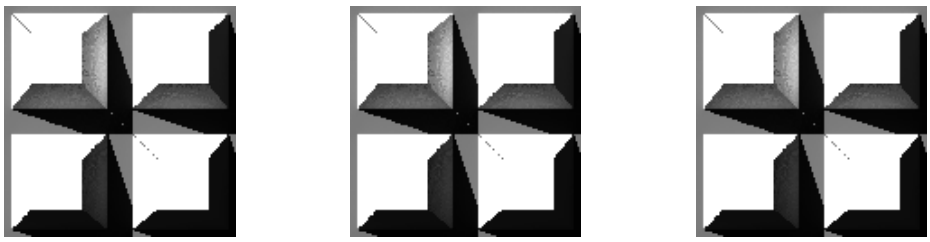

(d) 15 rays (e) 28 rays (f) 45 rays

Figure 7.23: Effects of increasing the number of rays on the second bounce for an all Lambertian scene. All images have a common linear gray scale.

(a) 1 ray (b) 2 rays (c) 6 rays

(d) 15 rays (e) 28 rays (f) 45 rays

Figure 7.24: Effects of increasing the number of rays on the second bounce for a copper scene. All images have a common linear gray scale.

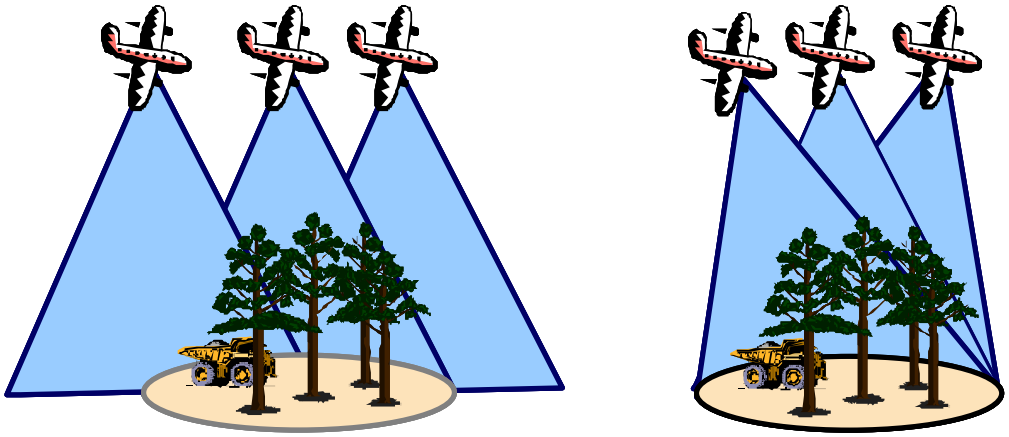

(a) Nadir looking flight profile

(b) Staring flight profile

Figure 7.25: Flight profiles used to demonstrate sensor module.

was varied. The results of this second set of simulations is shown in figures 7.23 and 7.24. Only the stretched S_0 images are presented. There was very little difference between these sets of images. This may be due to the large number of rays cast for the first surface. Varying the number of rays cast on the first and second bounce simultaneously might identify a better way to cast a total given number of rays. The computation time for these simulations were approximately an order of magnitude longer than the related single bounce simulation.

7.6 Sensor Simulations

This section presents the results of the sensor simulations performed. The new DIRSIG sensor module was not available for testing. Therefore, the sensor simulations were limited to a simple framing array system flown along two different profiles. The first flight profile was straight and level over the scene with a fixed camera pointing straight down. A sequence of nine images were formed representing the

camera capturing nine different images as it flew over the scene. The second flight profile flew over the same scene. However, this time, the angle of the camera was adjusted each time so that it remained pointed at the center of the scene. For this flight profile a sequence of five images were formed. Figure 7.25 depicts the two flight profiles used to demonstrate the capabilities of the sensor module and the resulting polarimetric response. The nadir looking profile demonstrates the ability to move the sensor along a flight profile while keeping the relative position of the sensor fixed. The staring profile demonstrates the ability to move both the platform and sensor simultaneously.

The copper scene was used to show how the S_0 brightness levels change as the camera flies in and out of the specular lobes. In addition, the copper scene also demonstrates how the polarization signatures change as the sensor moves along its flight path. The variations in view and illumination angles result in variations in the polarimetric signatures. All simulations were performed by casting a total of 91 rays.

7.6.1 Fixed Camera Straight and Level Flight Simulation

In the first flight profile, the sensor platform flew straight and level over the scene. The sensor was held stationary pointing straight down along the nadir direction. This is analogous to the simulations used to test the sampling requirements.

The S_0 images are shown in figure 7.26. The images are in sequence going across the rows and then down the page. The upper left chunk, facet ID 4, clearly demonstrates the effects of moving in and out of the specular lobe region. As the sensor's field of view enters the specular lobe region, the facet's relative brightness increases. This sequence of images also shows that the speckling moves around the image from frame to frame. This emphasizes the fact that this is a ray sampling phenomena.

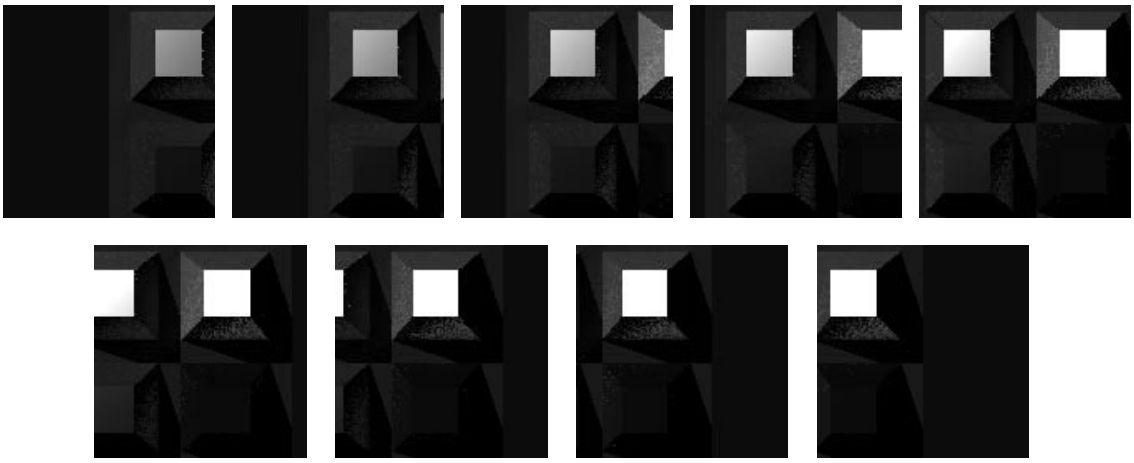

Figure 7.26: Simulated S_0 images from a fixed camera flying sensor.

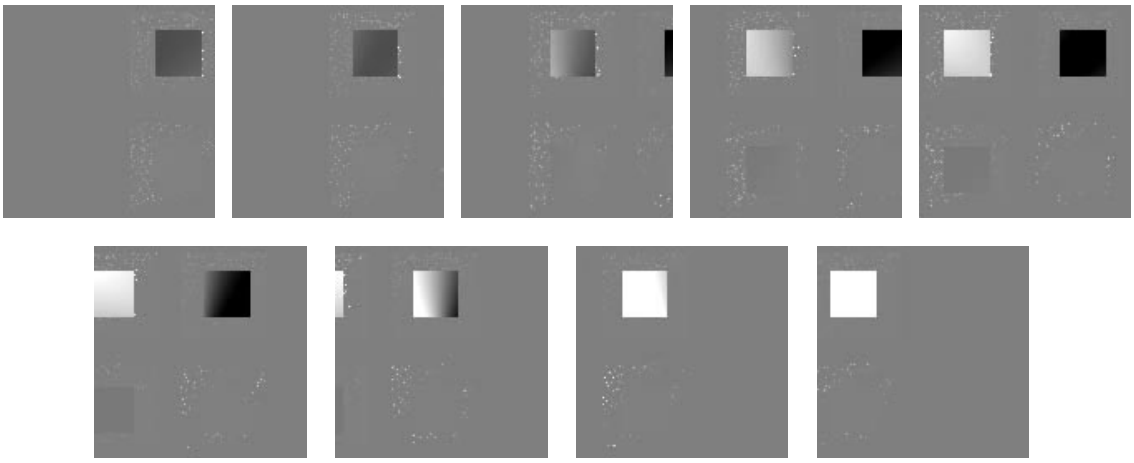

Figure 7.27: Simulated S_1 images from a fixed camera flying sensor.

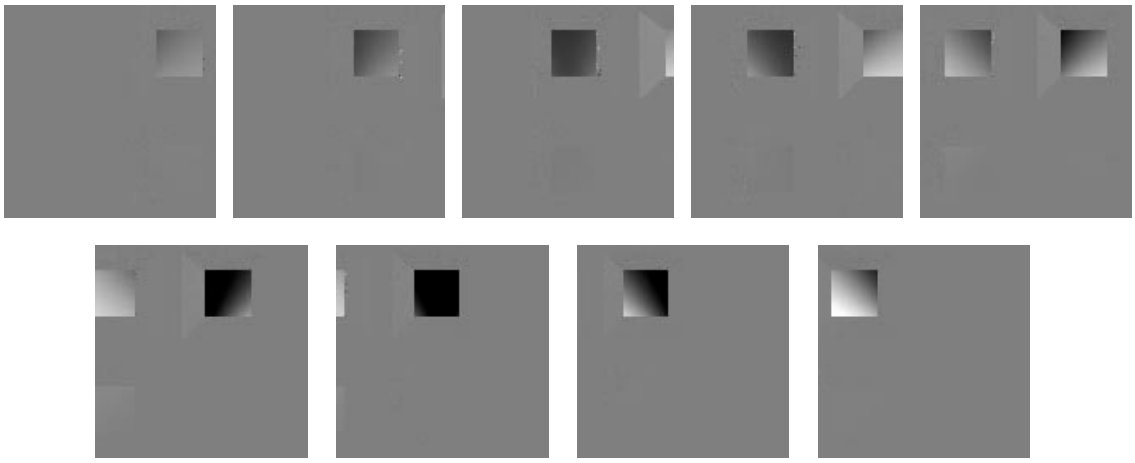

Figure 7.28: Simulated S_2 images from a fixed camera flying sensor.

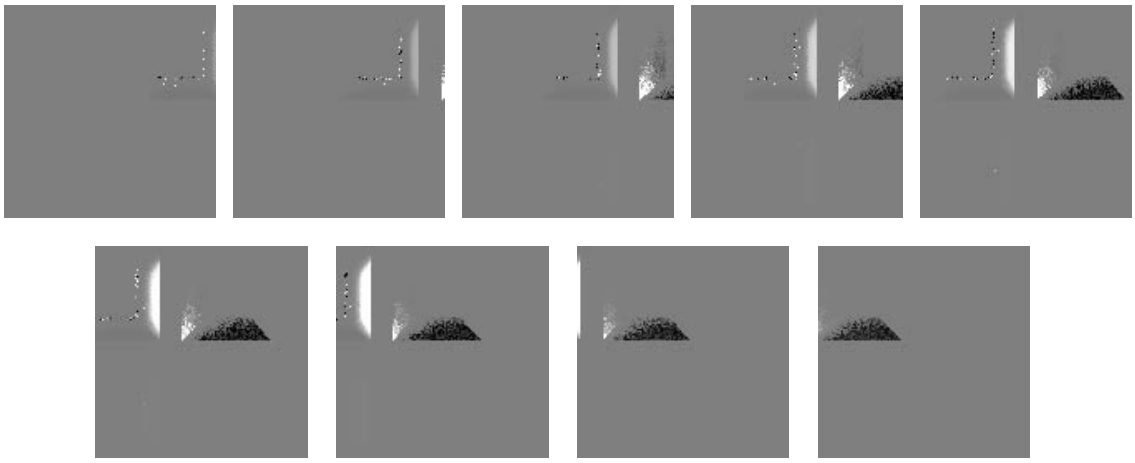

Figure 7.29: Simulated S_3 images from a fixed camera flying sensor.

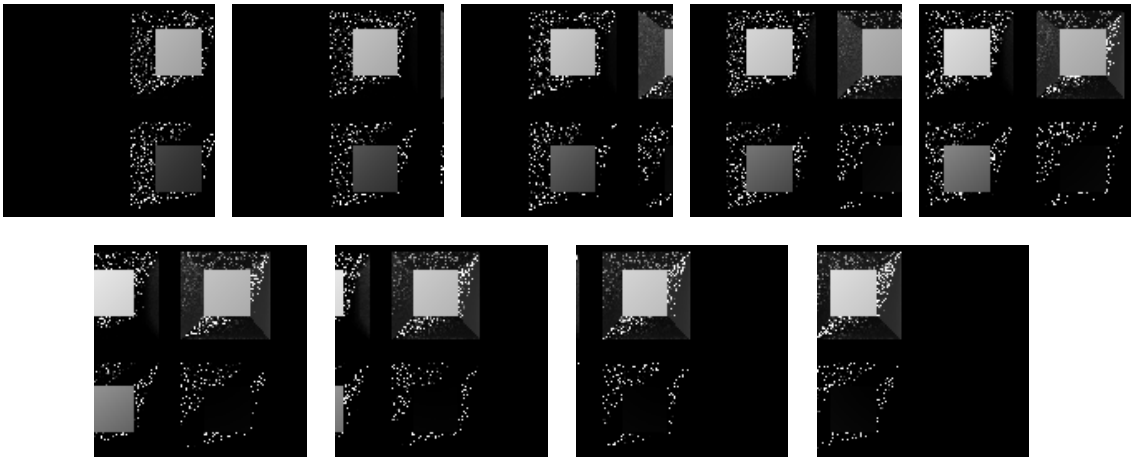

Figure 7.30: Simulated DoLP images from a fixed camera flying sensor.

The S_1 and S_2 images, figures 7.27 and 7.28 respectively, show how the linear polarization images change as the angle between the sensor's field of view and the sun change. Figure 7.29 shows that the circular polarization only changes slightly as the camera flies over head. Finally, the DoLP images, figure 7.30, have only slight variation in the tops of the chunks.

7.6.2 Staring Camera Flight Simulation

The second sensor simulation used the same framing array sensor but had it stare at the center of the scene as the sensor platform flew over the scene. The camera positions were the same as the previous simulation. However, the orientation at each position points the camera at the center of the scene and rotated clockwise about the optical axis. The images in this section clearly show a strong dependence on the sensor's viewing geometry.

The S_0 through S_3 images are shown in figures 7.31 through 7.34. Once again, the effects of moving in and out of the specular lobes is seen in these images. The

Figure 7.31: Simulated S_0 images from a staring camera flying sensor.

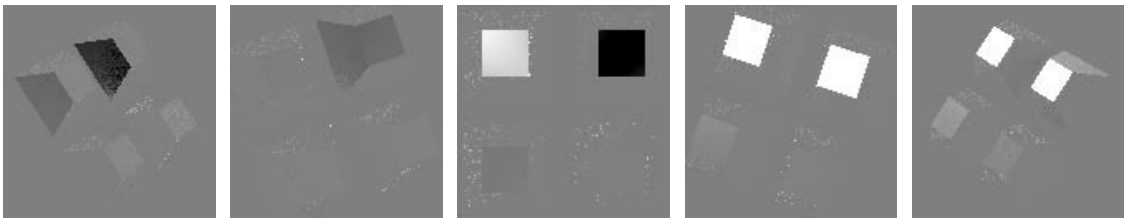

Figure 7.32: Simulated S_1 images from a staring camera flying sensor.

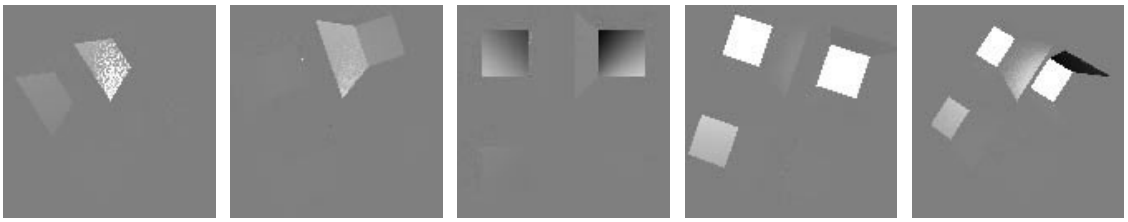

Figure 7.33: Simulated S_2 images from a staring camera flying sensor.

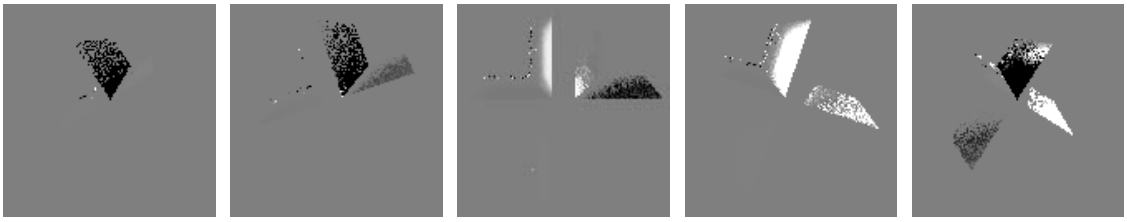

Figure 7.34: Simulated S_3 images from a staring camera flying sensor.

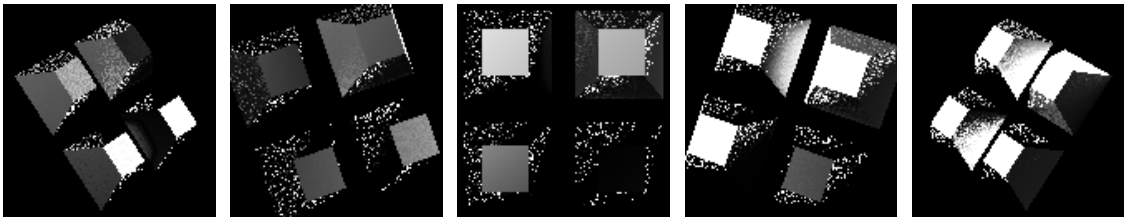

Figure 7.35: Simulated DoLP images from a staring camera flying sensor.

reflection of the neighboring chunk shows up nicely in the far right image of figure 7.31. A similar reflection is not seen in the lower pair of chunks because they are more specular than the upper pair and the sensor's field of view is too far away from the specular returns. Note that this same reflection is seen in the S_2 image, figure 7.33, but not the S_1 image, figure 7.32. The reflection appears earlier in the circular polarization, figure 7.32, than it does in the other images.

Finally, the DoLP images, figure 7.32, show a wide range of variations. The tops of the chunks tend to fluctuate as the sensor flies over head. The strongest DoLPs are seen where the zenith angles of the sensor are large. This agrees with the results obtained during the DoLP characterization. Once again, we see the effects of the "hot spots" is most significant in the DoLP images.

7.7 Polarized Atmosphere Scenes

All of the previous scenes used a simplified unpolarized atmosphere. In addition, the simulations were all performed using a single wavelength. This was done to minimize the number of variables and to reduce the time required to perform all of the simulations. This section presents the effects of using a polarized atmosphere. It should be noted that the polarized version of MODTRAN used is still in alpha testing. As such, no effort was made to judge the validity of the polarized signatures coming from the atmospheric model. Instead, the atmospheric model was used to generate a plausible input for a "typical" sky.

AFRL has been performing validation tests of the polarized version of MODTRAN. Their preliminary results indicate MODTRAN closely follows the trends of the atmospher's polarization signatures as demonstrated in figure 7.36. The MODTRAN predictions were for a sky with only Rayleigh scattering and no aerosols. The reference data was collected by Coulson (1988) at the Mauna Loa observatory in Hawaii. The data were collected at an altitude of 3.4 km, a wavelength of 700 nm, and the sky was very clear with few aerosols. MODTRAN slightly over estimates the polarization because it doesn't include the aerosol scatter which tends to depolarize the light.

The simulations were performed at two wavelengths, 450 nm and 650 nm, which lie at the two ends of the visible spectrum. These two wavelengths were chosen to note variations in polarization signature as a result of wavelength. Unfortunately, since the DIRSIG sensor platform module coding wasn't completed in time for these simulations, the sensor view angles were limited to direct over head viewing. This is not an optimum viewing geometry for detecting polarization signatures. However,

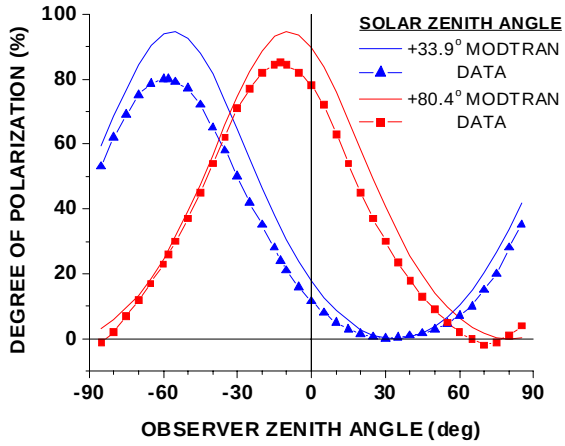

Data location: Mauna Loa, Hawaii
Alt: 3.4 km
$\lambda = 700$ nm
Sky conditions: Clear sky, few aerosols
(Plot courtesy of AFRL)

Figure 7.36: Comparison of MODTRAN-P and Coulson sky data at 700 nm. The MODTRAN atmosphere used Raleigh scattering without aerosols.

the results do show some variations due to wavelength. The sun was placed at a zenith angle of 20.67° and an azimuth of 175.66°.

The first thing to note is that illumination and reflection levels vary as a function of the wavelength. Both pairs of S_0 images in figure 7.37 used the same linear stretches. Therefore, direct comparisons can be made between the gray levels seen in those images. The brightness difference is most notable in the most diffuse chunk, upper left corner. However, the trend is seen in all four chunks when viewed in the stretched images. The side reflections in the top two chunks also demonstrate this variation nicely.

The DoLP images in figure 7.37 could not be stretched using the same scale without one image being saturated. The 650 nm DoLP image had to be stretch an order of magnitude more than the 450 nm image. The DoLP values in the 450 nm images vary between 0% and about 4% while the DoLP values in the 650 nm image only range between 0% and about 0.5%. The variations between the S_0 and DoLP differences can be attributed to a combination of varying sky polarization and

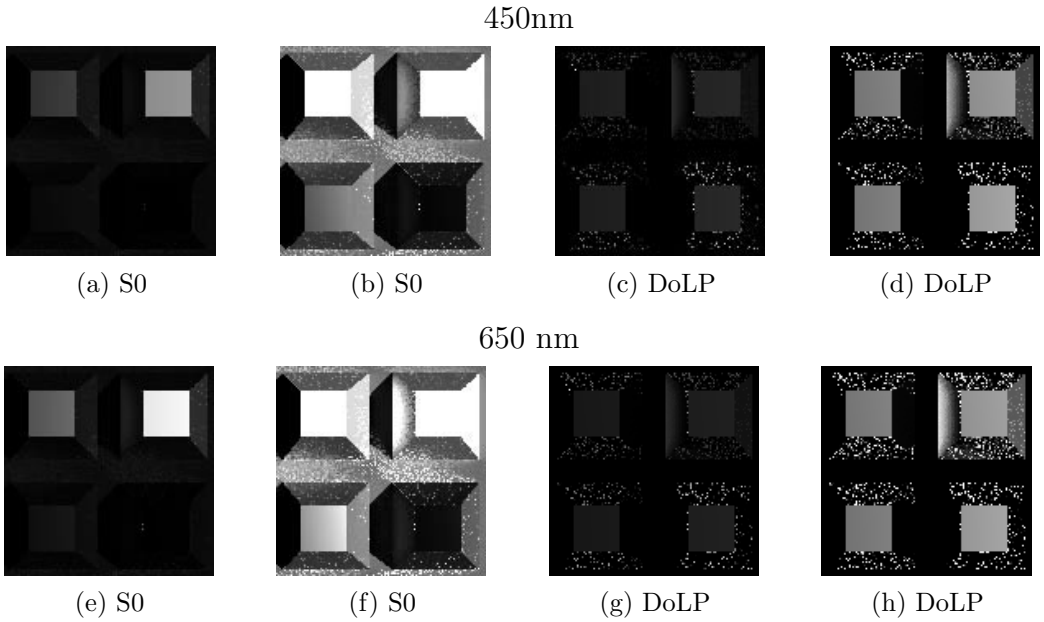

(a) S0 (b) S0 (c) DoLP (d) DoLP

(e) S0 (f) S0 (g) DoLP (h) DoLP

Figure 7.37: S_0 and DoLP images for the polarized atmosphere simulation using the copper chunky bar scene. The right image of each pair has been stretched.

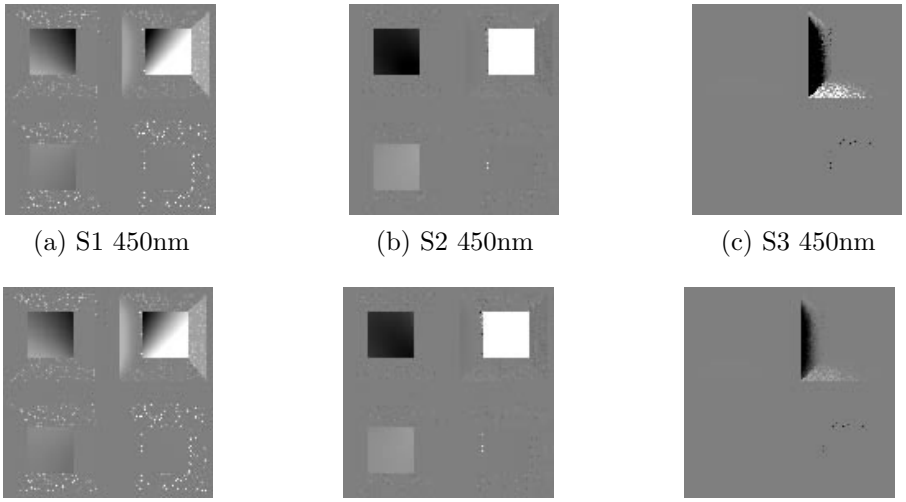

(a) S1 450nm (b) S2 450nm (c) S3 450nm

(d) S1 650nm (e) S2 650nm (f) S3 650nm

Figure 7.38: Polarization images (S_1 through S_3) for the polarized atmosphere simulation using the copper chunky bar scene.

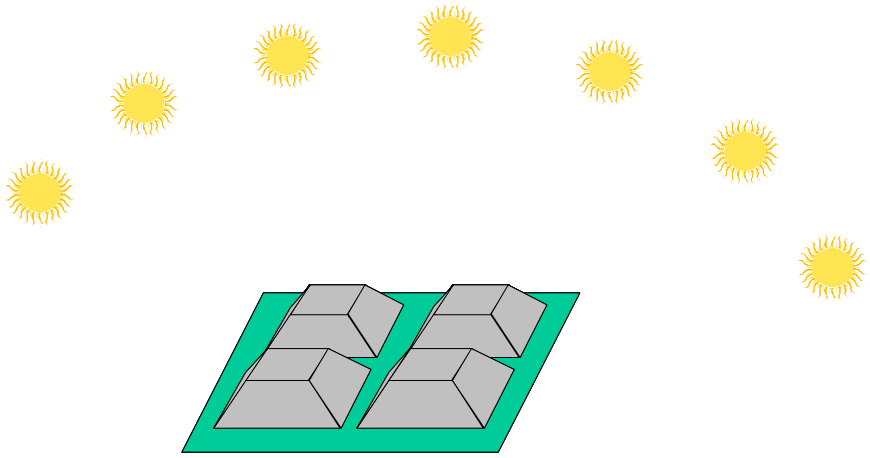

Figure 7.39: Cartoon drawing of the time-of-day simulations.

reflectances as a function of wavelength.

7.8 Time of Day Scenes

A set of simulations was performed using the simple atmosphere which simulated a sensor staring at a scene from overhead throughout an entire day. Images of the scene were generated for every hour starting at 7:00 am and ending at 6:00 pm. The sun's position in the sky was calculated based on the scene being located in Rochester, NY. Figure 7.39 depicts how these images were simulated.

The results are shown in figures 7.40 through 7.44. As in the previous sensor simulations, these images show strong polarimetric variations as a function of geometry. In the sensor simulations, the view angle was changing. In these simulations, the illumination angle was changing. Both types of geometry variations produce significant changes in the observed polarization signatures. These results also show the relative behavior of specular and diffuse materials over a wide range of illumination

angles. The chunk in the lower right corner of the scene is the most specular and shows the greatest variation in reflectance as the sun passes over. The more diffuse chunks exhibit less of a variation and reflect light over a larger range of time. In the DoLP images, this trend is reversed.

7.9 Summary

A series of tests and simulations were performed to test and characterize the integration of the new polarimetric capabilities. The polarimetric radiance equations were tested using a series of DIRSIG flat panel simulations along with hand calculations. The differences resulting from the new polarized equations were compared to the unpolarized equations. The results show differences in the 1% to 10% range depending upon the amount of polarization present in the illumination and the polarization sensitivity of the detector. In general, the unpolarized calculations under predicted the total sensor reaching radiance since it averages the polarimetric response. The polarized calculations fully account for the polarization interactions and more accurately predict the total sensor reaching radiance.

DIRSIG's implementation of the Torrance-Sparrow BRDF was compared to Fresnel reflection theory for smooth surfaces and the result published by Priest and Germer. In both cases, the DIRSIG results closely tracked the comparison data. Once the Torrance-Sparrow BRDF implementation was verified, a series of tests were performed to characterize the models response to changes in the three input parameters.

Finally, the entire integrated DIRSIG simulation tool was tested with a simple geometric scene. The scene was designed to test both single and multiple bounce scenarios in an easy to understand geometry. The results show a strong dependence on the amount and method of sampling used to determine the incident irradiance.

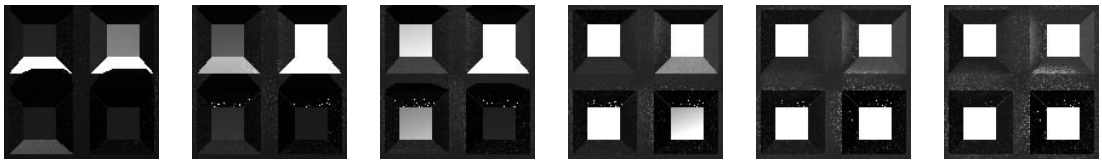

(a) 0700 (b) 0800 (c) 0900 (d) 1000 (e) 1100 (f) 1200

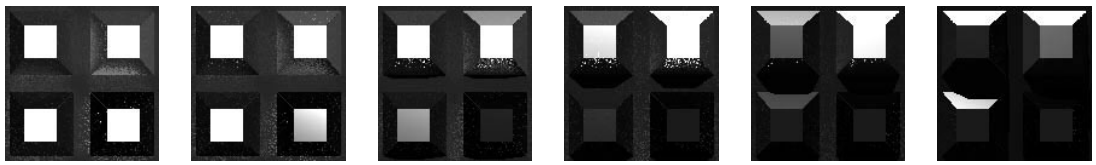

(g) 1300 (h) 1400 (i) 1500 (j) 1600 (k) 1700 (l) 1800

Figure 7.40: Hourly S_0 images for the copper scene using an unpolarized sky.

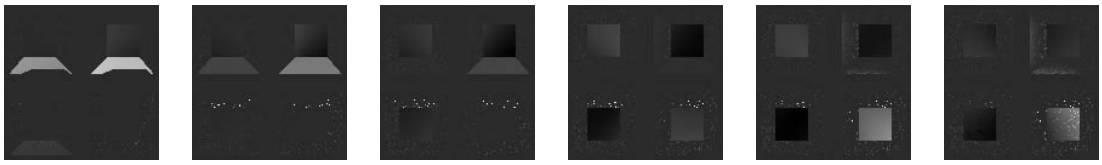

(a) 0700 (b) 0800 (c) 0900 (d) 1000 (e) 1100 (f) 1200

(g) 1300 (h) 1400 (i) 1500 (j) 1600 (k) 1700 (l) 1800

Figure 7.41: Hourly S_1 images for the copper scene using an unpolarized sky.

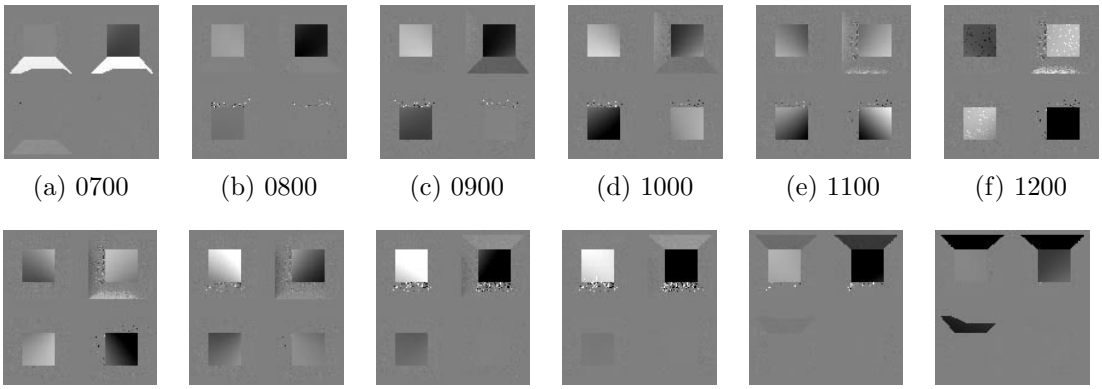

(a) 0700 (b) 0800 (c) 0900 (d) 1000 (e) 1100 (f) 1200

(g) 1300 (h) 1400 (i) 1500 (j) 1600 (k) 1700 (l) 1800

Figure 7.42: Hourly S_2 images for the copper scene using an unpolarized sky.

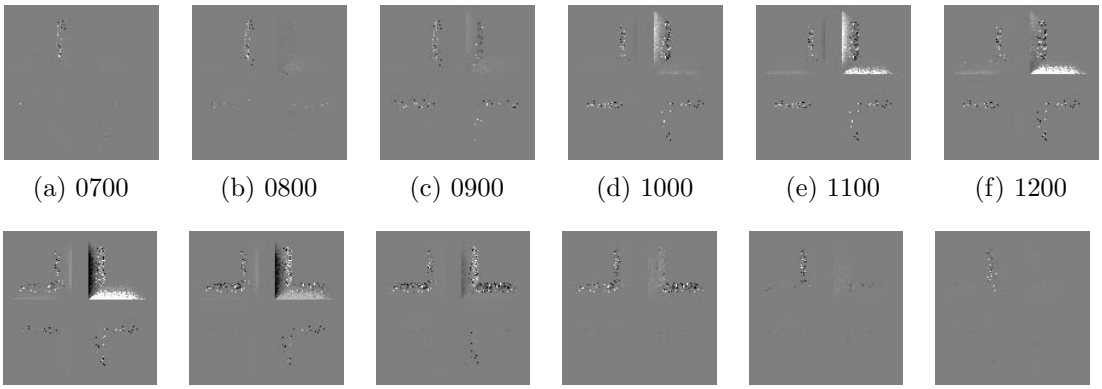

(a) 0700 (b) 0800 (c) 0900 (d) 1000 (e) 1100 (f) 1200

(g) 1300 (h) 1400 (i) 1500 (j) 1600 (k) 1700 (l) 1800

Figure 7.43: Hourly S_3 images for the copper scene using an unpolarized sky.

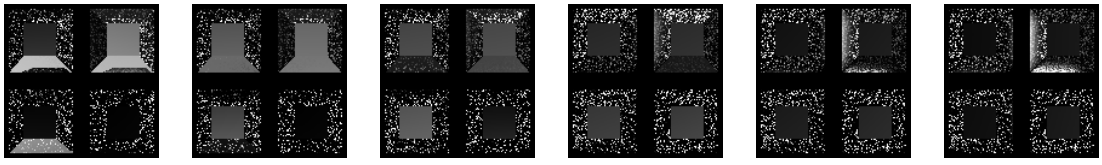

(a) 0700 (b) 0800 (c) 0900 (d) 1000 (e) 1100 (f) 1200

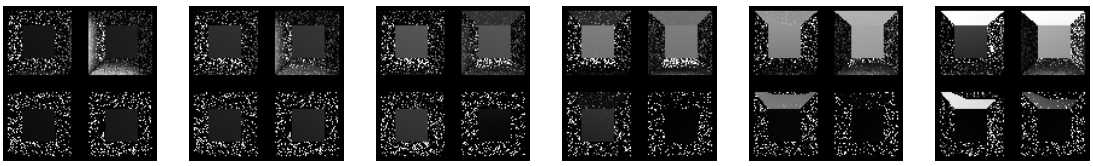

(g) 1300 (h) 1400 (i) 1500 (j) 1600 (k) 1700 (l) 1800

Figure 7.44: Hourly DoLP images for the copper scene using an unpolarized sky.

The results indicate a need to find an efficient method of randomly sampling the sky dome while not over sampling large irradiance sources like the sun. A series of simulations were performed to demonstrate the features of the sensor module and the ability to integrate a polarized atmospheric model.

Chapter 8

Conclusions

We have successfully demonstrated the ability to perform polarimetric radiometry simulations resulting in a synthetically generated sensor reaching radiance image. The radiative transfer calculations can be performed using either polarized or unpolarized quantities in the same simulation based on the availability of polarimetric input parameters. The resulting simulation includes as much polarization information as possible about the simulated scene.

The performance of the polarimetric BRDF models were tested as best as possible using the limited BRDF measurement tools available. Reasonable agreement was obtained for two metal samples using tabulated index of refraction values. Given the ability to better measure the optical parameters of a sample, the performance of the BRDF model should improve.

A lack of polarimetric BRDF databases poses the single largest problem for conducting fully polarimetric radiometry simulations. Physically based BRDF models exist that do an acceptable job of predicting the polarimetric BRDF. However, community wide resource limitations have prevented generating databases of physically

based model parameters. Empirically derived parameters tend to work well for specifically measured materials. However, the empirical method severely limits the ability to extrapolate the results to unknown conditions. As better models and material databases become available, the simulated results will also improve.

Several major accomplishments were achieved during the integration of the polarimetric calculations. First the ability to simultaneously perform polarized and unpolarized computations was developed without significantly impacting the computation time of the unpolarized simulations. A better method of handling BRDF models was developed for DIRSIG which allows for a smoother integration of future models and improvements of current models. A modified Torrance-Sparrow BRDF model was integrated and validated using a simple laboratory experiment. We also demonstrated the ability to use various atmospheric models with different levels of polarimetric and spectral complexity. The results confirm that even in the presence of a totally uniform unpolarized illumination field, the materials within a scene will generate varying polarization signatures. These signatures obviously change in the presence of polarized illumination.

The BRDF sampling and characterization were improved over earlier versions of DIRSIG. Three new BRDF sampling techniques were developed. Additional analysis needs to be performed in this area to better understand all of the interactions and factors. In addition analyzing the distribution of rays between the various bounces may lead to better performance for a given number of total rays used in a simulation.

Limited scene and sensor simulations were performed due to the current developmental status of the new version of DIRSIG. The results obtained for the simple scenes and sensors presented in this work should apply equally to more complex scenes and sensor designs. None of the simplifications used prevents the extrapolation of these

results to more complex scenarios typically performed using the full version of DIRSIG.

Several areas exist for continued research. Two of the biggest areas include better polarimetric BRDF measurements and characterization and improved models. As the polarimetric BRDF of various materials is characterized, our understanding of the physics involved will improve leading to better first principles based BRDF models. Until then, we will have to use a mixture of analytical and empirically based models.

The usefulness of the Torrance-Sparrow BRDF model is limited by our knowledge of the complex index of refraction for the materials of interest. Therefore, it would be beneficial to investigate methods of either estimating or measuring the complex index of refraction for a given sample. The complex index of refraction is used by the model to calculate the complex Fresnel reflection amplitudes as a function of incident and reflected angles. Therefore, it might be possible to modify the model to accept measurements of the material's Fresnel reflectivities. A series of specular reflectivity measurements could be made using a field spectrometer like the ASD used in this research. The incident light would have to be depolarized and the spectrometer would need a rotatable linear polarizer. The polarizer would be used to measure the reflectivities parallel and orthogonal to the plane of incidence. These measurements would provide a spectral database of reflectivities that could be interpolated over the range of required specular angles. The depolarizing diffuse portion of the BRDF could be obtained from measurements using an integrating sphere. This measurement approach could be simulated using the current Torrance-Sparrow BRDF model to determine its potential. In such an experiment, the Torrance-Sparrow model would be used as a truth source and the measurements described would be simulated using the results of the Torrance-Sparrow model. The simulated experimental results could then be compared with the values directly obtained from the Torrance-Sparrow model. If

the experiment shows promise, the next step would involve designing and conducting real laboratory experiments.

If the surface roughness of the material is the dominant parameter affecting the specularity of the BRDF. If the surface roughness of a material is not well known, additional non-specular measurements would have to be made in the plane of incidence to estimate the size of the specular lobe. The specular lobe size could then be used to derive an estimate of the surface roughness parameter.

This research only focused on reflections in the visible region of the spectrum. Polarization effects are also present in the IR region and this presents another area for further development and research. Transmission effects across the entire spectrum is yet another area that needs more research. While there is very little information about polarimetric BRDFs, there is even less available for polarimetric transmissions. The basic mathematical tools have been developed as part of this effort which can be used to implement future transmission models for solid materials like leaves.

The various intricacies of performing computer simulations to generate synthetic imagery present a whole host of areas for continued research. As in the case of the background sampling, many aspects of the simulation problem appear simple on the surface but have unexpected complexities. An entire effort could be focused on better understanding the implications of assumptions used to sample the illumination field.

Finally, the modeling tools developed could be used to explore a wide variety of remote sensing schemes that implement polarimetric remote sensing. These studies could assess the impacts of sensor design trades. They could also look at methods to characterize and exploit the polarimetric information collected.

Works Cited

Berk, A., L. S. Bernstein, and D. C. Robertson. MODTRAN: A moderate resolution model for LOWTRAN 7. Technical Report GL-TR-89-0122, Spectral Sciences Inc., April 1989.

Brosseau, Christian. *Fundamentals of Polarized Light: A Statistical Optics Approach*. New York, NY: John Wiley & Sons, Inc., 1998.

Brown, Scott D. *DIRSIG User Documentation: Release 3.4*. Chester F. Carlson Center for Imaging Science, Rochester, NY: Rochester Institute of Technology, June 1, 2001.

Brown, Scott D., Rolando Raqueño, and John R. Schott. "Incorporation of Bi-Directional Reflectance Characteristics into the Digital Imaging and Remote Sensing Image Generation Model." *Proceedings of the Eighth Annual Ground Target Modeling and Validation Conference*. Houghton, MI: Michigan Technological University, August 1997.

Brown, Scott D., John R. Schott, Todd Kraska Rolando Raqueño, and Russ White. "Validation and Analysis of the Digital Imaging and Remote Sensing Laboratory's Synthetic Image Generation Model, DIRSIG." *Proceedings of the Seventh Annual Ground Target Modeling and Validation Conference*. Houghton, MI: Michigan Technological University, August 1996.

Collett, Edward. *Polarized Light*. New York, NY: Marcel Dekker, Inc., 1993.

Coulson, Kinsell L. *Polarization and Intensity of Light in the Atmosphere*. Hampton, Virginia: A. Deepak Publishing, 1988.

Coulson, Kinsell L., Jitendra V. Dave, and Zdenek Sekera. *Tables Related to Radiation Emerging from a Planetary Atmosphere with Rayleigh Scattering*. Berkeley, CA: University of California Press, 1960.

Deschamps, Pierre-Yves, François-Marie Bréon, Marc Leroy, Alain Podaire, Annick Bricaud, Jean-Claude Buriez, and Geneviève Sèze. "The POLDER Mission: Instrument Characteristics and Scientific Objectives." *IEEE Transactions on Geoscience and Remote Sensing* 32 (May 3, 1994): 598–615.

Egan, Walter G. *Photometry and Polarization in Remote Sensing*. New York, NY: Elsevier, 1985.

Egan, Walter G. "Polarization in Remote Sensing." *SPIE* 1747 (1992): 2–28.

Egan, Walter G., W. R. Johnson, and V. S. Whitehead. "Terrestrial polarization imagery obtained from the Space Shuttle: characterization and interpretation." *Applied and Optics* 30 (February 1, 1991): 435–442.

Ellis, Kenneth K. "Reflectance Phenomenology and Modeling Tutorial". World wide web hypertext document, ERIM Int., 1994, `<http://www.erim-int.com/on-line-docs/GUIDE/guide.frm.html>`.

Ellis, Kenneth K. "Polarimetric bidirectional reflectance distribution function of glossy coatings." *Journal of the Optical Society of America* 13 (August 1996): 1758–1762.

Ellis, Kenneth K., Frank N. Jones, Guobei Chu, and William F. Lynn. "First-Principles Coatings Reflectance Model Validation." *Proceedings of the*

Sixth Annual Ground Target Modeling and Validation Conference. Houghton, MI: Michigan Technological University, August 22–24, 1995.

Feng, Xiaofan, John R. Schott, and Timothy Gallagher. "Comparison of methods for generation of absolute reflectance-factor values for bidirectional reflectance-distribution function studies." *Applied and Optics* 32 (March 1, 1993): 1234–1242.

Flynn, David S. and Cliff Alexander. "Polarized surface scattering expressed in terms of a bidirectional reflectance distribution function matrix." *Optical Engineering* 34 (June 1995): 1646–1650.

Hecht, Eugene. *Optics*. Second edition. Reading, Massachusetts: Addison-Wesley Publishing Company, 1990.

Maxwell, J. R., J. Beard, S. Weiner, D. Ladd, and S. Ladd. Bidirectional Reflectance Model Validation and Utilization. Technical Report AFAL-TR-73-303, DTIC Accession #AD913816, Environmental Research Institute of Michigan, Ann Arbor, MI 48107, October 1973. Prepared for Air Force Avionics Laboratory, Air Force Systems Command, Wright-Patterson AFB, OH 45433.

Metzler, Michael. Re: NEF BRDF Calculations. July 5, 2001, e-mail conversation.

Nadal, Florence and François-Marie Bréon. "Parameterization of Surface Polarized Reflectance Derived from POLDER Spaceborne Measurements." *IEEE Transactions on Geoscience and Remote Sensing* 37 (May 3, 1999): 1709–1718.

NEFDS User's Manual. Version 9.1. Technical report, 1996.

Nicodemus, F. E., J. C. Richmond, J. J. Hsia, I. W. Ginsberg, and T. Limperis.

"Geometrical Considerations and Nomenclature for Reflectance." *Radiometry*. Ed. Lawrence B. Wolff, Steven A. Shafer, and Glenn E. Healey Boston, MA: Jones and Bartlett Publishers, 1992, 94–145.

Parker, Sybil P., editor. *McGraw-Hill Dictionary of Scientific and Technical Terms*. Fourth edition. New York, NY: McGaw-Hill Book Company, 1989.

Priest, Richard G. and Thomas A. Germer. "Polarimetric BRDF in the Microfacet Model: Theory and Measurements." *Proceedings of the 2000 Meeting of the Military Sensing Symposia Specialty Group on Passive Sensors* 1 (2002): 169–181.

Rusinkiewicz, Symon M. "A New Change of Variables for Efficient BRDF Representation." *Proceedings of the Eurographics Workshop on Rendering*. 1998.

Schott, John R. *Remote Sensing: The Image Chain Approach*. New York, NY: Oxford University Press, 1997.

Schott, John R., Scott D. Brown, Rolando Raque no, Harry N. Gross, and Gary Robinson. "Advanced Synthetic Image Generation Models and their Application to Multi/Hyperspectral Algorithm Development." *Canadian Journal of Remote Sensing* 25 (June 1999): 99–111.

Schott, John R., Didi Kuo, Scott Brown, and Rolando Raqueño. "Prediction of observed image spectra using synthetic image generation models." San Diego. *Proceedings of the SPIE* 3118 (July 1997): 81–93.

Straw, David C. "Polarimetry: A New Remote Sensing Tool." *AFRL Technology Horizons* (June 2001): 28–29.

Torrance, Keneth E. and E. M. Sparrow. "Theory for Off-Specular Reflection

From Roughened Surfaces." *Journal of the Optical Society of America* 57 (September 1967): 1105–1114.

Uitenbroek, Han. Polarization of Solar Radiance. December 8, 2000, e-mail conversation.

Weast, Robert C. and David R. Lide, editors. *CRC Handbook of Chemistry and Physics*. 70th edition. Boca Raton, FL: CRC Press, Inc., 1990.

Wellems, D., M. Serna, S. H. Sposato, M. P. Fetrow, S. A. Arko, and T. R. Caudill. Spectral Polarimetric BRDF Model and Comparison to Measurements from Isotropic Roughened Glass. Special Report RD-WS-01-01, U.S. Army Aviation and Missile Command, November 7–9, 2000. Workshop on Multi/Hyperspectral Sensors, Measurements, Modeling and Simulation.

Whitehead, Victor S. "A summary of observations performed and the preliminary findings in the Space Shuttle Polarization Experiment." *SPIE* 1747 (1992): 104–108.

Appendix A

DIRSIG Math Tester

This appendix presents the tests conducted to verify the implementation of the Stokes vector and Mueller matrix classes. The tester is an independent program that can be run to ensure any changes to these base classes do not impact the validity of the mathematical operations. The tests are conducted by hard coding an extensive list of mathematical operations along with the correct answers. The computed results are compared with the preprogrammed answers to ensure accuracy. The tests also check other critical features of the classes to ensure the stability of any programs using these classes.

The CDPolarimetricMath.nw file contains the classes which provide the mechanisms to store Stokes vectors and Mueller matrices and perform all polarimetric computations. These classes also handle performing polarized and unpolarized computations seamlessly on-the-fly.

A.1 Polarimetric Data Sets

Two sets of polarized and unpolarized data sets were used as a basis for all of the tests. Each set had two Stokes vectors, one polarized and one unpolarized, and two Mueller matrices, one polarized and one unpolarized. Care was taken to ensure the data sets produced answers which simplified the detection of errors. For example, the results of test calculations should produce vectors or matrices with all unique elements. This allows for quick identification of transposed answers. Also, answers resulting in zeros were avoided except when specifically testing special cases.

A.1.1 Data Set #1

Unpolarized Stokes Vector $upsv1 = \begin{pmatrix} 5.7 & 0 & 0 & 0 \end{pmatrix}$

Polarized Stokes Vector $psv1 = \begin{pmatrix} 8.7 & 6.5 & 4.3 & 2.1 \end{pmatrix}$

Unpolarized Mueller matrix $upmm1 = \begin{pmatrix} 9.1 & 0 & 0 & 0 \\ 0 & 0 & 0 & 0 \\ 0 & 0 & 0 & 0 \\ 0 & 0 & 0 & 0 \end{pmatrix}$

Polarized Mueller matrix $pmm1 = \begin{pmatrix} 0 & 1 & 2 & 3 \\ 4 & 5 & 6 & 7 \\ 8 & 9 & 10 & 11 \\ 12 & 13 & 14 & 15 \end{pmatrix}$

A.1.2 Data Set #2

Unpolarized Stokes Vector $upsv2 = \begin{pmatrix} 7.2 & 0 & 0 & 0 \end{pmatrix}$

Polarized Stokes Vector $psv2 = \begin{pmatrix} 19.0 & 13.0 & 11.0 & 7.0 \end{pmatrix}$

Unpolarized Mueller matrix $upmm2 = \begin{pmatrix} 8.3 & 0 & 0 & 0 \\ 0 & 0 & 0 & 0 \\ 0 & 0 & 0 & 0 \\ 0 & 0 & 0 & 0 \end{pmatrix}$

Polarized Mueller matrix $pmm2 = \begin{pmatrix} 2 & 3 & 5 & 7 \\ 11 & 13 & 17 & 19 \\ 23 & 29 & 31 & 37 \\ 41 & 43 & 47 & 53 \end{pmatrix}$

In addition to the polarimetric data sets presented above, two scalar variables were also used consistently throughout the testing. These values were stored in floating point variables and used to test the mathematical operations involving the standard C++ floating point numbers. The two variables are

$$f1 = 3.5$$

$$f2 = -4.7$$

A.2 Polarimetric Math Tests

The following sections list the various test performed and their purposes.

A.2.1 Scaling Operations

The following scaling operations were performed using Stokes vectors and Mueller matrices. Both pre and post scaling were tested.

$$upsv1 * f1 \quad f1 * upsv1 \quad psv1 * f1 \quad f1 * psv1$$
$$upmm1 * f1 \quad f1 * upmm1 \quad pmm1 * f1 \quad f1 * pmm1$$

A.2.2 Addition Operations

The following addition tests were performed. The commutative feature was tested by testing both orders of addition for each test.

$$upsv1 + upsv2 \quad upsv2 + upsv1 \quad upmm1 + upmm2 \quad upmm2 + upmm1$$
$$psv1 + upsv2 \quad upsv2 + psv1 \quad pmm1 + upmm2 \quad upmm2 + pmm1$$
$$psv1 + psv2 \quad psv2 + psv1 \quad pmm1 + pmm2 \quad pmm2 + pmm1$$

A.2.3 Subtraction Operations

The following subtraction tests were performed. The order of subtraction was switched to ensure the negative answer was obtained for each case.

$$upsv1 - upsv2 \quad upsv2 - upsv1 \quad upmm1 - upmm2 \quad upmm2 - upmm1$$
$$psv1 - upsv2 \quad upsv2 - psv1 \quad pmm1 - upmm2 \quad upmm2 - pmm1$$
$$psv1 - psv2 \quad psv2 - psv1 \quad pmm1 - pmm2 \quad pmm2 - pmm1$$

A.2.4 Multiplication Operations

The matrix nature of Mueller calculus limits the types of multiplications allowed. The following is an exhaustive list of the allowed multiplication operations.

$$upmm1 * upsv1 \quad upmm1 * upmm2$$
$$upmm1 * psv2 \quad upmm1 * pmm2$$
$$pmm1 * upsv2 \quad pmm1 * upmm2$$
$$pmm1 * psv2 \quad pmm1 * pmm2$$

A.2.5 Division Operations

Division operations are limited to scaling operations between floating point values and a Stokes vector or a Mueller matrix. The following tests were performed.

$$upsv1/f1 \quad psv1/f1$$
$$upmm1/f1 \quad pmm1/f1$$

A.2.6 Functional Tests

The remainder of the tests verify all of the functions built in to the CDStokesVector and CDMuellerMatrix classes. The following is a list of the functions tested:

getDOP	getDOLP	getDOCP
equality (==)	inequality (!=)	
getScalar()	getStokes(i)	getMueller(i, j)
demote()	rotate(theta)	